A New Surface Integral Formulation of EMQS Impedance Extraction for 3-D Structures

by

Junfeng Wang

B.S. Biomedical Engineering, Southeast University, Nanjing (1992)
M.S. Biomedical Engineering, Tsinghua University, Beijing (1995)
M.S. Electrical Engineering, Massachusetts Institute of Technology (1997)

Submitted to the Department of Electrical Engineering and Computer Science
in partial fulfillment of the requirements for the degree of

Doctor of Philosophy

at the

MASSACHUSETTS INSTITUTE OF TECHNOLOGY

September 1999

© 1999 Massachusetts Institute of Technology

All rights reserved.

Signature of Author________________________________
Department of Electrical Engineering and Computer Science
August 15, 1999

Certified by________________________________
Jacob K. White
Professor of Electrical Engineering and Computer Science
Thesis Supervisor

Accepted by________________________________
Arthur C. Smith
Chairman, Departmental Committee on Graduate Students

A New Surface Integral Formulation of EMQS Impedance Extraction for 3-D Structures

by

Junfeng Wang

Submitted to the Department of Electrical Engineering and Computer Science
on August 15, 1999, in partial fulfillment of the
requirements for the degree of
Doctor of Philosophy

Abstract

A new surface integral formulation and discretization approach for computing electromagnetoquasistatic impedance of general 3-D conductors is developed. The key advantages of the formulation is that it avoids volume discretization of the conductors and the substrate, and a single discretization is accurate over the entire frequency range. In addition, the approach does not require a-priori information about proximity effects or the low frequency ditribution of the currents, and the formulation is based on surface integral equations applicable to general 3-D structures.

Computational results from a ring, a wire, an on-chip spiral inductor, a multipin connector and a transmission line examples verify that the formulation is accurate when the predconditioned GMRES iterative method is used to solve the discretized equations for MQS and EMQS analysis. Furthermore, when the $O(N^2)$ part of the matrix-vector multiplication of the iterative solver is accelerated with the Precorrected-FFT algorithm, a fast algorithm with close to $O(N)$ performance in both CPU time and memory is developed.

Thesis Supervisor: Jacob K. White
Title: Professor of Electrical Engineering and Computer Science

Acknowledgments

The research experience toward a Ph.D degree must be one of the most unforgettable parts of one's research life. This is especially true for me because I did the PhD research under the supervision of Prof. Jacob White, to whom I owe the greatest thanks in making the significant progresses in this difficult and challenging research. I was frustrated and depressed so many times by the well-known and new difficulties in the surface formulation for inductance problem, but every time Jacob helped me and encouraged me with his intelligence, optimism and persistent pursuit for the ultimate understanding of the physics truth behind numerics. I could not have gone even half of the way without Jacob.

The research could not have been done without the help from such a group of talented and devoted students and researchers. Dr. Kamon, a former student of Jacob and the author of FastHenry, contributed tremendously to my research. It is through reading his Ph.D thesis and talking with him so many times that the I gained much insights to the problem of inductance extraction and finally figured out the right path of the surface formulation. Dr. Tausch helped me greatly in the previous derivation of the surface formulation. It was through discussion with him that skin effect was found to be captured by the surface formulation. Dr. Phillips helped me in the previous stage of the research even though he is far from MIT. Yehia Massoud helped me to get more intuition of skin effect and the substrate coupling. Dr. Jurgen Singer helped me in various programming problems and math issues. Yong Chen helped me to figure out the 1-D simplification in computing monopole potential for Helmhotz kernel. I also got substantial support from Dr. Tom Korsmeyer and Dr. Wenjing Ye in the complex Precorrected-FFT algorithm.

Outside the group, I got help from Prof. Suiren Wan of Southeast University in the verification of the derivation of surface formulation. Dr. Chi Wang of MIT physics department also helped me when I was puzzled in the low frequency analysis of surface formulation. Meanwhile, the inspiration for research from Mr. Nathaniel Durlach and Prof. Jerry Mendel is also very important.

I can not overemphasize my wife's strong support for my hard work in both time and feeling. In the last two years, she has taken almost all of the load of housework and taken a good care of me. I would not have believed that she could make the dishes so delicious, because all of the skills were learned by herself in the last two years. In addition, my parents always encouraged me to do excellent research at MIT.

In the end, I owe much thanks to the great mathematicians and physicists who describe the world with such a beautiful language of mathematics, and of course, the ultimate thank should go to the one who makes such a beautiful description possible.

To Jianying

Contents

Abstract 3

Acknowledgments 5

List of Figures 14

List of Tables 19

1 Introduction 21

1.1 The need for inductance and capacitance extraction 21

1.1.1 The interconnect problem 21

1.1.2 The packaging problem 22

1.1.3 Useful "parasitics" 23

1.2 Previous work on inductance and capacitance extraction 24

1.2.1 3-D Capacitance extraction methods 24

1.2.2 Inductance extraction methods 25

1.2.2.1 Volume methods 25

1.2.2.2 Advantages of surface methods for inductance extraction 25

1.2.2.3 Existing surface methods of inductance extraction 27

1.2.2.4 The difficulties of inductance extraction using surface methods 28

1.3 The need of coupled inductance and capacitance analysis 29

1.4 The new surface formulation 29

2 **The circuit analogy of impedance extraction** **33**

2.1 The circuit analogy of impedance extraction 33

2.2 The difficulties of a surface formulation 34

2.3 The impedance extraction for multiple conductor cases 35

3 **The new surface formulation for EMQS impedance extraction** **37**

3.1 EMQS analysis for the time harmonic electromagnetic field 37

3.1.1 The time harmonic Maxwell's equations 37

3.1.2 EMQS analysis for time harmonic electromagnetics 39

3.2 Two dyadic surface integral equations 40

3.2.1 The first dyadic surface integral equation 40

3.2.2 The second dyadic surface integral equation 41

3.3 The surface integral form for current conservation 43

3.4 The capacitive surface integral equation and boundary conditions 44

3.4.1 Capacitive surface integral equation 44

3.4.2 Boundary conditions 45

4 **Discretization** **47**

4.1 Discretization of the first dyadic surface integral equation 48

4.1.1 Discretization of the second dyadic surface integral equation . . . 50

4.2 Discretization of the integral form of current conservation 53

4.3 Discretization of the capacitive integral equation 55

4.4 Applying the boundary condition in the discretization 56

4.5 The linear system and the computation of the input current 57

4.5.1 The linear systems for EMQS and MQS impedance extraction . . 57

4.5.2 Current computation, impedance extraction and circuit parameter extraction 59

5 **Low frequency and high frequency problems** **63**

5.1 The low frequency problem 63

5.1.1 $\sqrt{\omega}$ term at low frequency 64
5.1.2 The elimination of the $\sqrt{\omega}$ term and the justification 66
5.2 The high frequency problem 72

6 The panel integration of the Green's function 79
6.1 Helmhotz kernel 79
6.2 The integration by side 81
6.3 The desingularization transform 83
6.4 The inner integration 85
6.4.1 The inner integration of ψ 85
6.4.2 The inner integration of computing $\frac{\partial\psi}{\partial D}$ 86
6.4.2.1 Normal derivative 87
6.4.2.2 The derivative at tangential direction of t_1 88
6.4.2.3 The derivative at tangential direction of t_2 89
6.5 The outer integration about θ and an improvement 90
6.5.1 A plain outer integration scheme 90
6.5.2 A flaw in the plain outer integration and the solution 91
6.6 Linearized kernel 93
6.6.1 Computing $\int_S Rds$ 94
6.6.2 Computing $\int_S \frac{\partial R}{\partial n}ds$ 94

7 Preconditioned iterative solver 97
7.1 GMRES, an iterative solution method 97
7.2 Iteration number and preconditioning 98
7.2.1 GMRES iteration number of the surface formulation 98
7.2.2 The condition number and the scaling problem 99
7.2.3 The eigen value distribution and the structure problem 101
7.2.4 An effective and efficient preconditioner 102
7.3 Numerical accuracy test of the preconditioned iterative solver 105
7.3.1 A ring example 105

7.3.2 A wire example 106
7.3.3 Multipin Connector 109
7.3.4 Spiral Inductor over a substrate ground plane 109
7.3.5 Transmission Line 112
7.3.6 The iteration number of the large examples 114

8 The Precorrected-FFT acceleration **115**
8.1 the Precorrected-FFT method 116
8.2 Polynomial projection scheme 117
8.3 Numerical result of the accelerated formulation 119
8.3.1 Comparison with FastHenry 119
8.3.2 Three typical examples 120
8.3.2.1 A 4 by 4 multipin connector 120
8.3.2.2 An 8 turn spiral over a ground plane 121
8.3.2.3 The shorted transimission line 121
8.3.2.4 The memory and CPU time performance 122
8.3.3 Asymptotic performance of the accelerated formulation 123
8.3.4 Comparison of different solution methods 125
8.3.5 The EMQS analysis of the spiral inductor problem 125
8.3.6 The convergence rate of EMQS analysis 127

9 Extension to fullwave impedance extraction **131**
9.1 Fullwave analysis of time harmonic electromagnetics 131
9.1.1 Time harmonic Maxwell's equations 131
9.1.2 Fullwave analysis for time harmonic electromagnetic field 132
9.2 Two dyadic surface integral equations 133
9.2.1 The first dyadic surface integral equation 133
9.2.2 The second dyadic surface integral equation 134
9.3 The current conservation, the capacitive integral equation and boundary conditions 135

9.4 Numerical simulations 136
    9.4.1 Fullwave analysis of the long shorted transmission line 136
    9.4.2 Limit of EMQS analysis 137

10 Conclusions and future work **141**

10.1 Conclusions 141
10.2 Future work 142

List of Figures

1-1 The packaging example of Harris Semiconductor 22
1-2 A proximity sensor 23
1-3 A coarse 3-D discretization of the ground 26

2-1 A simple example of impedance extraction 33
2-2 The conversion of impedance extraction to circuit analysis 34
2-3 Multiple conductor impedance extraction 35

3-1 Multiple conductors in time harmonic EM field 38
3-2 Illustration of the first dyadic surface integral equation 40
3-3 Illustration of the second dyadic surface integral equation 42
3-4 A thin box for surface current conservation 44

4-1 The discretization of the surface 47
4-2 The centroid collocation scheme 48
4-3 A four conductor problem 49
4-4 P_1 matrix of a four conductor problem 49
4-5 Computation of the gradient of potential 52
4-6 Dual panel for current conservation 53
4-7 The decomposition of the dual panel 54
4-8 The computation of the centroid potential 55
4-9 The summation of the current 60

5-1 The discretized ring 64

5-2 The abnormal behavior at low frequency 65
5-3 A conductor under electrostatics 69
5-4 A discretized wire 72
5-5 The skin effect at two frequencies 73
5-6 The skin effect for a conductor of general geometry 73
5-7 The discretization of the cross section to capture skin effect 74
5-8 An equivalent way of high frequency current computation 75
5-9 The local coordinate on the peripheral of the cross section 76
5-10 The finite difference scheme for E_n term 77

6-1 The potential due to the source over a panel 79
6-2 The conversion from dipole potential to the derivative of monopole potential 80
6-3 The integration over a polygon 81
6-4 The decomposed integration over a polygon 82
6-5 The decomposed integration over a triangle 82
6-6 The one-side integration of a panel 83
6-7 The one side integration in polar coordinates 84
6-8 The inner integration bounds of one side polar integration 84
6-9 Three directions of the derivative computation 87
6-10 The perturbation of side AB along t_1 88
6-11 The perturbation of side AB along t_2 90
6-12 The flaw in the outer integration 91
6-13 The basic integration of the linearized kernel 94

7-1 A wire of 216 panels 99
7-2 The eigen values at 1000 Hz 101
7-3 The eigen values at 10^{17} Hz 101
7-4 The eigen values of the preconditioned system at 1000 Hz 104
7-5 The eigen values of the preconditioned system at 10^{17} Hz 104

7-6 A discretized ring 105
7-7 Inductance for the ring example 106
7-8 Resistance for the ring example 107
7-9 A wire example 107
7-10 Inductance for the wire example 108
7-11 Resistance for the wire example 108
7-12 A 3 by 3 curved connector example 109
7-13 Inductance for a 3 by 3 curved connector 110
7-14 Resistance for a 3 by 3 curved connector 110
7-15 A spiral inductor over a substrate ground plane 111
7-16 Inductance for the spiral inductor with and without a substrate ground plane 111
7-17 Resistance for the spiral inductor with and without a substrate ground plane 112
7-18 A long shorted transmission line 113
7-19 Admittance of the long transmission line 114

8-1 The potential evaluation problem 115
8-2 Precorrected-FFT method 117
8-3 Worst case projection error for a typical example 118
8-4 A 4 by 4 connector 120
8-5 The inductance of the 4 by 4 connector 120
8-6 The resistance of the 4 by 4 connector 121
8-7 An 8 turn spiral over a ground plane 122
8-8 The inductance of the 8 turn spiral over a ground plane 122
8-9 The resistance of the 8 turn spiral over a ground plane 123
8-10 The admittance of the shorted transmission line 123
8-11 The memory usage versus the number of panels 124
8-12 The cputime versus the number of panels 124
8-13 The admittance resonance peak of the two turn spiral 126

8-14 The effective inductance of the two turn spiral 127

8-15 The effective inductance of the eight turn spiral 128

8-16 A wire example 128

8-17 A wire discretized into 24 panels 128

9-1 The illustration of the first dyadic surface integral equation 133

9-2 The illustration of the second dyadic surface integral equation 135

9-3 The fullwave admittance of the shorted transmission line 137

9-4 EMQS and fullwave results for $d = 500$ 138

9-5 EMQS and fullwave results for $d = 5000$ 138

List of Tables

5-1 Imaginary part of the impedance under different F_L's 72
5-2 Imaginary part of the impedance from two different methods 78
5-3 Three modes of computation 78

7-1 Iteration number of the wire 98
7-2 Condition number and iteration number of the wire 99
7-3 The improvement by the preconditioner 104
7-4 Size of the problem and GMRES iteration number 114

8-1 Comparison with FastHenry 119
8-2 Performance of the accelerated formulation 123
8-3 CPU time of different methods 126
8-4 Memory usage of different methods 126
8-5 The average amplitude of admittance 129

1

Introduction

1.1 The need for inductance and capacitance extraction

The inductance and capacitance can be important parameters of a system, wanted or unwanted. In the interconnect and packaging problems, the existence of the parasitic inductance and capacitance can change the performance of the system greatly, so that it is very important to extract these parasitics. It is even more important to extract the inductance and capacitance accurately where the system is based solely on the inductors and capacitors, as in some MEMS devices and in the use of spiral inductors in RF circuits.

1.1.1 The interconnect problem

In the early days of the semiconductor circuits, the speed bottleneck was at the devices, while the interconnect connecting the devices could be taken as ideal connection with no parasitic effects. When the devices are running at low frequencies, the propagation delay and the waveform deformation caused by the interconnect are negligible so that the parasitic inductance and capacitance can be ignored. However, the interconnect problem is getting more and more serious as the semiconductor devices are running at higher and higher frequencies. Recently the operation frequency of the semiconductor circuits can be close to one gigahertz, and the parasitic resistance, inductance and capacitance effects of the interconnect can change the performance of a circuit significantly.

It is well known that the parasitic capacitance and resistance effects of the interconnect can cause propagation delay [24], while the coupled inductance and capacitance effects of the interconnect can not only change the propagation delay but also introduce ringing behavior [24], and this influences signal integrity. In addition, the coupling between the interconnect and the substrate introduces noise in the signal [27] and so does the coupling between the nearby interconnect wires. In the frequency domain, the coupled inductance and capacitance effects can create resonance peaks in the interconnect frequency response [37], and the substrate coupling tends to reduce the inductance significantly at high frequencies. To account for these parasitic effects, extraction tools are necessary.

1.1.2 The packaging problem

In the packaging problem, inductance and capacitance effects are also very important to the performance of the system. Figure 1-1 shows an RF packaging system. Accurate resistance, inductance and capacitance extraction is essential for reliable circuit simulation [37]. Figure 1-1 also comes from [37].

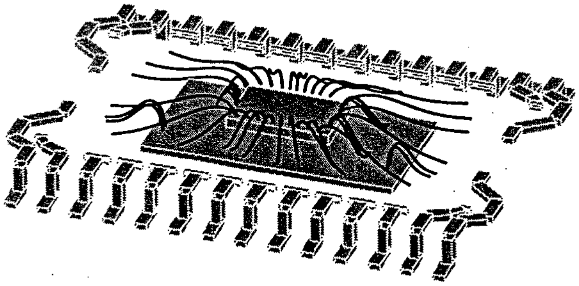

FIGURE 1-1: The packaging example of Harris Semiconductor

1.1.3 Useful "parasitics"

Although inductance and capacitance effects are taken as unwanted parasitic effects in the interconnect and packaging cases, MEMS devices sometimes rely on the inductance and capacitance of the conductors.

In Figure 1-2 the spiral inductor can be used as a proximity sensor to measure the distance from a ground plane. The underlying mechanism is that the inductance of the spiral inductor changes sharply with the distance from the ground plane.

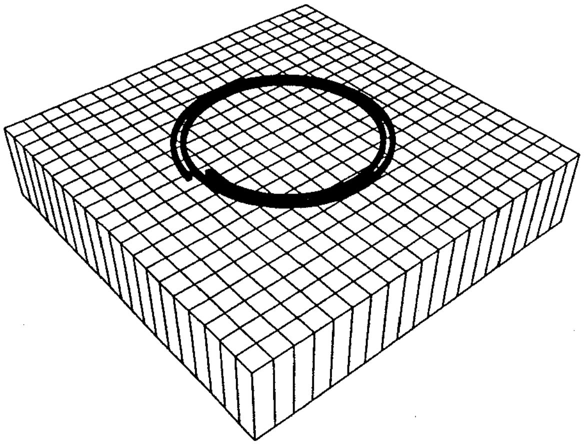

FIGURE 1-2: A proximity sensor

Surprisingly, the problem is very similar to the substrate coupling noise problem in the case of on-chip interconnect analysis. The only difference is that the substrate coupling is unwanted in the on-chip interconnect cases while it is used in the MEMS device.

Inductance and capacitance extraction is also very important to the modeling of spiral inductors in RF circuits [34]. The increase of effective inductance due to the inductance-capacitance coupling plays an important role in the performance of RF circuits.

1.2 Previous work on inductance and capacitance extraction

1.2.1 3-D Capacitance extraction methods

Since the structures for capacitance extraction are mostly complicated 3-D geometries, 3-D capacitance extraction methods have been developed that are based on the surface integral equation that relates the scalar potential to the charge on the surface

$$\int_S G(x,y)\frac{\rho}{\epsilon}dy = \psi(x)$$

where S is the surface of the conductor, ρ is the charge density, ψ is the potential on the surface, ϵ is the permittivity, and $G(x,y)$ is the Green's function. This integral equation follows from the Laplace equation for the scalar potential inside and outside the conductors and the fact that the charge is just on the surface. Starting from the surface integral equation, the boundary element method is used to solve for the capacitance [20, 21].

In typical applications, large number of unknowns are encountered, and this makes the direct solution of the linear system very costly. The direct solution of the linear system requires $O(N^3)$ CPU time and $O(N^2)$ memory.

Fortunately, fast methods have been developed for capacitance extraction [16, 17, 11] in the last decades that get close to $O(N)$ performance both in CPU time and memory, by using iterative solving methods such as GMRES [13] and matrix sparsification techniques such as the fast multipole algorithm [7], the Precorrected-FFT algorithm [8], SVD algorithm [10] and wavelet based methods [11].

The GMRES iterative method reduces the $O(N^3)$ operations of Gaussian Elimination to a small number of matrix vector multiplications, and each matrix vector multiplication requires $O(N^2)$ operations. Matrix sparsification methods accelerate the matrix vector multiplication reducing the number of operations from $O(N^2)$ to near $O(N)$. Although the fast multipole algorithm is utilizing the Green's function kernel of the Laplace equation so that the method is not applicable to general kernels, the Precorrected-FFT algorithm, SVD algorithm, and wavelet based methods can be used as general matrix sparsification schemes.

The number of GMRES iterations is another factor that can affect the performance of the fast methods. The second kind integral formulation [15] of the Laplace equation improves the conditioning of the linear system and reduces the number of iterations.

1.2.2 Inductance extraction methods

1.2.2.1 Volume methods

Inductance extraction is much more complicated than the capacitance extraction. In capacitance extraction, a very special case of the electrostatistics field is analyzed in which there is neither current nor magnetic field, so that the potential can be specified on the surface to solve for the charge distribution. In inductance extraction, however, the coupled electrical and magnetic field have to be analyzed at the same time, which requires the solution of Maxwell's equation.

Since the current is nonzero everywhere in the volume in the inductance problem, volume based methods have been developed [22, 23, 25, 26]. The PEEC method introduced in [23] has gained the most popularity, probably because it is applicable to a wide range of problems.

These volume based methods still have the disadvantage of using direct solution of the linear systems, which is costly both in CPU time and memory. FastHenry, a fast version of PEEC, is developed in [18]. Similar to FastCap, FastHenry combines GMRES iterative solver and fast multipole matrix sparsification technique. FastHenry has the performance of close to $O(N)$ in both CPU time and memory.

1.2.2.2 Advantages of surface methods for inductance extraction

The advantages of surface methods for inductance extraction can be shown in considering the following problems:

1. The high frequency problem:

   The volume based methods have to use very fine discretizations to handle high frequency problems because skin effect drives the current to the surface of the conductor. This makes the volume method very costly at high frequency [18], and causes anomalies in some cases [19].

2. Model order reduction(MOR):

   Model order reduction [35, 36] generates a much smaller compact model of the original system. The different requirements of discretization for volume methods at low frequency and high frequency leads to one dense discretization for the whole frequency range being used for model order reduction [37]. Hence for model order reduction, surface methods seem to be appropriate.

3. The ground plane problem:

   In cases when a non-ideal ground plane is present, the proximity effect can change the inductance of the structure above the ground plane to a great extent. To simulate the proximity effect of the ground plane, a dense 3-D mesh needs to be used [27]. Figure 1-3 is just a coarser version of the actual mesh of the ground plane. If a surface method is used, only the surface of the ground plane must be meshed, reducing the number of unknowns.

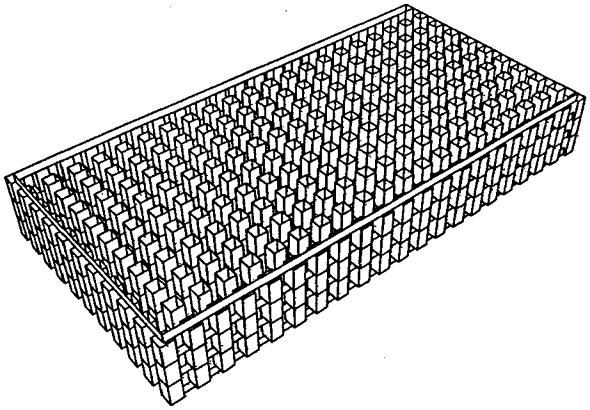

FIGURE 1-3: A coarse 3-D discretization of the ground

4. Curved structures:

   Even though PEEC and FastHenry are applicable to 3-D problems, the discretization of the volume of a curved structure can be very difficult. If a surface method is developed for general 3-D structures, the discretization would be much easier.

1.2.2.3 Existing surface methods of inductance extraction

Although various surface methods have been proposed, most of them are limited to the high frequency inductance extraction of 2-D transmission line problems.

Djordjevic and Sarkar [28] analyzed a cylindrical conductor excited by an axially independent TM electromagnetic field. A nonphysical distribution of current was assumed along the propagation direction, causing an excess resistance at high frequencies. Wu and Yang [30] modified this method to allow quasi-TEM propagation. Tusk and Kong [31] developed a surface method for inductance and resistance extraction of transmission lines at high frequency under the MQS assumption. Neikirk *et al* [29] developed a surface ribbon method for inductance extraction of interconnect using surface impedance.

All of these surface methods have difficulties at low frequency. Surface methods in [28], [30] and [31] are based on the normal derivative of the electrical field, and this creates numerical difficulty because the normal derivative of the electrical field is close to zero at low frequency. Take [31] for example, the basic relation to compute the current is:

$$I = \frac{i}{\omega\mu\sigma}\int_L \frac{\partial J_z}{\partial n} dl$$

At very low frequency, $\frac{\partial J_z}{\partial n}$ should be $O(\omega)$ because the denominator is $O(\omega)$. This means the numerical error in computation of $\frac{\partial J_z}{\partial n}$ can easily corrupt the accuracy of I.

The method in [29] based on surface impedance assumes that the electrical field takes exponential form in respect to the distance from the surface. This assumption is based on 1-D high frequency analysis and is not accurate at low frequencies. In addition, the surface impedance is defined as the ratio of the total electrical field to the total magnetic field, so that numerically the ratio could blow up at low frequency because the magnetic field could be vanishingly small while the electrical field remains substantial at very low frequency.

In addition to the low frequency problem, these surface methods have other restrictions. Methods in [28] and [30] are using TM and quasi-TEM assumptions, which are not necessarily true for general 3-D fields. The method in [31] only has MQS assumption, but it is limited to 2-D transmission line problems. The method in [29] is also limited to 2-D interconnect problems.

1.2.2.4 The difficulties of inductance extraction using surface methods

From the review in the preceding paragraphs, it is clear that none of the existing surface methods of inductance extraction can be applied to general 3-D structures at both low and high frequencies.

The biggest challenge of a general surface method comes from the low frequency problem. With the current spread over all the volume at the low frequencies, a surface method has to account for the contribution from the volume current by the surface quantities. The surface representation of the volume field needs to be achieved without assumption of the field distribution so that the surface method can be used for the inductance extraction at any frequency. This is also necessary for the proximity effect to be captured with the surface formulation, because the proximity effect changes the field distribution.

Another challenge of a general surface method is that the assumption related to the geometry should be abandoned. For example, the assumption that the vector potential satisfies Laplace equation [31] is only valid for 2-D transmission line and it should not be used for general 3-D geometries. The assumption that the electrical field takes the exponential form in respect to the distance from the surface [29] should not be used for general 3-D geometries either, because the assumption is based on 1-D high frequency analysis. The surface representation of the volume field should be achieved without any assumption of the geometry so that the surface method could be used for general 3-D structures.

1.3 The need of coupled inductance and capacitance analysis

To get the frequency response of a structure, the lumped inductance and lumped capacitance are usually extracted separately, and then combined in a circuit model. This approach is based on the assumption that the inductance and capacitance can be decoupled in the solution of Maxwell's equation. However, it is unclear if this assumption is always correct.

A safe way to get the frequency response of a structure is to solve Maxwell's equation making as little assumption as possible so that the inductance, the capacitance and the resistance are considered at the same time. Since the dimension of the sturctures is normally smaller than the wavelength, the electromagnetoquasistatic(EMQS) assumption can be made to simplify Maxwell's equations. The impedance extracted under the EMQS assumption is the distributed RLC impedance.

1.4 The new surface formulation

A volume method of EMQS impedance extraction is developed in [32]. As a surface method can have many advantages over volume methods in inductance extraction, a general surface formulation for EMQS impedance extraction can also have advantages in handling the high frequency problem, modeling of the proximity effect of a ground plane, generating inexpensive frequency independent discretization for MOR and requiring little effort in the discretization of a curved structure.

At the same time, the difficulties of surface methods for inductance extraction are also inherited by the surface methods for EMQS impedance extraction. The key difficulty is to find a general surface representation of the volume current without an assumption of current distribution or the geometry of the structures.

In this thesis, a new surface formulation of distributed RLC(EMQS) impedance extraction for 3-D structures is developed which overcomes the difficulties of the surface methods mentioned above. The new surface formulation can perform EMQS impedance extraction for general 3-D structures at both low frequencies and high frequencies.

The new surface formulation overcomes these difficulties with two dyadic surface integral equations that relate the electrical field to the scalar potential, and a surface integral form of $\nabla \cdot \bar{E} = 0$.

These two dyadic surface integral equations are directly derived from Maxwell's equations so that they are applicable to general 3-D structures and arbitrary frequencies. The surface integral form of $\nabla \cdot \bar{E} = 0$ is also applicable to general structures.

When the charge density is set to zero, the surface formulation can be used to perform MQS impedance extraction so that the inductance and resistance of the structure can be computed.

In Chapter 2, a circuit analogy is made for the impedance extraction, so that the necessary steps toward a surface formulation for impedance extraction can be clearly identified. It is shown that two basic volume-based relations need to be transformed into surface forms, one is $-\nabla\psi = \bar{E} + i\omega\bar{A}$, another is $\nabla \cdot \bar{E} = 0$.

In Chapter 3, two daydic surface integral equations are derived directly from Maxwell's equations that relate the electrical field and its normal derivative to the gradient of the scalar potential. The first surface integral equation captures the skin effect for general 3-D structures. Actually, the first surface integral equation is a special case of a surface integral equation that relates the electrical field of any point inside a conductor to the electrical field and its normal derivative on the surface. The second dyadic surface integral equation is a direct transform of $-\nabla\psi = \bar{E} + i\omega\bar{A}$ to the surface form, with the normal derivative of electrical field introduced which can be eliminated along with the first dyadic surface integral equation. The surface integral form of $\nabla \cdot \bar{E} = 0$ is derived by taking the limit of a thin box right underneath the surface.

In chapter 4, the discretization of all of the equations are discussed, along with the correct boundary conditions to be applied at the contact and non-contact panels.

In chapter 5, the low frequency numerical problem is explained and eliminated by linearization. The high frequency problem due to the skin effect is solved by computing the input current with the magnetic field nearby, which can be translated into the derivative of the electrical field.

Chapter 6 shows an efficient numerical scheme to compute the panel integration of the Helmhotz kernel and its derivative. The integration of the linearized kernel is also covered. A numerical scheme is described which eliminates the singularity with a transformation, and reduces the 2-D integration into 1-D integration for efficient computation with a Gauss quadrature scheme.

In chapter 7, validation of the preconditioned GMRES iterative solver is presented using various examples. Both MQS and EMQS impedance extraction is performed, and the results are compared with analytic results and the results from FastHenry. The comparison shows that the formulation gives satisfactory results. It is also shown that a cheap preconditioner reduces the iteration number greatly.

In chapter 8 the surface formulation is accelerated further by computing the potential evaluation part of matrix vector multiplication with the Precorrected-FFT algorithm. After the acceleration, the surface formulation has the performance of close to $O(N)$ in both CPU time and memory.

In chapter 9, an extension to fullwave impedance extraction is described. With the example of a shorted transmission line, it is shown that the fullwave impedance extraction of the surface formulation yields accurate results compared with those from analytic formula.

Conclusions and suggestions for future work are included in chapter 10.

2

The circuit analogy of impedance extraction

2.1 The circuit analogy of impedance extraction

Impedance extraction for a certain structure (Figure 2-1) consists of determining the voltage and current relation at the two terminals (ports, or contacts) at a certain frequency. Typically, the voltage drop V (or potential difference $\psi_+ - \psi_-$) is specified between the two contacts (C_+ and C_-), so that the current I(or electrical field $\bar{E}$) can be computed by solving Maxwell's equations.

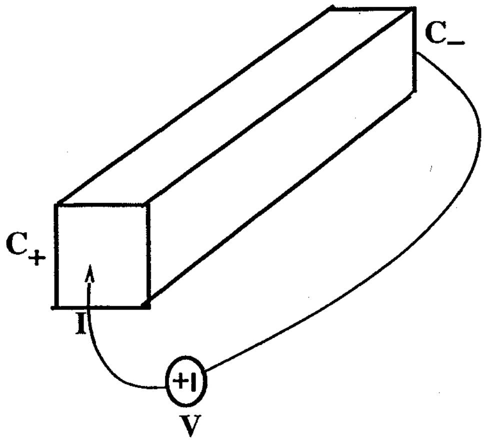

FIGURE 2-1: A simple example of impedance extraction

The problem resembles the nodal analysis of a circuit when a voltage source is applied between two terminals and the input current is to be solved.

The volume based MQS impedance extraction program FastHenry [18] exploits the similarity to a further extent. There are two basic equations used in FastHenry, one is $-\nabla\psi = \bar{E} + i\omega\bar{A}$, the other is $\nabla\cdot\bar{E} = 0$. The first equation can be taken as the equivalent to the constitutive relationship in nodal analysis, while the second equation is equivalent to the current conservation law in circuit theory.

Due to the similarity between the equations used in FastHenry and the circuit analysis equations, the impedance extraction problem of the wire in (a) of Figure 2-2 is converted to the circuit analysis problem in (c) of Figure 2-2 through the discretization shown in (b) of that figure. The figure comes from [37].

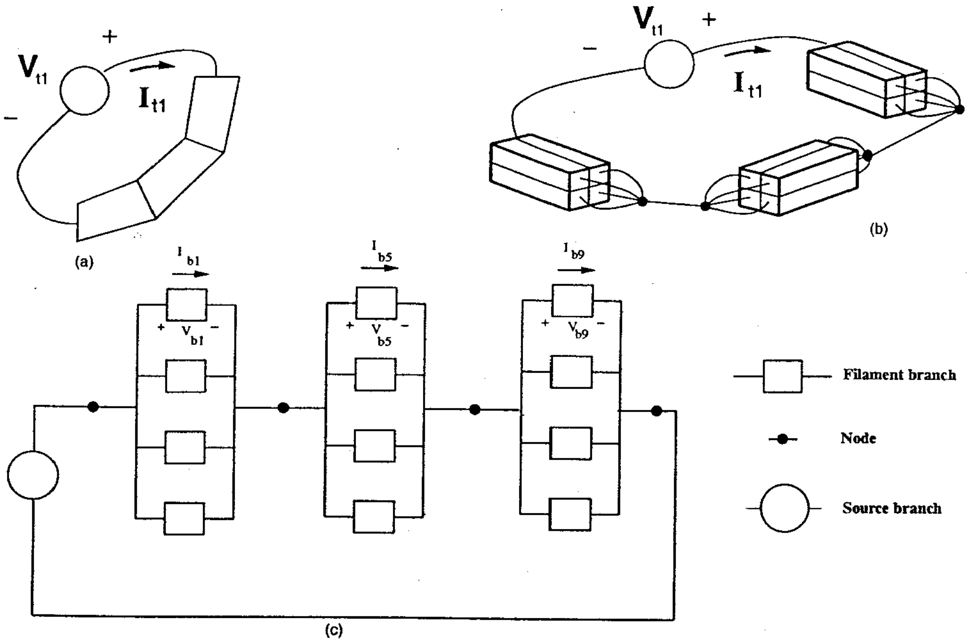

FIGURE 2-2: The conversion of impedance extraction to circuit analysis

2.2 The difficulties of a surface formulation

Any surface formulation faces two major difficulties if the circuit analysis analogy is to be exploited.

1. It is difficult to transform the constitutive relationship of $-\nabla\psi = \bar{E} + i\omega\bar{A}$ to a

surface form.

The difficulty comes from the fact that $\bar{A}$ is has a contribution from the currents over all the volume of the conductor. A general transformation needs to be found that can change the volume equation to a surface equation that is valid for any frequency and general 3-D structures.

2. It is also difficult to change the volume equation $\nabla \cdot \bar{E} = 0$ to a surface equation.

In the next chapter, two dyadic surface integral equations are derived that can play the role of the constitutive relationship, while the current conservation equation is also changed to a surface integral form.

Unlike the constitutive equation or current conservation equation, the equation relating the scalar potential to the charge is naturally a surface equation because the charge is only on the surface at time harmonics, as will be shown in the next chapter.

2.3 The impedance extraction for multiple conductor cases

For M conductor cases (Figure 2-3), the mutual impedance should also be extracted. The extraction is the determination of the impedance matrix Z, which relates the voltage vector $\bar{V}$ to the current vector $\bar{I}$ by:

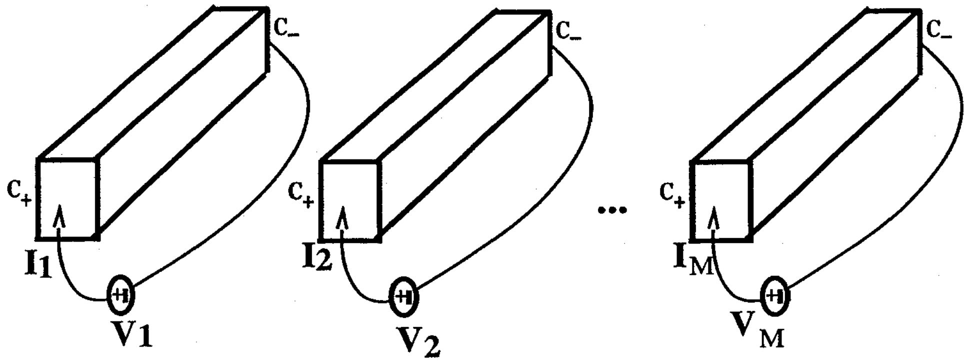

FIGURE 2-3: Multiple conductor impedance extraction

$$Z\bar{I} = \bar{V}$$

By applying M linearly independent voltage vectors, M current vectors can be computed. If these voltage vectors are written as matrix M_V with every column a voltage vector, and the current vectors are written as matrix M_I in the same way, the equation about Z can be written as:

$$ZM_I = M_V$$

Then the impedance matrix can be solved as:

$$Z = M_V {M_I}^{-1}\,.$$

3

The new surface formulation for EMQS impedance extraction

In impedance extraction, the electrical field around the contact where the potential is applied must be solved. The constitutive relation $-\nabla\psi = \bar{E} + i\omega\bar{A}$ and current conservation are essential in the solution. This chapter gives the surface version of these basic equations, and describes the appropriate boundary conditions.

3.1 EMQS analysis for the time harmonic electromagnetic field

3.1.1 The time harmonic Maxwell's equations

Consider the electromagnetic field for the multiple conductor example in Figure 3-1. It is assumed that the permeability μ and the permittivity ϵ are constant over all the space, and the conductivity σ is constant for each conductor.

Maxwell's equations at time harmonics are [1, 2]:

$$\nabla \times \bar{E} = -i\omega\mu\bar{H} \tag{3.1}$$

$$\nabla \times \bar{H} = i\omega\epsilon\bar{E} + \bar{J} \tag{3.2}$$

$$\nabla \cdot (\epsilon\bar{E}) = \rho \tag{3.3}$$

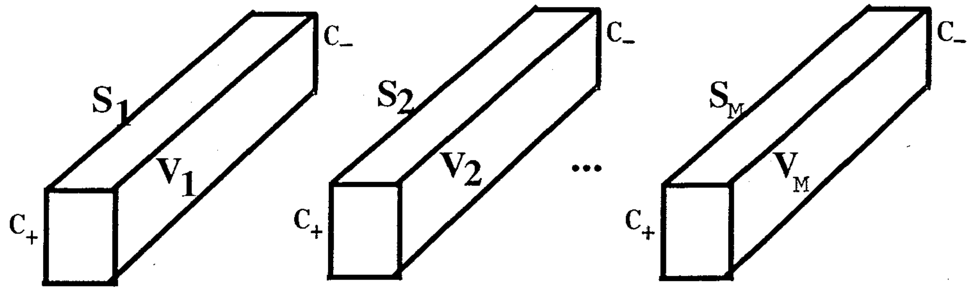

FIGURE 3-1: Multiple conductors in time harmonic EM field

$$\nabla \cdot (\mu \bar{H}) \;=\; 0 \tag{3.4}$$

where ω is the angular frequency.

In addition, within the conductors, by Ohm's law,

$$\bar{J} = \sigma \bar{E} \tag{3.5}$$

where σ is the conductivity.

Taking the divergence on both sides of equation (3.2) and using the uniform ϵ and the conductor-wise-uniform σ, then we have:

$$0 = (\sigma + i\omega\epsilon)\nabla \cdot \bar{E}$$

Therefore, $\nabla \cdot \bar{E} = 0$ is true inside the conductors. For the space outside the conductors where σ is 0, $\nabla \cdot \bar{E} = 0$ can be proved for nonzero frequency with the same approach. For zero frequency, or electrostatics, $\nabla \cdot \bar{E} = 0$ is obviously correct for both inside and outside of conductors. So, the electrical field is divergence free for both inside and outside of the conductors for time harmonic electromagnetics with uniform μ, ϵ and conductor-wise-uniform σ:

$$\nabla \cdot \bar{E} = 0 \tag{3.6}$$

With Gauss's Law (3.3) and uniform ϵ, the charge density ρ must be zero both inside and outside the conductors. This means the charge is only on S, the union of all conductor surfaces.

3.1.2 EMQS analysis for time harmonic electromagnetics

Because the displacement current is neglected under the EMQS assumption, Ampere's Law is changed to its EMQS form

$$\nabla \times \bar{H} = \bar{J} \tag{3.7}$$

The equivalent representation of Maxwell's equation with vector potential and scalar potential for EMQS analysis is well known [1, 2, 37]. With $\nabla \cdot \bar{A} = 0$ (Coulomb gauge) , $\mu\bar{H} = \nabla \times \bar{A}$ and $-\nabla\psi = \bar{E} + i\omega\bar{A}$, the differential equations for $\bar{A}$ and ψ turn out to be:

$$\nabla^2 \bar{A} = -\mu\bar{J} \tag{3.8}$$

and

$$\nabla^2 \psi = -\rho/\epsilon \tag{3.9}$$

where ρ is nonzero only on S.

Therefore, the integral equations for $\bar{A}$ and ψ are:

$$\bar{A}(x) = \int_V G_0(x,y)\mu\bar{J}(y)dy \tag{3.10}$$

and

$$\psi(x) = \int_S G_0(x,y)\frac{\rho(y)}{\epsilon}dy \tag{3.11}$$

where $G_0(x,y) = \frac{1}{4\pi|x-y|}$, V is the union of all conductor volumes and S is the union of all conductor surfaces.

3.2 Two dyadic surface integral equations

In this section, two dyadic surface integral equations are presented that are equivalent to $-\nabla\psi = \bar{E} + i\omega\bar{A}$. These dyadic surface integral equations are applicable to general 3-D structures and arbitrary frequencies.

3.2.1 The first dyadic surface integral equation

The first dyadic surface integral equation is derived for every conductor separately(Figure 3-2).

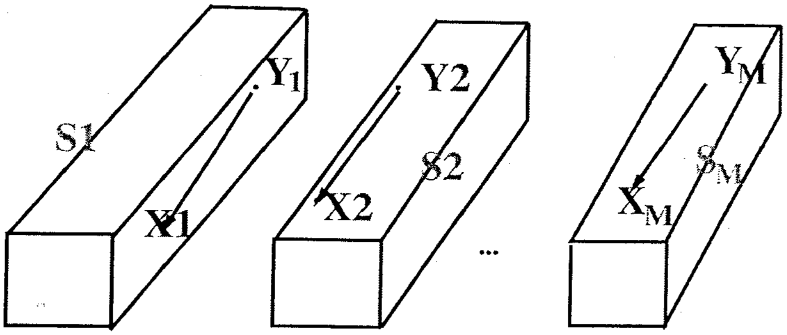

FIGURE 3-2: Illustration of the first dyadic surface integral equation

For the inside of the k-th conductor, the electromagnetic field satisfies Faraday's Law (3.1) and Ampere's Law under the EMQS assumption (3.7), which can be written as

$$\nabla \times \bar{E} = -i\omega\mu\bar{H} \tag{3.12}$$

$$\nabla \times \bar{H} = \sigma_k\bar{E} \tag{3.13}$$

with $\bar{J} = \sigma_k\bar{E}$ applied.

Taking the curl on both sides of Farady's Law (3.12), using the vector identity $\nabla \times (\nabla \times \bar{E}) = \nabla(\nabla \cdot \bar{E}) - \nabla^2\bar{E}$ with $\nabla \cdot \bar{E} = 0$, and also applying (3.13), we have a vector Helmhotz equation for $\bar{E}$ inside the k-th conductor

$$\nabla^2\bar{E} - i\omega\mu\sigma_k\bar{E} = 0 \tag{3.14}$$

which is homogeneous for every conductor.

Applying Green's Second Identity [4] to (3.14) with $x \in V_k$ as the evaluation point of the Green's function yields a dyadic surface integral equation

$$\int_{S_k} G_1(x,y)\frac{\partial \bar{E}(y)}{\partial n_y}dy - \int_{S_k} \frac{\partial G_1(x,y)}{\partial n_y}\bar{E}(y)dy = \bar{E}(x) \tag{3.15}$$

where S_k and V_k are the surface and the volume of the k-th conductor,

$$G_1(x,y) = \frac{e^{iK_1|x-y|}}{4\pi|x-y|}, \; K_1 = \sqrt{-i\omega\mu\sigma_k}. \tag{3.16}$$

The surface integral equation relates the electrical field at any point inside the volume V_k to the electrical field and the normal derivative of the electrical field on the surface S_k.

With x moved to the interior of S_k in the equation above, a dyadic surface integral equation is derived which is based on the electrical field and its normal derivative:

$$\int_{S_k} G_1(x,y)\frac{\partial \bar{E}(y)}{\partial n_y}dy - \int_{S_k} \frac{\partial G_1(x,y)}{\partial n_y}\bar{E}(y)dy = \bar{E}(x) \tag{3.17}$$

where $x, y \in S_k$.

Note that a simpler notation is used in which $\int_{S_k} \frac{\partial G_1(x,y)}{\partial n_y}\bar{E}(y)dy$ is the entire integral rather than a principle-value integral plus an extra term.

3.2.2 The second dyadic surface integral equation

The second dyadic surface integral equation is derived by considering all conductors at the same time, so that the coupling between the electromagnetic field can be accounted for(Figure 3-3).

Equation (3.14) can be rewritten as another vector Helmhotz equation:

$$\nabla^2 \bar{E} = i\omega\mu\bar{J} \tag{3.18}$$

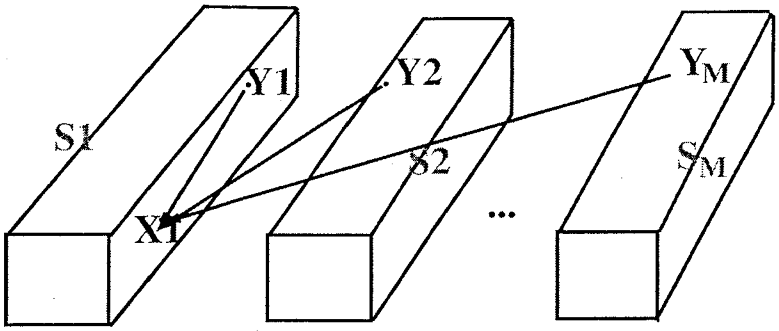

FIGURE 3-3: Illustration of the second dyadic surface integral equation

which is homogeneous throughout the space.

Applying Green's Second Identity to (3.18) with $x \in V$ as the evaluation point of the Green's function yields the following integral equation

$$\int_S G_0(x,y)\frac{\partial \bar{E}(y)}{\partial n_y}dy - \int_S \frac{\partial G_0(x,y)}{\partial n_y}\bar{E}(y)dy = \bar{E}(x) + i\omega \int_V \mu G_0(x,y)\bar{J}(y)dy$$

where V is the union of all conductor volumes, S is the union of all conductor surfaces, and

$$G_0(x,y) = \frac{1}{4\pi|x-y|}$$

Note that the Green's function is the same as that used in the integral form of $\bar{A}$ and ψ. G_0 can be taken as a Helmhotz kernel of $G_0(x,y) = \frac{e^{iK_0|x-y|}}{4\pi|x-y|}$ where K_0 is zero.

With $-\nabla\psi = \bar{E} + i\omega\bar{A}$ and $\bar{A}(x) = \int_V \mu G_0(x,y)\bar{J}(y)dy$, the integral equation above can be written as:

$$\int_S G_0(x,y)\frac{\partial \bar{E}(y)}{\partial n_y}dy - \int_S \frac{\partial G_0(x,y)}{\partial n_y}\bar{E}(y)dy + \nabla\psi(x) = 0 \tag{3.19}$$

This integral equation relates the gradient of the scalar potential at any point in the space to the electrical field and the normal derivative of electrical field on the surface S.

With x moved to the interior of S, a dyadic surface integral equation can be derived which is based on the electrical field, the normal derivative of the electrical field and the gradient of scalar potential:

$$\int_S G_0(x,y)\frac{\partial \bar{E}(y)}{\partial n_y}dy - \int_S \frac{\partial G_0(x,y)}{\partial n_y}\bar{E}(y)dy + \nabla\psi(x) = 0 \qquad (3.20)$$

Again, the singularity in the integration is not removed.

3.3 The surface integral form for current conservation

In (3.17) and (3.20), there are three unknowns, $\bar{E}$, $\frac{\partial \bar{E}}{\partial n}$ and ψ. These two equations can be understood as the surface integral form of the constitutive relationship of $-\nabla\psi = \bar{E} + i\omega\bar{A}$, because they relates $\nabla\psi$ to $\bar{E}$ and $\frac{\partial \bar{E}}{\partial n}$. Since (3.17) shows that $\frac{\partial \bar{E}}{\partial n}$ can be uniquely determined with $\bar{E}$, (3.17) and (3.20) essentially relate $\nabla\psi$ to $\bar{E}$. This section gives another basic relationship: the surface integral form of current conservation.

It has been proved that $\nabla \cdot \bar{E} = 0$ is valid for the impedance extraction problem considered. For a surface formulation, a surface form of $\nabla \cdot \bar{E} = 0$ must be derived.

To get the equation for E for certain part of the surface from current conservation, it is necessary to consider some volume associated with this piece of surface. For a certain area a of the conductor surface S encircled by a closed path of C shown in Figure 3-4, consider the current conservation for a box inside the conductor volume right underneath a with thickness δ. The top of the box is on the interior of S and the bottom is off S by a small distance of δ.

The current flowing in from the top, the bottom and the sides of the box should add up to zero. With the fact that the top and the bottom are very close, the equation of the current conservation can be written as:

$$\int_C \delta E_t \cdot (n(x) \times l(x))dx - \int_{a_1}^{b_1}\int_{a_2}^{b_2}(E_{n(y)}(t_1,t_2,0) - E_{n(y)}(t_1,t_2,-\delta))dt_1dt_2 = 0 \quad (3.21)$$

where a_1, b_1, a_2 and b_2 are the integration boundaries. In equation (3.21), the integration

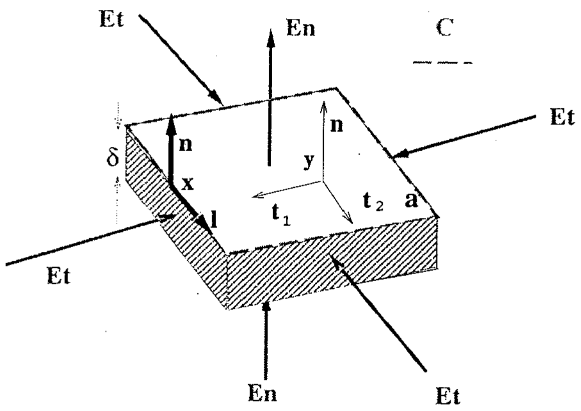

FIGURE 3-4: A thin box for surface current conservation

along C accounts for the contribution of E_t from the side, while the 2-D integration accounts for the contribution of E_n from the top and the bottom.

For an arbitrary point y on the top of the box, the coordinate is $(t_1, t_2, 0)$ under the local coordinate system. The local axes are $n(y)$, t_1 and t_2, where $n(y)$ is the unit normal direction vector, while t_1 and t_2 are two tangential vectors. For an arbitrary point x on C, $n(x)$ is the unit normal vector, $l(x)$ is the unit vector along C, and $n(x) \times l(x)$ indicates the direction for the current to flow into the box through the side.

Let δ approach zero and apply a Taylor expansion to the integrands of the 2-D integration in (3.21), then we have the surface form of the current conservation law:

$$\int_C E_t(x) \cdot (n(x) \times l(x))dx - \int_a \frac{\partial E_n(y)}{\partial n(y)} dy = 0 \qquad (3.22)$$

3.4 The capacitive surface integral equation and boundary conditions

3.4.1 Capacitive surface integral equation

As has been shown in the section on time harmonic Maxwell's equations, the charge is just on the surface of the conductors. The relationship between the charge and the scalar potential is

$$\psi(x) = \int_S G_0(x,y)\frac{\rho(y)}{\epsilon}dy \tag{3.23}$$

where G_0 is the same Green's function used in the second dyadic surface integral equation (3.20).

3.4.2 Boundary conditions

(3.17), (3.20), (3.22) and (3.23) are the basic equations of the new surface formulation. However, special care should be taken about (3.20). Unlike (3.17) which has equations in three directions, the normal direction of (3.20) is not available to the surface representation, because it requires the normal derivative of ψ. To make up the equation in the normal direction, the normal boundary condition can be used.

It is well known [3, 2] that the charge conservation law applied to the small area around a point on S gives the normal boundary condition for E_n and ρ

$$E_n = \frac{i\omega\rho}{\sigma} \tag{3.24}$$

where E_n is at the interior of S.

For magnetoquasistatics(MQS) impedance extraction, the charge density is assumed to be zero and the normal boundary condition should be

$$E_n = 0 \tag{3.25}$$

In addition, special care should be taken for the surface where the terminal is attached, which we call contact surface. For these contact surface, the normal boundary condition can not be used because the surface is not the interface between the conductor and the air, as is the case for a non-contact surface. For a contact surface, we assume E_t is zero, so that $\frac{\partial \bar{E}_n}{\partial n}$ is zero if (3.22) is also applied. Intuitively, $\frac{\partial \bar{E}_n}{\partial n} = 0$ at the contact surface means the input current is not changing in the normal direction.

The other boundary condition is that the potential at the contact surface is given.

Therefore, the boundary conditions are:

1. For non-contact surface, apply $E_n = \frac{i\omega\rho}{\sigma}$ in the case of general EMQS impedance extraction, but apply $E_n = 0$ in the case of MQS impedance extraction.
2. For contact surface, apply $\frac{\partial \bar{E}_n}{\partial n} = 0$.
3. For the contact surface, ψ is set to ψ_+ or ψ_- depending on the polarity of the terminal(contact).

4

Discretization

In order to solve the system of integral equations of (3.17), (3.20), (3.22) and (3.23), consider discretizing the surface into N quadrilateral panels, which have M vertices. Among these panels and vertices, N^C panels and M^C vertices are on the contact while N^{NC} panels and M^{NC} vertices are not. In such a discretization, a quadrilateral panel vertex will be shared by four panels. We associate 7 unknowns with each panel: $\frac{\partial E_x}{\partial n}$, $\frac{\partial E_y}{\partial n}$, $\frac{\partial E_z}{\partial n}$, E_x, E_y,E_z and ρ, where ρ is the charge density. The scalar potential is associated with the panel vertices. The panel discretization and the associated unknowns are shown in Figure 4-1.

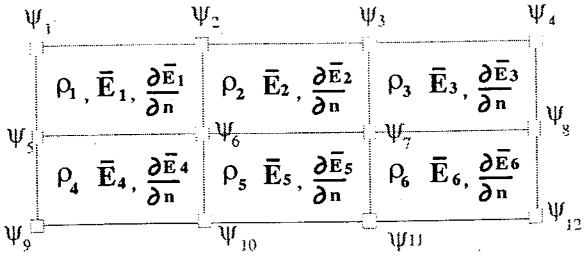

ψ_1
ψ_2
ψ_3
ψ_4
$\rho_1, \bar{E}_1, \frac{\partial \bar{E}_1}{\partial n}$
$\rho_2\ \bar{E}_2, \frac{\partial \bar{E}_2}{\partial n}$
$\rho_3\ \bar{E}_3, \frac{\partial \bar{E}_3}{\partial n}$
ψ_5
ψ_6
ψ_7
ψ_8
$\rho_4\ \bar{E}_4, \frac{\partial \bar{E}_4}{\partial n}$
$\rho_5\ \bar{E}_5, \frac{\partial \bar{E}_5}{\partial n}$
$\rho_6\ \bar{E}_6, \frac{\partial \bar{E}_6}{\partial n}$
ψ_9
ψ_{10}
ψ_{11}
ψ_{12}

FIGURE 4-1: The discretization of the surface

The panel unknowns are assumed to be constant over a panel, and the collocation point is set at the center of the panel, as shown in Figure 4-2.

4.1 Discretization of the first dyadic surface integral equation

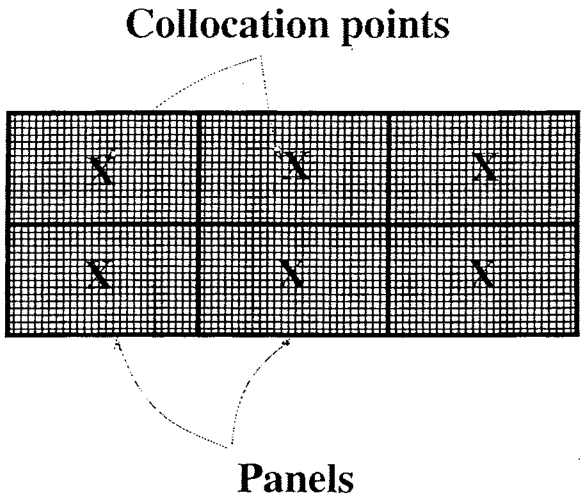

FIGURE 4-2: The centroid collocation scheme

If centroid collocation is applied to the dyadic integral equation (3.17), the result is a dyadic linear equation

$$P_1 \frac{\partial \bar{E}}{\partial n} - D_1 \bar{E} = 0 \tag{4.1}$$

where P_1 and D_1 are both N by N,

$$\begin{aligned} P_1(i,j) &= \int_{panel_j} G_1(x_i, y) dy \\ D_1(i,j) &= \int_{panel_j} \frac{\partial G_1}{\partial n_y}(x_i, y) dy \end{aligned}$$

and x_i is the i^{th} collocation point. With the singularity term already considered, D_1 is the discretization of the dipole potential operator of the $\frac{e^{iK_1 r}}{4\pi r}$ kernel, and

$$D_1(i,i) = \frac{1}{2}, \; i = 1, \ldots, N$$

It is worth noting that for the multiple conductor case, there is no coupling between conductors in equation (3.17), so that if panel i and panel j do not belong to the same conductor,

$$P_1(i,j) = D_1(i,j) = 0$$

therefore, (4.1) can be taken as independent equations for every conductor.

For example, if there are four conductors in the problem(Figure 4-3), P_1 consists of four diagonal blocks as shown in Figure 4-4, where each diagonal block comes from the discretization of (3.17) for one conductor. The number of rows and the number of columns of a diagonal block are the same as the number of panels of the correspondent conductor. The same is ture for D_1.

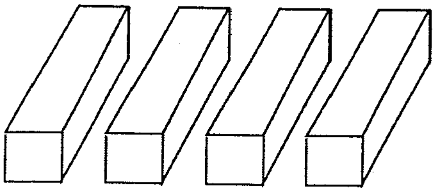

FIGURE 4-3: A four conductor problem

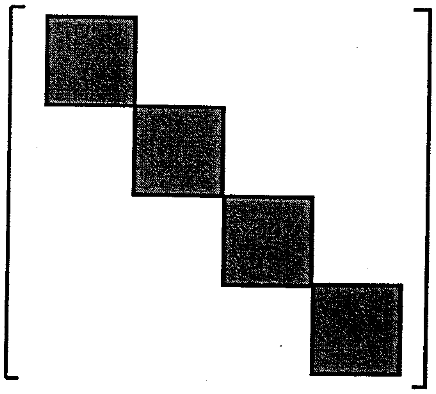

FIGURE 4-4: P_1 matrix of a four conductor problem

Equation (3.17) is actually three independent equations:

$$\begin{aligned} P_1\frac{\partial \bar{E}_x}{\partial n} - D_1\bar{E}_x &= 0 \\ P_1\frac{\partial \bar{E}_y}{\partial n} - D_1\bar{E}_y &= 0 \\ P_1\frac{\partial \bar{E}_z}{\partial n} - D_1\bar{E}_z &= 0 \end{aligned} \tag{4.2}$$

4.1.1 Discretization of the second dyadic surface integral equation

Collocation applied to (3.20) will result in an equation similar in form to (4.1) with a $\nabla\psi$ term introduced. The $\nabla\psi$ term in the normal direction is difficult to compute as the surface-normal derivative of the potential can not be evaluated using only the vertex potentials. Instead, consider applying collocation to (3.20) to get the discretized equation (4.3) then extracting out only the surface tangential components from it.

Another dyadic linear equation comes directly from applying collocation to the dyadic integral equation(3.20):

$$P_0\frac{\partial \bar{E}}{\partial n} - (D_0 - I)\bar{E} + \nabla\psi = 0 \tag{4.3}$$

which can be written in three independent directions as

$$\begin{aligned} P_0\frac{\partial \bar{E}_x}{\partial n} - (D_0 - I)\bar{E}_x + \nabla_x\psi = 0 \\ P_0\frac{\partial \bar{E}_y}{\partial n} - (D_0 - I)\bar{E}_y + \nabla_y\psi = 0 \\ P_0\frac{\partial \bar{E}_z}{\partial n} - (D_0 - I)\bar{E}_z + \nabla_z\psi = 0 \end{aligned} \tag{4.4}$$

where P_0, D_0 and the identity matrix I are all N by N,

$$\begin{aligned} P_0(i,j) &= \int_{panel_j} G_0(x_i, y)dy \\ D_0(i,j) &= \int_{panel_j} \frac{\partial G_0}{\partial n_y}(x_i, y)dy \end{aligned}$$

D_0 is the discretization of the dipole operator of $G_0(r) = \frac{1}{4\pi r}$ kernel, and $-I$ comes from the fact that the unit singularity of $\bar{E}$ is absorbed into $\nabla\psi$. The diagonal entries of D_0 are

$$D_0(i,i) = \frac{1}{2},\ i = 1, \ldots, N$$

$\nabla\psi$ at panel j in direction t is the combination of three components:

$$\nabla_t\psi_j = t_x\nabla_x\psi_j + t_y\nabla_y\psi_j + t_z\nabla_z\psi_j$$

where $t = (t_x, t_y, t_z)$.

The same idea can be used for all of the panels at the same time. Pick a unit tangential vector for each panel, and form diagonal matrices T_{1_x}, T_{1_y} and T_{1_z} with the entries as the x, y, z coordinates of the vectors, i.e, the tangential vector of panel j is $(T_{1_x}(j,j), T_{1_y}(j,j), T_{1_z}(j,j))$. Then the tangential gradient of ψ on the panels at the corresponding tangential directions can be written as

$$\nabla_{T_1}\psi = T_{1_x}\nabla_x\psi + T_{1_y}\nabla_y\psi + T_{1_z}\nabla_z\psi$$

With $\nabla_x\psi$, $\nabla_y\psi$, $\nabla_z\psi$ substituted using (4.4), resulting equation is

$$T_{1_x}(P_0\frac{\partial\bar{E}_x}{\partial n}-(D_0-I)\bar{E}_x)+T_{1_y}(P_0\frac{\partial\bar{E}_y}{\partial n}-(D_0-I)\bar{E}_y)+T_{1_z}(P_0\frac{\partial\bar{E}_z}{\partial n}-(D_0-I)\bar{E}_z)+\nabla_{T_1}\psi = 0$$

where $\nabla_{T_1}\psi$ denotes the gradient of ψ on the panels at the corresponding tangential directions set by T_1 matrices.

$T_{2_x}, T_{2_y}, T_{2_z}$ can be formed by picking another set of tangential vectors, with the vector of every panel in a different direction to the corresponding one in the first set. A similar equation holds:

$$T_{2_x}(P_0\frac{\partial\bar{E}_x}{\partial n}-(D_0-I)\bar{E}_x)+T_{2_y}(P_0\frac{\partial\bar{E}_y}{\partial n}-(D_0-I)\bar{E}_y)+T_{2_z}(P_0\frac{\partial\bar{E}_z}{\partial n}-(D_0-I)\bar{E}_z)+\nabla_{T_2}\psi = 0$$

For any panel, two independent tangential directions can be found. As shown in Figure4-5, two tangential directions t_a and t_b are formed by connecting the midpoints of the sides. The representation of the tangential $\nabla\psi$ can be achieved using finite differences.

For example, the gradient of ψ along t_a can be computed with

$$\nabla_{t_a}\psi = \frac{\psi_2 + \psi_3 - \psi_1 - \psi_4}{2|M_{14}M_{23}|}$$

where ψ_1, ψ_2, ψ_3 and ψ_4 are the potential at the vertices V_1, V_2, V_3 and V_4, M_{12}, M_{23}, M_{34} and M_{14} are the midpoints of the sides of the panel, whereas $|M_{14}M_{23}|$ is the length of line $M_{14}M_{23}$.

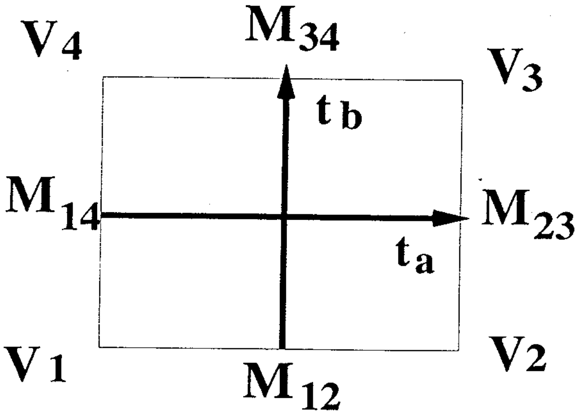

FIGURE 4-5: Computation of the gradient of potential

With the finite difference matrix denoted with A_T, the final discretized form of (3.20) in the tangential direction can be written as

$$\begin{aligned}
T_{1_x}(P_0\frac{\partial \bar{E}_x}{\partial n} - (D_0 - I)\bar{E}_x) + T_{1_y}(P_0\frac{\partial \bar{E}_y}{\partial n} - (D_0 - I)\bar{E}_y) + T_{1_z}(P_0\frac{\partial \bar{E}_z}{\partial n} - (D_0 - I)\bar{E}_z) + A_{T_1}\psi = 0 \\
T_{2_x}(P_0\frac{\partial \bar{E}_x}{\partial n} - (D_0 - I)\bar{E}_x) + T_{2_y}(P_0\frac{\partial \bar{E}_y}{\partial n} - (D_0 - I)\bar{E}_y) + T_{2_z}(P_0\frac{\partial \bar{E}_z}{\partial n} - (D_0 - I)\bar{E}_z) + A_{T_2}\psi = 0
\end{aligned} \tag{4.5}$$

where T_{1_x}, T_{1_y}, T_{1_z}, T_{2_x}, T_{2_y}, T_{2_z}, A_{T_1} and A_{T_2} are all N by N matrices.

4.2 Discretization of the integral form of current conservation

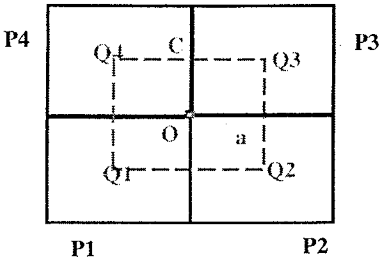

FIGURE 4-6: Dual panel for current conservation

Consider the dual panel of four panels P_1, P_2, P_3 and P_4 (Figure 4-6) for resolving the potential at the shared non-contact vertex O. The dual panel a is encircled by the dashed line C, which connects the four panel centroids. Applying the surface integral equation of (3.22) to the dual panel leads to the equation

$$\int_C E_t(x) \cdot (n(x) \times l(x))dx - \int_a \frac{\partial E_n(y)}{\partial n(y)} dy = 0$$

where $E_t(x)$ and $\frac{\partial E_n(y)}{\partial n(y)}$ in (3.22) can be approximated by averaging the electrical field and the electrical field derivatives of the panels nearby.

With constant electrical field and its normal derivative are assumed on each panel, the coefficients of E_x, E_y, E_z, $\frac{\partial E_x}{\partial n}$, $\frac{\partial E_y}{\partial n}$ and $\frac{\partial E_z}{\partial n}$ in the discretized equation can be computed by looking at one panel at a time. Take the field and its normal derivative at panel P_1 for example, the coefficients of them can be computed by evaluating the integration related to P_1 part of the dual panel, which is a_1 (quadrilateral $Q_1M_{14}OM_{12}$ in Figure 4-7).

In Figure 4-7, M_{14} is on the shared side of P_1 and P_4, M_{12} is on the shared side of P_1 and P_2, l_1 is the unit vector in the direction of $M_{14}Q_1$, l_2 is the unit vector in the direction of Q_1M_{12}, n is the unit normal vector of a_1, t_1 is $n \times l_1$ and t_2 is $n \times l_2$. The coordinates of t_1, t_2 and n are $[t_{1_x}, t_{1_y}, t_{1_z}]$, $[t_{2_x}, t_{2_y}, t_{2_z}]$, and $[n_x, n_y, n_z]$.

Based on the constant electrical field and its normal derivative assumption on P_1, the coefficients of the field quantities in the integration are:

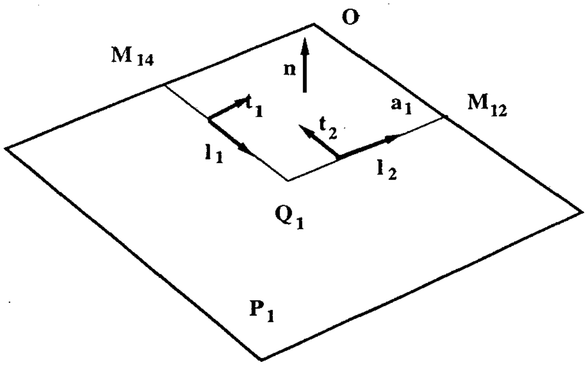

FIGURE 4-7: The decomposition of the dual panel

1. E_x: $|Q_1M_{14}|t_{1_x} + |Q_1M_{12}|t_{2_x}$
2. E_y: $|Q_1M_{14}|t_{1_y} + |Q_1M_{12}|t_{2_y}$
3. E_z: $|Q_1M_{14}|t_{1_z} + |Q_1M_{12}|t_{2_z}$
4. $\frac{\partial E_x}{\partial n}$: $-n_x s_{a_1}$
5. $\frac{\partial E_y}{\partial n}$: $-n_y s_{a_1}$
6. $\frac{\partial E_z}{\partial n}$: $-n_z s_{a_1}$

where s_{a_1} is the area of a_1.

The matrix form of the equation applied to the dual panels formed for non-contact vertices is:

$$C_{d_x}\frac{\partial E_x}{\partial n} + C_{d_y}\frac{\partial E_y}{\partial n} + C_{d_z}\frac{\partial E_z}{\partial n} + C_x E_x + C_y E_y + C_z E_z = 0 \tag{4.6}$$

where C_x, C_y, C_z, C_{d_x}, C_{d_y} and C_{d_z} are the matrices formed by the coefficients of E_x, E_y, E_z, $\frac{\partial E_x}{\partial n}$, $\frac{\partial E_y}{\partial n}$ and $\frac{\partial E_z}{\partial n}$ in the surface form equation of current conservation (3.22). C_x, C_y, C_z, C_{d_x}, C_{d_y} and C_{d_z} are all M^{NC} by N.

This equation is used to resolve the potential of the non-contact vertices, or, the vertices not on the contact panels. For the vertices on the contact panels, the potential boundary condition can be applied.

4.3 Discretization of the capacitive integral equation

Through the discretization of (3.23), the charge density on a panel can be related to the weighted average of the panel's vertex potentials with

$$P_0\rho - \epsilon A_p\psi = 0 \tag{4.7}$$

where A_p is the matrix of potential averaging coefficients that relates the potential at the centroids to the potential at the vertices. A_p is N by N.

Consider a panel in Figure 4-8 for example, the potential at the center of the quadrilateral panel is computed by averaging the potential of the panel vertices

$$\psi_Q = \sum_{i=1}^{4} \frac{1}{4}\psi(v_i)$$

where ψ_1, ψ_2, ψ_3 and ψ_4 are the potential at the vertices V_1, V_2, V_3 and V_4, while Q is the centroid of the panel.

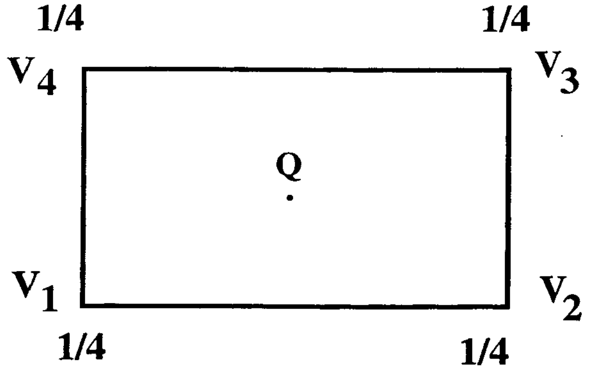

FIGURE 4-8: The computation of the centroid potential

4.4 Applying the boundary condition in the discretization

The discretization of the the normal boundary conditions consists of applying the normal boundary condition to the panels.

1. If panel j is a non-contact panel, then

   $$n(j) \cdot \bar{E}(j) = \frac{i\omega\rho(j)}{\sigma} \tag{4.8}$$

   is applied in the EMQS case, but

   $$n(j) \cdot \bar{E}(j) = 0 \tag{4.9}$$

   is applied in the MQS case.

2. If panel j is a contact panel,

   $$n(j) \cdot \frac{\partial \bar{E}(j)}{\partial n} = 0 \tag{4.10}$$

   is applied.

The matrix form of (4.8) is

$$N_{NC_x}E_x + N_{NC_y}E_y + N_{NC_z}E_z + W\rho = 0 \tag{4.11}$$

where N_{NC_x}, N_{NC_y} and N_{NC_z} are N^{NC} by N matrices formed by X, Y, Z coordinates of the unit normal vectors at the non-contact panels, and W is formed by the entries of $-\frac{i\omega}{\sigma}$. These matrices have N_{NC} rows because the equations are for the non-contact panels. Note that zeros are padded for the columns related to contact panels.

Similarly, the matrix form of (4.9) is

$$N_{NC_x}E_x + N_{NC_y}E_y + N_{NC_z}E_z = 0 \tag{4.12}$$

And the matrix form of (4.10) is

$$N_{C_x}\frac{\partial E_x}{\partial n} + N_{C_y}\frac{\partial E_y}{\partial n} + N_{C_z}\frac{\partial E_z}{\partial n} = 0 \tag{4.13}$$

where N_{C_x}, N_{C_y} and N_{C_z} are N^C by N matrices formed by X, Y, Z coordinates of the unit normal vectors at the contact panels. These matrices have N_C rows because the equations are for the contact panels. Note that zeros are padded for the columns related to non-contact panels.

The potential boundary condition is applied to the contact panels. If panel j is a contact panel, then

$$\psi_{v_j} = \psi_c \tag{4.14}$$

for vertex v_j of the panel. In (4.14), ψ_c is the given potential on the contact. Typically, ψ_c is set to $+\frac{1}{2}$ for the positive contact and $-\frac{1}{2}$ for the negative contact.

The matrix form of (4.14) is

$$I_C\psi = \psi_c \tag{4.15}$$

where I_C is M^C by N. I_C has M^C rows because the boundary condition is applied to the contact vertices. Note that the columns related to non-contact vertices are padded with zero's.

4.5 The linear system and the computation of the input current

4.5.1 The linear systems for EMQS and MQS impedance extraction

The discretized equations (4.2), (4.5), (4.11), (4.13), (4.6), (4.15) and (4.7) can be summarized as the linear system of $7N + M$ eqations and $7N + M$ unknowns for EMQS impedance extraction:

$$
\left[\begin{array}{|c|c|c|c|c|c|c|c|}
\hline
P_1 & & & -D_1 & & & & \\
\hline
 & P_1 & & & -D_1 & & & \\
\hline
 & & P_1 & & & -D_1 & & \\
\hline
T_{1_x}P_0 & T_{1_y}P_0 & T_{1_z}P_0 & -T_{1_x}(D_0 - I) & -T_{1_y}(D_0 - I) & -T_{1_z}(D_0 - I) & A_{t_1} & \\
\hline
T_{2_x}P_0 & T_{2_y}P_0 & T_{2_z}P_0 & -T_{2_x}(D_0 - I) & -T_{2_y}(D_0 - I) & -T_{2_z}(D_0 - I) & A_{t_2} & \\
\hline
 & & & N_{NC_x} & N_{NC_y} & N_{NC_z} & & W \\
\hline
N_{C_x} & N_{C_y} & N_{C_z} & & & & & \\
\hline
C_{d_x} & C_{d_y} & C_{d_z} & C_x & C_y & C_z & & \\
\hline
 & & & & & & I_C & \\
\hline
 & & & & & & -\epsilon A_p & P_0 \\
\hline
\end{array}\right]
\begin{bmatrix}
\frac{\partial E_x}{\partial n} \\
\frac{\partial E_y}{\partial n} \\
\frac{\partial E_z}{\partial n} \\
E_x \\
E_y \\
E_z \\
\psi \\
\rho
\end{bmatrix}
= b
\tag{4.16}
$$

where the first three rows correspond to the discretized first dyadic surface integral equation (4.2), the fourth and the fifth row correspond to the discretization and tangential combination of the second dyadic surface integral equation (4.5), the sixth row corresponds to the normal boundary condition for non-contact panels in the EMQS case(4.11), the seventh row corresponds to the normal boundary condition for contact panels (4.13), the eighth row corresponds to the discretization of surface current conservation equation (4.6) applied to non-contact panels, the ninth row corresponds to the potential boundary condition applied to contact vertices(4.15), and the tenth row corresponds to the discretization of the capacitive equation (4.7).

In the MQS impedance extraction case, the charge can be dropped out, and the normal boundary condition for non-contact panels for MQS analysis is used. The discretized equations (4.2), (4.5), (4.12), (4.13), (4.6), (4.15) form the linear system of $6N + M$ eqations and $6N + M$ unknownsfor MQS impedance extraction:

$$\left[\begin{array}{|c|c|c|c|c|c|c|}
\hline
P_1 & & & -D_1 & & & \\
\hline
 & P_1 & & & -D_1 & & \\
\hline
 & & P_1 & & & -D_1 & \\
\hline
T_{1_x}P_0 & T_{1_y}P_0 & T_{1_z}P_0 & -T_{1_x}(D_0-I) & -T_{1_y}(D_0-I) & -T_{1_z}(D_0-I) & A_{t_1} \\
\hline
T_{2_x}P_0 & T_{2_y}P_0 & T_{2_z}P_0 & -T_{2_x}(D_0-I) & -T_{2_y}(D_0-I) & -T_{2_z}(D_0-I) & A_{t_2} \\
\hline
 & & & N_{NC_x} & N_{NC_y} & N_{NC_z} & \\
\hline
N_{C_x} & N_{C_y} & N_{C_z} & & & & \\
\hline
C_{d_x} & C_{d_y} & C_{d_z} & C_x & C_y & C_z & \\
\hline
 & & & & & & I_C \\
\hline
\end{array}\right]
\begin{bmatrix} \frac{\partial E_x}{\partial n} \\ \frac{\partial E_y}{\partial n} \\ \frac{\partial E_z}{\partial n} \\ E_x \\ E_y \\ E_z \\ \psi \end{bmatrix} = b \tag{4.17}$$

In the block matrices of (4.16) and (4.17), only P_0, D_0, P_1 and D_1 are dense.

4.5.2 Current computation, impedance extraction and circuit parameter extraction

Once the linear system is solved, the current flowing into the conductors can be computed. As shown in Figure 4-9, current I flowing into contact C_+ can be computed by summing up the current flowing into the panels on the contact with (4.18). Note that n_+ is opposite to the direction of the current flow.

$$I = \sum_{panel_j \in C_+} -\sigma(n_+ \cdot E_j)s_j \tag{4.18}$$

where s_j is the area of panel j.

For two port impedance extraction, a linear system of equation can be set up at certain frequency f with a unit potential difference applied to the two terminals. After the linear system of equation is solved and I is computed, the impedance at the frequency

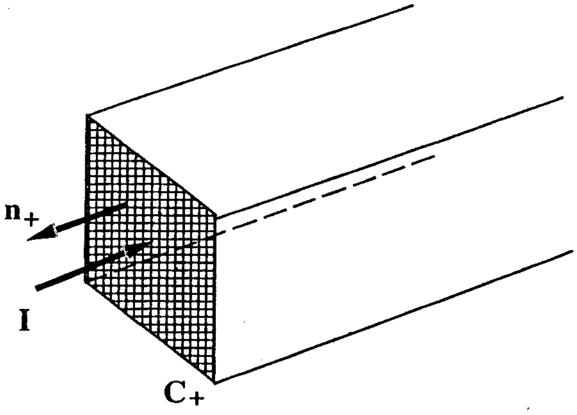

FIGURE 4-9: The summation of the current

of f is

$$Z = \frac{1}{I}$$

The resistance and effective inductance at the frequency of f can be computed with

$$R = real(Z)$$

and

$$L_{eff} = \frac{imag(Z)}{\omega}.$$

Then a simple circuit approximation of the conductor at the frequency f is a resistor of R and an inductor of L_{eff} in series. For MQS analysis, L_{eff} reflects inductance effect of the conductor, while it reflects the coupled inductance and capacitance effects for EMQS analysis.

For the case with multiple voltage sources or current sources, use the technique in chapter 2 is used. After the impedance matrix Z is computed, the resistance matrix and inductance matrix can be extracted as:

$$R = real(Z)$$

and

$$L_{eff} = \frac{imag(Z)}{\omega}.$$

5

Low frequency and high frequency problems

5.1 The low frequency problem

At sufficiently low frequencies, the discretized formulation for MQS analysis generates an impedance with the imaginary part that decreases more like $\sqrt{\omega}$ than like ω. In this section, Taylor expansion at low frequency is used to show that a $\sqrt{\omega}$ term actually exists in the Green's function kernel in the first dyadic integral equation (3.17), but it should have zero contribution to the linear system of equations if there is no numerical error in the discretization, because the impact of this term is proportional to the product of three operators which turns out to be zero. However, the numerical errors in the discretization of these operators often lead to a nonzero product of them, and the impact of $\sqrt{\omega}$ term can be significant because the $\sqrt{\omega}$ term can dominate the ω term at low frequencies. Linearization of the Green's function kernel in respect to ω at low frequencies is used for the surface formulation to eliminate the $\sqrt{\omega}$ problem completely.

There is a second problem at high frequency. The current at high frequency is crowded near the surface due to the skin effect, and this means that the contact surfaces need very fine discretization because a contact is just like a cross section inside the volume. To avoid fine and adaptive meshing of the contact surfaces at higher and higher frequencies, the magnetic field around a cross section nearby the contact is used to compute the current.

With more mathematical manipulation, the current can be computed with the electrical field and its normal derivative on the non-contact surface near the contact. In this way, the need to use fine discretization for the contacts at high frequencies is eliminated.

5.1.1 $\sqrt{\omega}$ term at low frequency

To check the formulation, MQS impedance extraction is performed first on a ring example. The ring has a diameter of 10 μm. The cross-section is a square of approximately 5 μm by 5 μm and σ is 54 mho μm. In the discretization of the problem shown in Figure 5-1, the loop is broken into 12 segments.

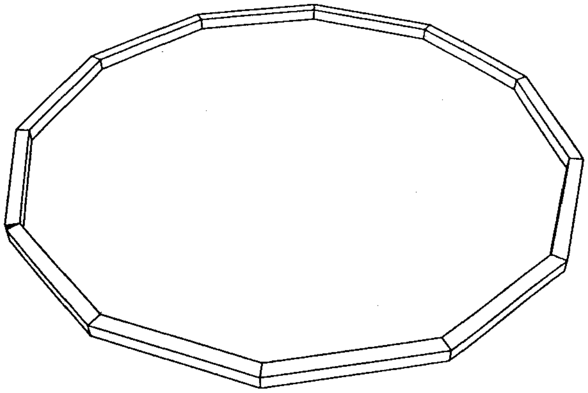

FIGURE 5-1: The discretized ring

MQS impedance extraction is performed for the ring example because a ring has a low frequency analytic formula for inductance, and the low frequency resistance can also be easily estimated with Ohm's Law.

Because the low frequency impedance should be $R + i\omega L$, the imaginary part of the impedance Z should change proportionally with ω in the low frequency range.

The simulation result, however, is different from the expectation. From Figure 5-2, it is obvious that $imag(Z)$ does not change linearly with frequency. As the frequency changes from 10^5 Hz to 10^2 Hz, $imag(Z)$ decreases by less than one magnitude instead of decreasing by three magnitudes.

To understand this problem, careful low frequency analysis was carried out for (4.17),

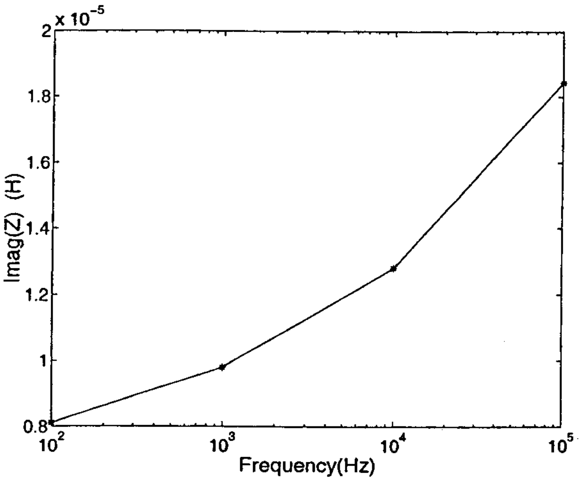

FIGURE 5-2: The abnormal behavior at low frequency

which can be written as:

$$A(\omega)x = b$$

The right hand side is always real, with the entries zero or the value of the applied potential. The matrix is frequency dependent, but this dependency on ω only comes from the block matrices of P_1 and D_1.

If every entry from these blocks can be approximated by a real constant plus an $O(i\omega)$ term, then $A(\omega)$ can be approximated with $A_1 + i\omega A_2$, where A_1 and A_2 are real and independent of ω. If this is the case, the solution of $A(\omega)x = b$ has negligible higher than $O(\omega)$ terms, and so does the current. As a result, Z should have a imaginary part linearly dependent on ω.

However, this is not the case. The entries of P_1 and D_1 take the form of

$$\begin{aligned} P_1(i,j) &= \int_{panel_j} G_1(x_i, y)dy \\ D_1(i,j) &= \int_{panel_j} \frac{\partial G_1}{\partial n_y}(x_i, y)dy \end{aligned}$$

where

$$G_1(x,y) = \frac{e^{iK_1|x-y|}}{4\pi|x-y|}, \; K_1 = \sqrt{-i\omega\mu\sigma} = \sqrt{\frac{\omega\mu\sigma}{2}}(-1+i) \qquad (5.1)$$

Since K_1 is $O(\sqrt{\omega})$, the Taylor expansion for $\frac{e^{iK_1 r}}{r}$ in terms of K_1 is:

$$\frac{e^{iK_1 r}}{r} = \frac{1}{r} + iK_1 + \frac{1}{r}\frac{(iK_1)^2 r^2}{2} + o(\omega) \tag{5.2}$$

In the expansion, the first term is a real constant and third term is actually $\frac{1}{r}\frac{(i\omega\sigma)r^2}{2}$, which is imaginary and linear in ω. The second term is $O(K_1)$ with a factor of $\sqrt{\frac{\omega\mu\sigma}{2}}(-1-i)$, which has an imaginary term of the order $\sqrt{\omega}$!

Obviously, the $O(K_1)$ term is the source of the nonlinear dependency of $imag(Z)$ on the frequency. The same problem might exist in $\frac{\partial G_1(r)}{\partial n}$.

5.1.2 The elimination of the $\sqrt{\omega}$ term and the justification

The existence of the $\sqrt{\omega}$ term in the matrix entry seems to be contradictory to physical analysis. Certainly it can be eliminated by throwing away the K_1 term in the right hand side of (5.2), which is the source of $\sqrt{\omega}$. The terms of higher order than the third term are negligible. This can be taken as a linearization in terms of ω. The linearized form of (5.2) is:

$$\frac{e^{iK_1 r}}{r} = \frac{1}{r} + \frac{1}{r}\frac{(iK_1)^2 r^2}{2} \tag{5.3}$$

However, it remains to be proved that the $O(\sqrt{\omega})$ term can be eliminated mathematically. To prove this, a Taylor expansion will be performed on $G_1(r)$ and $\frac{\partial G_1(r)}{\partial n}$ to second order in K_1, then the order K_1 terms will be shown to have zero impact in the formulation.

The expansion of the monopole and dipole kernel is:

$$\frac{e^{iK_1 r}}{r} \approx \frac{1}{r} + iK_1 - \frac{{K_1}^2 r}{2} \tag{5.4}$$

and

$$\frac{\partial}{\partial n}\frac{e^{iK_1 r}}{r} \approx \frac{iK_1 r - 1}{r^2} e^{iK_1 r}\frac{\partial r}{\partial n}$$

$$\begin{aligned}
&\approx \frac{iK_1r-1}{r^2}(1+iK_1r+\frac{iK_1r^2}{2})\frac{\partial r}{\partial n} \\
&\approx -\frac{1-iK_1r}{r^2}(1+iK_1r+\frac{iK_1r^2}{2})\frac{\partial r}{\partial n} \\
&\approx -(\frac{1+K_1r^2}{r^2}+\frac{1-iK_1r}{r^2}\frac{iK_1r^2}{2})\frac{\partial r}{\partial n} \\
&\approx -\frac{1}{r^2}\frac{\partial r}{\partial n}-\frac{{K_1}^2}{2}\frac{\partial r}{\partial n} \\
&\approx \frac{\partial}{\partial n}\frac{1}{r}-\frac{{K_1}^2}{2}\frac{\partial r}{\partial n}
\end{aligned}$$

The final expansion result for the dipole can be written as:

$$\frac{\partial}{\partial n}\frac{e^{iK_1r}}{r} \approx \frac{\partial\frac{1}{r}}{\partial n}-\frac{{K_1}^2}{2}\frac{\partial r}{\partial n} \tag{5.5}$$

It is clear from (5.4) and (5.5) that the K_1 term is automatically eliminated in the dipole kernel expansion, but it exists in the monopole kernel expansion.

For the single conductor case, the definition of P_1 and D_1 for the discretized surface is:

$$\begin{aligned}
P_1(j,k) &= \int_{panel_k} G_1(x_j,y)dy \\
D_1(j,k) &= \int_{panel_k} \frac{\partial G_1}{\partial n_y}(x_j,y)dy
\end{aligned}$$

where x_j is the center of panel j.

Based on (5.4) , P_1 can be expanded as

$$P_1 \approx P_0 + iK_1P_a + P_{LM} \tag{5.6}$$

where

$$P_a(j,k) = s_k$$

$$P_{LM}(j,k) = -\frac{{K_1}^2}{2}\int_{panel_k}|x_j-y|dy$$

and s_k is the area of panel k.

Similarly, D_1 can be expanded based on (5.5):

$$D_1 = D_0 + D_{LD} \tag{5.7}$$

where

$$D_{LD}(j,k) = -\frac{{K_1}^2}{2}\int_{panel_k}\frac{\partial|x_j - y|}{\partial n_y}dy$$

In these matrices, P_0, P_a and D_0 are constant, while P_{LM} and P_{LD} are order $O(\omega)$. In the expansions, only iK_1P_a is $O(\sqrt{\omega})$. In addition, P_0 and D_0 are the discretized form of the monopole and dipole electrostatic potential operators on the surface of the conductor.

The impact of P_1 and D_1 to the MQS linear system (4.17) is only reflected in (4.1):

$$P_1\frac{\partial\bar{E}}{\partial n} - D_1\bar{E} = 0$$

Or

$$\frac{\partial\bar{E}}{\partial n} = P_1^{-1}D_1\bar{E}$$

If it can be proved that $P_1^{-1}D_1$ is approximately a constant matrix plus an $O(\omega)$ matrix, then the whole MQS linear system should not be influenced by $O(\sqrt{\omega})$ terms in P_1.

Following is the mathematical manipulation of $P_1^{-1}D_1$ based on dropping the terms smaller than $O(\omega)$, or $O(K_1^2)$:

$$\begin{aligned}
P_1^{-1}D_1 &\approx (P_0 + iK_1P_a + P_{LM})^{-1}(D_0 + D_{LD}) \\
&\approx [(I + iK_1P_aP_0{}^{-1} + P_{LM}P_0{}^{-1})P_0]^{-1}(D_0 + D_{LD}) \\
&\approx P_0{}^{-1}(I + iK_1P_aP_0{}^{-1} + P_{LM}P_0{}^{-1})^{-1}(D_0 + D_{LD}) \\
&\approx P_0{}^{-1}[I - iK_1P_aP_0{}^{-1} - P_{LM}P_0{}^{-1} + (iK_1P_aP_0{}^{-1} + P_{LM}P_0{}^{-1})^{-2}](D_0 + D_{LD}) \\
&\approx P_0{}^{-1}[I - P_{LM}P_0{}^{-1} - iK_1P_aP_0{}^{-1} + (iK_1P_aP_0{}^{-1})^2](D_0 + D_{LD})
\end{aligned}$$

$$\approx \; {P_0}^{-1}[D_0 - P_{LM}({P_0}^{-1}D_0) + D_{LD} - iK_1P_a({P_0}^{-1}D_0) + (iK_1P_a{P_0}^{-1})^2D_0]$$

Among the terms in the square brackets, D_0 is constant, $-P_{LM}({P_0}^{-1}D_0)$ and D_{LD} are $O(\omega)$. It remains to be proved that $-iK_1P_a({P_0}^{-1}D_0)$ and $(iK_1P_a{P_0}^{-1})^2D_0$ are zero. Since both these terms have a factor $P_a({P_0}^{-1}D_0)$, let us prove

$$P_a({P_0}^{-1}D_0) = 0.$$

Note that P_0 and D_0 are both discrete electrostatic operators on a conductor, and P_a consists of the area of the panels. Based on these facts, the proof can be done through electrostatic analysis.

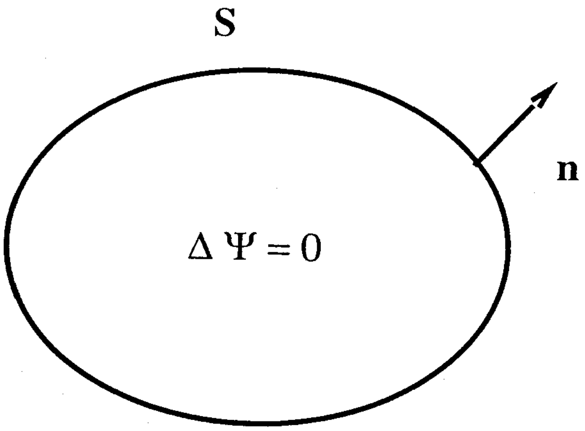

FIGURE 5-3: A conductor under electrostatics

In electrostatics for the conductor in Figure 5-3, the scalar potential ψ satisfies Laplace equation

$$\nabla^2\psi = 0$$

Applying Green's Second Identity to the equation above yields

$$\int_S G_0(x,y)\frac{\partial\psi(y)}{\partial n_y}dy - \int_S \frac{\partial G_0(x,y)}{\partial n_y}\psi(y)dy = \psi(x) \tag{5.8}$$

where x is at the interior of S.

In the discrete form, (5.8) is

$$P_0 \frac{\partial \psi}{\partial n} = D_0 \psi$$

where ψ and $\frac{\partial \psi}{\partial n}$ are the vectors of the scalar potential and its normal derivative at the interior of the surface.

The equation can be also written as:

$$\frac{\partial \psi}{\partial n} = ({P_0}^{-1} D_0)\psi$$

The Laplace equation of ψ can be written as $\nabla \cdot (\nabla \psi) = 0$. With Gauss's Theorem applied to the volume of a conductor, $\nabla \cdot (\nabla \psi) = 0$ leads to

$$\int_S \frac{\partial \psi(y)}{\partial n_y} dy = 0$$

which has the discrete form of

$$\sum_j s_j \frac{\partial \psi_j}{\partial n} = 0 \tag{5.9}$$

where s_j is the area of panel j.

Combined with $P_a(k, j) = s_j$ and $\frac{\partial \psi}{\partial n} = ({P_0}^{-1} D_0)\psi$, equation (5.9) gives

$$P_a({P_0}^{-1} D_0)\psi = 0$$

which holds for arbitrary ψ.

Therefore,

$$P_a({P_0}^{-1} D_0) = 0$$

The proof justifies the approximation

$$P_1^{-1} D_1 \approx {P_0}^{-1}[D_0 - P_{LM}({P_0}^{-1} D_0) + D_{LD}]$$

and the linearization of P_1 and D_1 in terms of ω by:

$$\begin{aligned} P_1 &\approx P_0 + iK_1P_a + P_{LM} \\ D_1 &= D_0 + D_{LD} \end{aligned} \tag{5.10}$$

For the multiple conductor case, the same proof can be used for every conductor separately to justify the linearization because the first equation (4.1) in the MQS linear system (4.17) can be taken as independent equations for every conductor. For the low frequency case of EMQS analysis, the linearization is also necessary.

Even though terms of $O(\sqrt{\omega})$ should have zero impact theoretically, the $O(\sqrt{\omega})$ term still shows up in the numerical experiments such as the ring example when linearization is not used because numerical errors in the discretization and computation are unavoidable. The impact of numerical errors of $O(\sqrt{\omega})$ at low frequency is unpredictable, because $O(\sqrt{\omega})$ is larger in the order than $O(\omega)$.

For the computation of P_1, D_1 the following linearized kernels should be used:

$$\begin{aligned} \frac{e^{iK_1r}}{r} &\approx \frac{1}{r} - \frac{{K_1}^2r}{2} \\ \frac{\partial}{\partial n}\frac{e^{iK_1r}}{r} &\approx \frac{\partial}{\partial n}\frac{1}{r} + \frac{{K_1}^2}{2}\frac{\partial r}{\partial n} \end{aligned} \tag{5.11}$$

For $f < F_L$, the linearization is used to eliminate the $O(\sqrt{\omega})$ term, where F_L can be set at the frequency at which $imag(Z) \approx 0.01real(Z)$. A more formal way of choosing F_L is to make sure that

$$\left|\frac{{K_1}^2r}{2}\right| < \frac{1}{r}$$

for all possible cases of numerical computation.

Provided the largest diameter of the conductor is d_L, we can choose:

$$F_L \approx \frac{1}{\pi {d_L}^2 \mu\sigma}$$

It is worth to note that the exact choice of F_L is not critical to get accurate results.

Take a rectangular wire of 8 μm long, 1 μm wide and 1 μm thick(Figure 5-4) for example, very similar results can be obtained for the frequencies ranging from 10^4 Hz to 10^6 Hz with or without linearization depending on whether F_L is set to be $1.5\,10^6$ Hz or $1.5\,10^3$ Hz (Table 5-1). Table 5-1 shows that the computed imaginary part of the impedance of the wire changes very little when F_L is changed from $1.5\,10^6$ to $1.5\,10^3$. It is also worth to note that F_L should be chosen for every conductor separately because the first dyadic integral equation (3.17) is applied to each conductor independently.

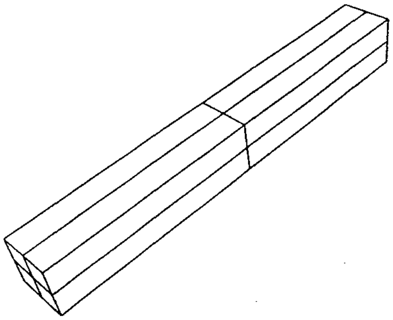

FIGURE 5-4: A discretized wire

F_L	imag(Z) at 1e4 Hz	imag(Z) at 1e5 Hz	imag(Z) at 1e6 Hz
$1.5\,10^6$	2.82709e-07	2.82709e-06	2.82709e-05
$1.5\,10^3$	2.82718e-07	2.82739e-06	2.82803e-05

Table 5-1: Imaginary part of the impedance under different F_L's

5.2 The high frequency problem

The volume based impedance extraction formulations have numerical difficulty in handling skin effect. The skin effect drives the current to the surface of the conductor at high frequencies. One dimensional analysis [3] shows that the current damps exponentially from the surface of the conductor to the volume. To make things worse, the damping is more severe at higher frequency. Figure 5-5 shows qualitatively the curves of the damping at two different frequencies, f and $10f$. The damping function used is $e^{-\sqrt{\frac{\mu\sigma\omega}{2}}r}$, where r is the depth from the surface.

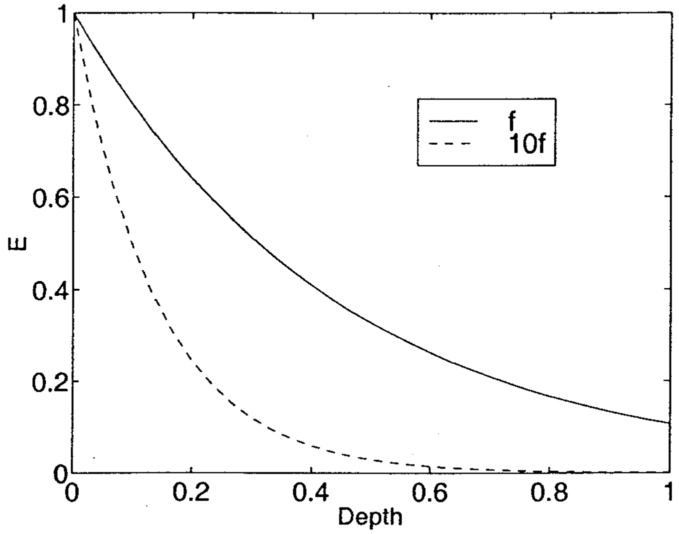

FIGURE 5-5: The skin effect at two frequencies

For general 3-D cases, equation (3.15) provides a mathematical description of skin effect:

$$\bar{E}(x) = \int_S G_1(x,y)\frac{\partial \bar{E}(y)}{\partial n_y}dy - \int_S \frac{\partial G_1(x,y)}{\partial n_y}\bar{E}(y)dy$$

where

$$G_1(x,y) = \frac{e^{iK_1|x-y|}}{4\pi|x-y|}$$

$$K_1 = \sqrt{\frac{\omega\mu\sigma}{2}}(-1+i)$$

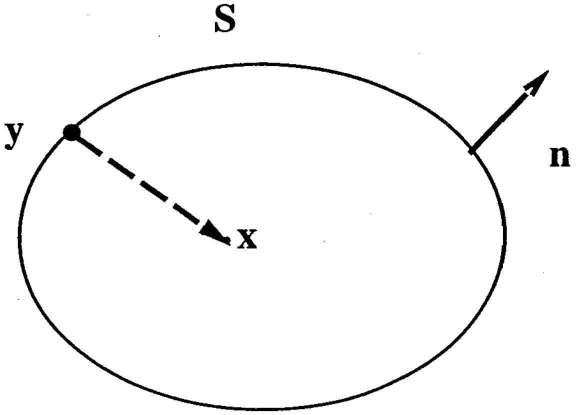

FIGURE 5-6: The skin effect for a conductor of general geometry

With this equation, the electrical field at any point x inside the volume is related to the electrical field and the normal derivative of electrical field on the surface(Figure 5-6). At a high frequency, $\frac{e^{iK_1|x-y|}}{4\pi|x-y|}$ describes the damping as x moves into the depth of the volume while y is on the surface. Near the surface, the damping of the magnitude is approximately $e^{-\sqrt{\frac{\mu\sigma\omega}{2}}r}$.

To reflect the skin effect, a very fine discretization should be used along the depth of the conductors, or the cross section of the conductor needs very fine discretization as shown in Figure 5-7.

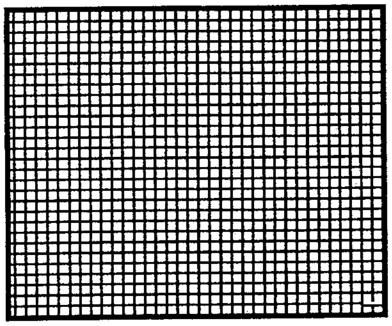

FIGURE 5-7: The discretization of the cross section to capture skin effect

Because the contact is actually a cross section, the surface formulation will have the same discretization problem at high frequency if the input current is computed by summing the current at the contact. However, a method similar to that of [31] can be used to avoid this.

Instead of summing the current at the contact surface C_+, the current at the cross section S_c nearby the contact can be computed (Figure 5-8). S_c is encircled by the directional loop of L. Note that S_c has the normal direction along the current flow direction, which is opposite to the normal direction of C_+.

Start from Faraday's Law and Ampere's Law

$$\begin{aligned} \nabla \times \bar{E} &= -i\omega\mu\bar{H} \\ \nabla \times \bar{H} &= i\omega\epsilon\bar{E} + \bar{J} \end{aligned}$$

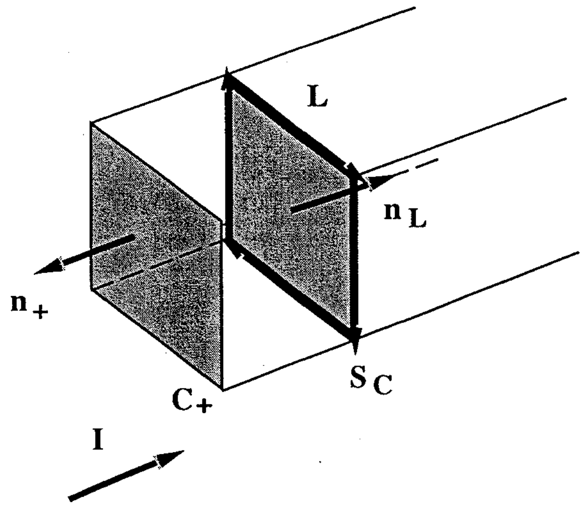

FIGURE 5-8: An equivalent way of high frequency current computation

The current is

$$\begin{aligned} I &= -\int_{C_+} \sigma(\bar{E}\cdot n)ds \\ &= \int_{S_c} \sigma(\bar{E}\cdot n)ds \\ &= \frac{\sigma}{\sigma + i\omega\epsilon}\int_{S_c}(\nabla\times\bar{H})\cdot nds \end{aligned}$$

With Stoke's Theorem, the derivation can be proceeded as:

$$\begin{aligned} I &= \frac{\sigma}{\sigma + i\omega\epsilon}\int_{L}\bar{H}\cdot t_l dl \\ &= \frac{\sigma}{\sigma + i\omega\epsilon}\int_{L}\frac{-1}{i\omega\mu}(\nabla\times\bar{E})\cdot t_l dl \\ &= \frac{\sigma}{\sigma + i\omega\epsilon}\frac{-1}{i\omega\mu}\int_{L}(\nabla\times\bar{E})\cdot t_l dl \end{aligned}$$

where t_l is the unit vector along loop L.

To represent $\nabla\times\bar{E}$ with the quantities available in the surface formulation, consider a local coordinate system near a point x on L. In Figure 5-9, x is on L, n is the unit normal vector, t_l is the unit vector along L, and $t_f = n \times l$ is a tangential vector in the direction of current flow.

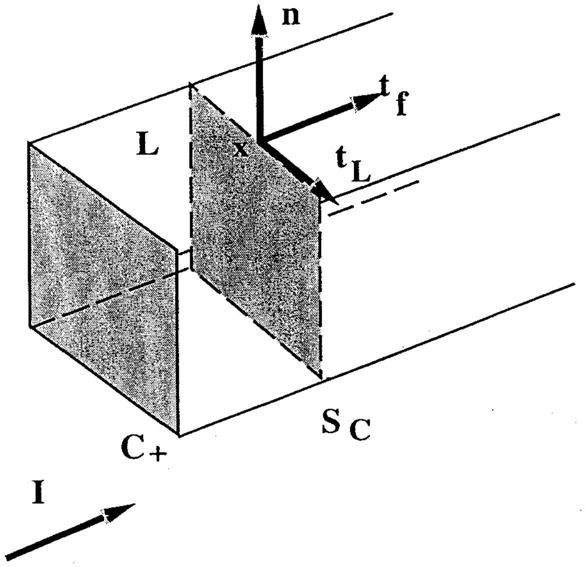

FIGURE 5-9: The local coordinate on the peripheral of the cross section

Because $\nabla \times E$ can be written as

$$\begin{bmatrix} t_l & t_f & n \\ \frac{\partial}{\partial t_l} & \frac{\partial}{\partial t_f} & \frac{\partial}{\partial n} \\ E_{t_l} & E_{t_f} & E_n \end{bmatrix} \tag{5.12}$$

we have

$$(\nabla \times \bar{E}) \cdot t_l = \frac{\partial E_n}{\partial t_f} - \frac{\partial E_{t_f}}{\partial n}$$

Therefore the formula for high frequency current extraction is:

$$I = \frac{\sigma}{\sigma + i\omega\epsilon} \frac{-1}{i\omega\mu} \int_L \left(\frac{\partial E_n}{\partial t_f} - \frac{\partial E_{t_f}}{\partial n}\right) dl \tag{5.13}$$

This formula is applicable for fullwave analysis because no approximation about the field is made.

In the EMQS case, however, the displacement current term in Ampere's Law will be dropped so that the formula becomes:

$$I = \frac{-1}{i\omega\mu} \int_L \left(\frac{\partial E_n}{\partial t_f} - \frac{\partial E_{t_f}}{\partial n}\right) dl \tag{5.14}$$

For the MQS case the formula can be simplified further because $E_n = 0$:

$$I = \frac{1}{i\omega\mu} \int_L \frac{\partial E_{t_f}}{\partial n} dl \tag{5.15}$$

In the discretization, $\frac{\partial E_{t_f}}{\partial n}$ can be computed with

$$\frac{\partial E_{t_f}}{\partial n} = \frac{\partial \bar{E}}{\partial n} \cdot t_f$$

while $\frac{\partial E_n}{\partial t_f}$ can be computed with the finite difference of two nearby panels along the direction of the current t_f on the non-contact surface, as shown in Figure 5-10.

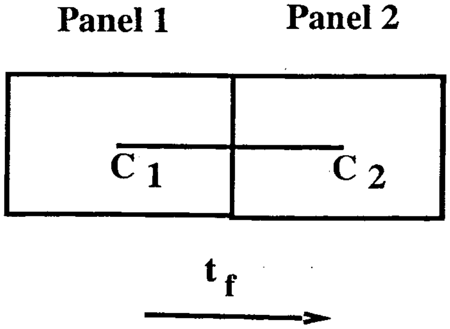

FIGURE 5-10: The finite difference scheme for E_n term

The finite difference formula is:

$$\frac{\partial E_n}{\partial t_f} \approx \frac{E_{n_2} - E_{n_1}}{d_f}$$

where d_f is the distance between the centers of the two panels, C_1 and C_2.

The high frequency method of current computation should be used when the skin effect is strong, or the diameter of the cross section of the conductor is larger than the skin depth. Assume the largest diameter of the cross section is d_H. At the frequency of $\frac{1}{\pi\mu\sigma d_H^2}$, d_H is the same as the skin depth, which is $\delta = \sqrt{\frac{2}{\omega\mu\sigma}}$.

Define F_H as:

$$F_H = \frac{4}{\pi\mu\sigma d_H^2}$$

At the frequencies higher than F_H, the skin effect is quite strong, so that the high frequency method of current computation should be used.

Again, the exact choice of F_H is not critical because the two ways of computing current produce similar results for around one decade of frequency. Still take the wire in Figure 5-4 for example, Table 5-2 shows that similar imaginary part of the impedance is obtained with two ways of current computation even though the discretization is very coarse. In the table, E stands for the ordinary way of computing the current I with the electrical field, while H stands for the method of current computation using the magnetic field.

Method	imag(Z) at 10^{10} Hz	imag(Z) at 10^{11} Hz
E	2.88218e-01	2.73453e+00
H	2.72075e-01	2.66651e+00

Table 5-2: Imaginary part of the impedance from two different methods

With the special treatments of linearizing the kernel at low frequencies and using the magnetic field to compute the current at high frequencies, there are three modes of computation for the surface formulation as summarized in Table 5-3.

Special treatment	$f <= F_L$	$F_L < f <= F_H$	$f > F_H$
Linearization	Yes	No	No
Use H for I	No	No	Yes

Table 5-3: Three modes of computation

6

The panel integration of the Green's function

6.1 Helmhotz kernel

In the linear system of the surface formulation, the panel integration of $\frac{e^{ikR}}{R}$ and $\frac{\partial}{\partial n}\frac{e^{ikR}}{R}$ is necessary. The integration is equivalent to the potential due to a uniformly distributed monopole or dipole over the panel with the Helmhotz kernel $\frac{e^{ikR}}{R}$ (Figure 6-1). In the figure, x is the evaluation point, y is a point on the panel of distance R from x, and n is the normal vector of the panel.

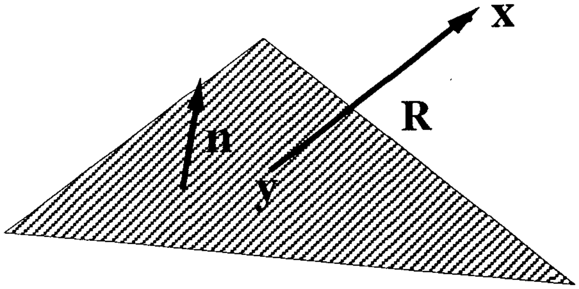

FIGURE 6-1: The potential due to the source over a panel

There is analytic formula to compute the potential due to a uniformly distributed monopole and dipole over a panel with $1/R$ kernel [5, 6], which is a very special Helmhotz kernel with zero as the wave number. Actually, even a dipole distribution over a panel with a linearly varying intensity in respect to the space has been shown to have analytic formula for the potential evaluation [42]. The derivation of all of the analytic formula is based on the desingularization transform eliminating R from the denominator to get a rational relationship between the potential and R. However, the analytic formula for the panel integration of a general Helmhotz kernel seems very unlikely because the relationship between the potential and R is still not rational even after the singularity of R is eliminated. A numerical integration scheme seems to be necessary.

It would be convenient if a numerical scheme were developed to compute the integrations of Helmhotz kernel with an arbitrary wavenumber k, real or imaginary, because in the EMQS case k is K_1 for G_1 but 0 for G_0, and in the fullwave case to be shown in chapter 9, there will be more values of k. Such a numerical scheme would also be useful in the general context of computational electromagnetics, such as scattering and radiation simulation.

Since the potential of the uniform dipole distribution is equivalent to the derivative of the potential due to the monopole distribution with the evaluation point moving along the opposite direction of the normal of the panel(Figure 6-2), it would be enough to develop a numerical scheme to evaluate the monopole potential and its derivative in any direction.

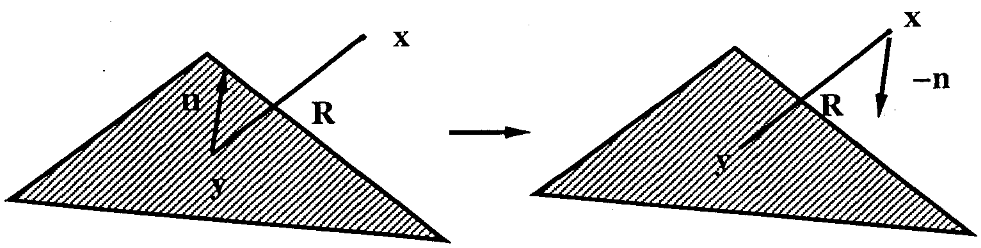

FIGURE 6-2: The conversion from dipole potential to the derivative of monopole potential

In this chapter, a scheme is developed which is applicable to general polygonal panels and general Helmhotz kernels. Through coordinate transformation, the scheme eliminates the singularity in the integration. The 2-D integration is reduced to a 1-D integration by computing the inner integration analytically. For the 1-D integration remained, a Gauss

Quadrature scheme is used. Note that the normal derivative is taken at the evaluation point along the normal direction of the panel in the following text of this chapter.

6.2 The integration by side

The problem can be described as computing the potential ψ at x and the derivative of ψ at x in an arbitrary direction D due to a unit uniformly distributed charge density on a panel(Figure 6-3):

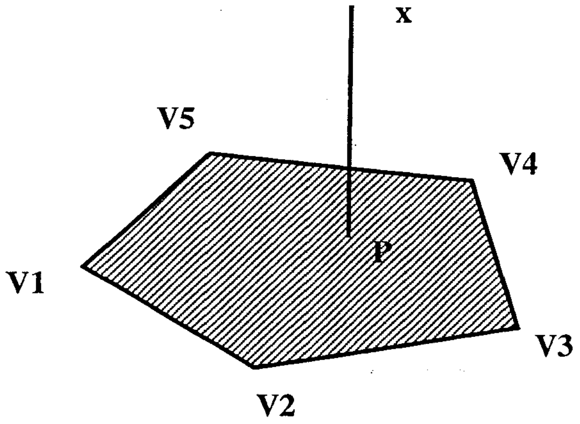

FIGURE 6-3: The integration over a polygon

$$\psi = \int_S \frac{e^{ikR}}{R} ds$$

$$\frac{\partial \psi}{\partial D} = \int_S \frac{\partial}{\partial D} \frac{e^{ikR}}{R} ds$$

Assume the projection point of x onto the plane of the polygonal panel is P, where xP is perpendicular to the panel. As shown in [6], any integration done over the polygon can be computed by adding or subtracting the integration done over the triangles formed by P and the sides of the polygonal. This idea can be shown easily in Figure 6-4

In Figure 6-4, the polygon has all sides labeled in a counter clockwise direction looking from P. The idea of the decomposition of the integration can be explained by computing the area of the polygon, which is the integration with 1 as the integrand. To get the area

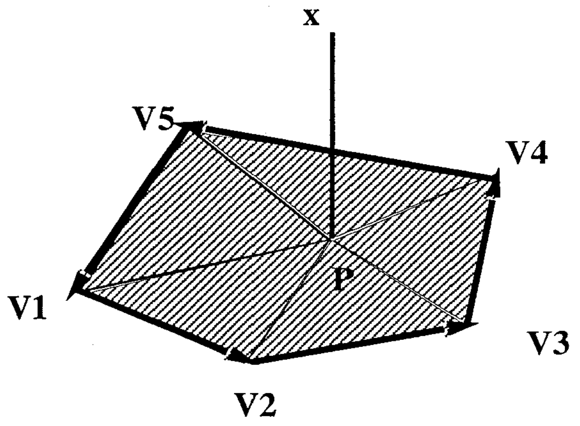

FIGURE 6-4: The decomposed integration over a polygon

of this polygon enclosed by the closed counter clockwise loop, we can also connect the vertices of the polygon to P and compute the area of the triangles like PV_iV_{i+1}. If the side is counter clockwise looking from P, the area of the triangle is added, otherwise it is subtracted. An easy example is the computation of the area of a triangle ABC in Figure 6-5. In this easy example, the area of ABC is the algebraic sum of areas of the triangles formed by P and the sides:

$$S_{ABC} = S_{PBC} + S_{PCA} - S_{PAB}$$

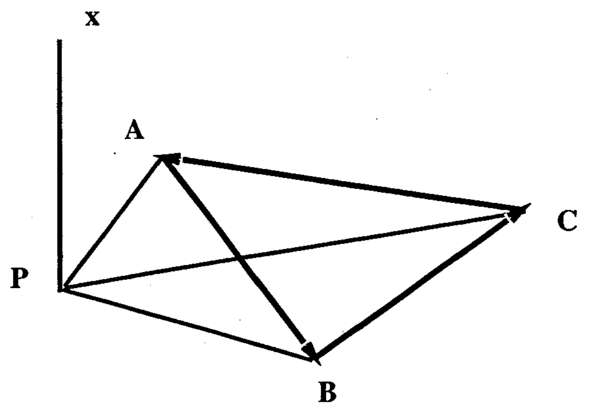

FIGURE 6-5: The decomposed integration over a triangle

Obviously, the same idea can be extended to the integration of a general integrand over a polygon. Let X be a general integrand, then the integration of X over the polygon in Figure 6-3 can be written as:

$$\int_S X ds = \sum_{i=1}^{N} sign(V_i V_{i+1}) \int_{PV_i V_{i+1}} X ds \tag{6.1}$$

where N is the number of vertices, $V_{N+1} = V_1$, and $sign(V_i V_{i+1})$ is 1 if $V_i V_{i+1}$ is counter clockwise looking from P, but -1 otherwise.

With this important equation, the integration for $\frac{\partial \psi}{\partial D}$ and ψ can be done one side at a time. For every side, $sign(V_i V_{i+1})$ should be accounted for in the integration.

6.3 The desingularization transform

Assume AB is a side of the directional polygon, with the direction from A to B. For side AB the integration region is PAB, as shown in Figure 6-6. In the figure, y is a point in the integration region, with a distance of r from P and R from x. h is the distance of xP, or the distance of x to the plane of the polygonal panel.

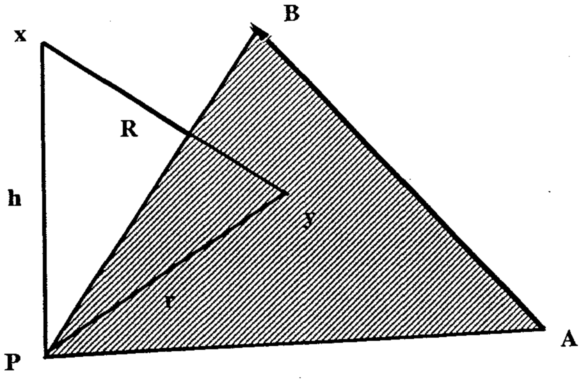

FIGURE 6-6: The one-side integration of a panel

The integration can be written down in polar coordinates as shown in Figure 6-7:

$$\psi(AB) = \int_{\theta_A}^{\theta_B} \int_{r_a(\theta)}^{r_b(\theta)} \frac{e^{ikR}}{R} r dr d\theta$$

$$\frac{\partial \psi(AB)}{\partial D} = \int_{\theta_A}^{\theta_B} \int_{r_a(\theta)}^{r_b(\theta)} \frac{\partial}{\partial D}(\frac{e^{ikR}}{R}) r dr d\theta$$

In Figure 6-7, the origin of the polar coordinate system is P, the axis of θ is perpendicular to AB, and r is the distance of the point on the panel from P.

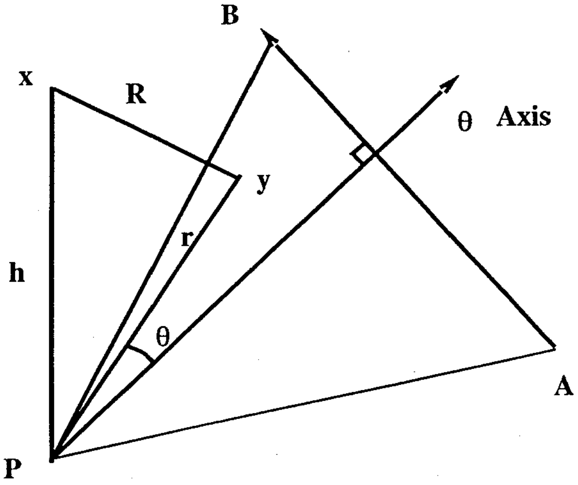

FIGURE 6-7: The one side integration in polar coordinates

Figure 6-8 shows the region of inner integration of r, where a and b denotes the starting and ending points for the inner integration based on r, with θ fixed. Obviously, $a(\theta)$ is always P and $b(\theta)$ is on AB.

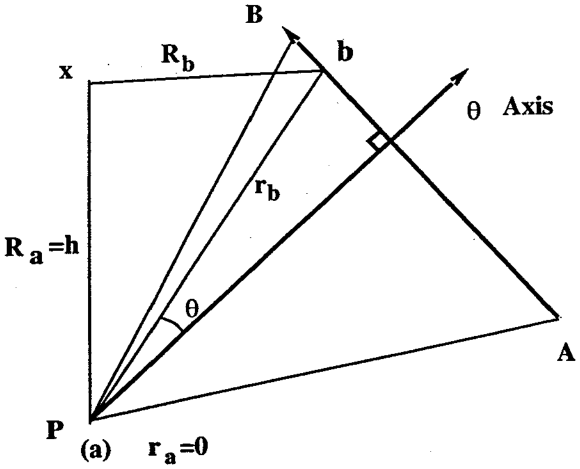

FIGURE 6-8: The inner integration bounds of one side polar integration

With the use of coordinates of R and θ as in [6] and with e^{ik} written as z, the integration can be transformed into:

$$\begin{aligned} \psi(AB) &= \int_{\theta_A}^{\theta_B} \int_{R_a(\theta)}^{R_b(\theta)} z^R dR d\theta \\ \frac{\partial \psi(AB)}{\partial D} &= \int_{\theta_A}^{\theta_B} \int_{R_a(\theta)}^{R_b(\theta)} \frac{\partial}{\partial D} z^R dR d\theta \end{aligned} \tag{6.2}$$

The derivation uses the facts $R = \sqrt{r^2 + h^2}$ and $RdR = rdr$. Note that $R_a(\theta)$ is always h, the distance of x from the plane of the panel.

With the transformation above, the $1/R$ singularity is removed.

6.4 The inner integration

The inner integration in the dimension R can be done analytically.

6.4.1 The inner integration of ψ

Let us solve the problem of ψ first.

Specifically, in the case of $k \neq 0$ (or $z \neq 1$), the inner integration in computing ψ is generally

$$\int_{R_a}^{R_b} z^R dR = \frac{z^{R_b} - z^{R_a}}{ln(z)} = \frac{z^{R_b} - z^{R_a}}{ik} \tag{6.3}$$

while in the case of $k = 0$ (or $z = 1$),

$$\int_{R_a}^{R_b} z^R dR = R_b - R_a \tag{6.4}$$

However, for k with very small norm, $|Z|$ is very close to 1, so that (6.3) is numerically inaccurate.

In this case, a Taylor expansion can provide a better method for computation:

$$\begin{aligned} \int_{R_a}^{R_b} z^R dR &= \frac{z^{R_b} - z^{R_a}}{ln(z)} \\ &= z^{R_a} \frac{z^{R_b - R_a} - 1}{ln(z)} \end{aligned}$$

$$
\begin{aligned}
&= z^{R_a}\frac{e^{(R_b-R_a)ln(z)}-1}{ln(z)} \\
&\approx \frac{z^{R_a}}{ik}\sum_{n=1}^{N}\frac{[ik(R_b-R_a)]^n}{n!}
\end{aligned}
$$

When $|k|$ is very small, a small number of terms in the Taylor series should give an accurate result. Obviously, $k = 0$ is also covered in the small $|k|$ case.

In the practical cases $\bar{R} = R_b - R_a$ can change in a wide range from almost zero to the diameter of a large structure, so that the choice of the computation mode should be based on $|k\bar{R}|$ instead of $|k|$ alone.

Suppose the expansion is always done to order 4 and a precision of about 10^{-15} is wanted, then the criteria and formulae for the inner integration of ψ is:

1. For $|k\bar{R}| < 0.001$,

$$\int_{R_a}^{R_b} z^R dR = \frac{z^{R_a}}{ik}\sum_{n=1}^{4}\frac{[ik(R_b-R_a)]^n}{n!} \tag{6.5}$$

2. For $|k\bar{R}| >= 0.001$,

$$\int_{R_a}^{R_b} z^R dR = \frac{z^{R_b}-z^{R_a}}{ik} \tag{6.6}$$

6.4.2 The inner integration of computing $\frac{\partial\psi}{\partial D}$

The inner integration of computing $\frac{\partial\psi(AB)}{\partial D}$ is based on the result of the inner integration of computing $\psi(AB)$.

For $k \neq 0$, it follows from (6.3):

$$
\begin{aligned}
\int_{R_a}^{R_b}\frac{\partial}{\partial D}(z^R)dR &= \frac{\partial}{\partial D}(\frac{z^{R_b}-z^{R_a}}{ik}) \\
&= z^{R_b}\frac{\partial R_b}{\partial D} - z^{R_a}\frac{\partial R_a}{\partial D}
\end{aligned} \tag{6.7}
$$

while for $k = 0$ (or $z = 1$), it follows from (6.4):

$$
\begin{aligned}
\int_{R_a}^{R_b}\frac{\partial}{\partial D}z^R dR &= \frac{\partial}{\partial D}(R_b - R_a) \\
&= \frac{\partial R_b}{\partial D} - \frac{\partial R_a}{\partial D}
\end{aligned}
$$

Therefore, one formula applies to all cases of k:

$$\int_{R_a}^{R_b} \frac{\partial}{\partial D} z^R dR = z^{R_b} \frac{\partial R_b}{\partial D} - z^{R_a} \frac{\partial R_a}{\partial D} \tag{6.8}$$

In the formula above, the unresolved terms are $\frac{\partial R_b}{\partial D}$ and $\frac{\partial R_a}{\partial D}$. The derivative of R in arbitrary directions is a linear combination of the derivatives in the directions denoted by the unit vectors n, t_1 and t_2 shown in Figure 6-9, where n is the normal direction of the polygon, $t_1 = AB \times n$ is perpendicular to AB while t_2 is parallel to AB. Actually, t_1 is in the same direction as the θ axis. The derivative along D can be related to the derivative long these three basic directions:

$$\frac{\partial R}{\partial D} = \frac{\partial R}{\partial n}(D \cdot n) + \frac{\partial R}{\partial t_1}(D \cdot t_1) + \frac{\partial R}{\partial t_2}(D \cdot t_2) \tag{6.9}$$

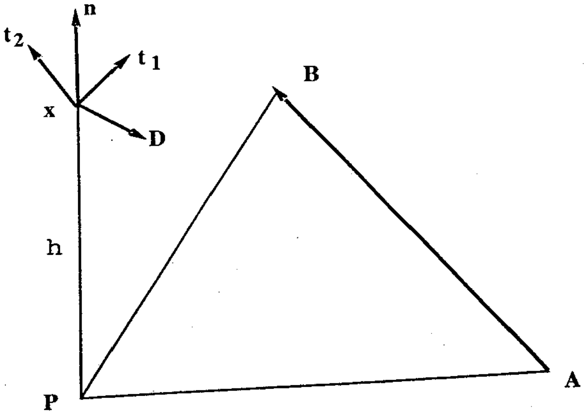

FIGURE 6-9: Three directions of the derivative computation

6.4.2.1 Normal derivative

Consider the normal direction of the derivative first.

With

$$\begin{aligned} R_b &= \sqrt{r_b^2 + h^2} \\ R_a &= h \end{aligned} \tag{6.10}$$

it is obvious that:

$$\frac{\partial R_b}{\partial n} = \frac{h}{R_b}$$
$$\frac{\partial R_a}{\partial n} = p_p \tag{6.11}$$

where p_p is 1 when the evaluation point is on the positive side of the panel, but -1 otherwise.

6.4.2.2 The derivative at tangential direction of t_1

For the tangential direction t, the derivative is computed by perturbing the polygon in the $-t$ direction while holding the evaluation point fixed. Note that the coordinate system based on P is unchanged.

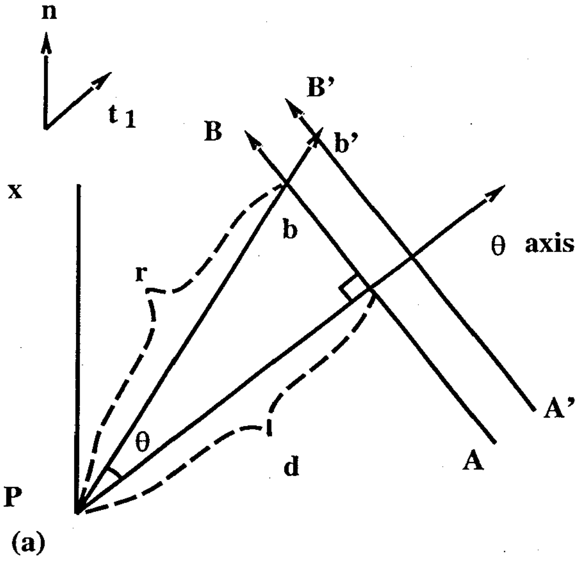

FIGURE 6-10: The perturbation of side AB along t_1

Figure 6-10 shows the method of computing $\frac{\partial R_b}{\partial t_1}$ in which AB is perturbed along t_1. The key is that point b has the same θ coordinate when perturbed, so that $r = d \sec\theta$ is always valid in the perturbation. Based on this fact, the following is true:

$$\begin{aligned}\frac{\partial R_b}{\partial t_1} &= -\frac{\partial R_b}{\partial r}\frac{\partial r}{\partial t_{1_{pan}}} \\ &= \frac{r}{R_b}\sec(\theta) \\ &= \frac{r^2}{R_b d}\end{aligned}$$

Note that $\frac{\partial}{\partial t_{1_{pan}}}$ is used in the first step when the perturbation of the panel is performed.

Because R_a remains to be h for perturbation of the evaluation point in the tangential direction, $\frac{\partial R_a}{\partial t_1} = 0$ must be true.

Therefore, the derivative of R_b and R_a along t_1 is:

$$\begin{aligned}\frac{\partial R_b}{\partial t_1} &= \frac{r^2}{R_b d} \\ \frac{\partial R_a}{\partial t_1} &= 0\end{aligned} \tag{6.12}$$

6.4.2.3 The derivative at tangential direction of t_2

The perturbation of AB along t_2 is shown in Figure 6-11. It is clear in Figure 6-11 that b does not change position in the perturbation, so $\frac{\partial R_b}{\partial t_2}$ must be zero. For the same reason, $\frac{\partial R_a}{\partial t_1}$ is 0.

Therefore, the derivative of R_b and R_a along direction t_2 is:

$$\begin{aligned}\frac{\partial R_b}{\partial t_2} &= 0 \\ \frac{\partial R_a}{\partial t_2} &= 0\end{aligned} \tag{6.13}$$

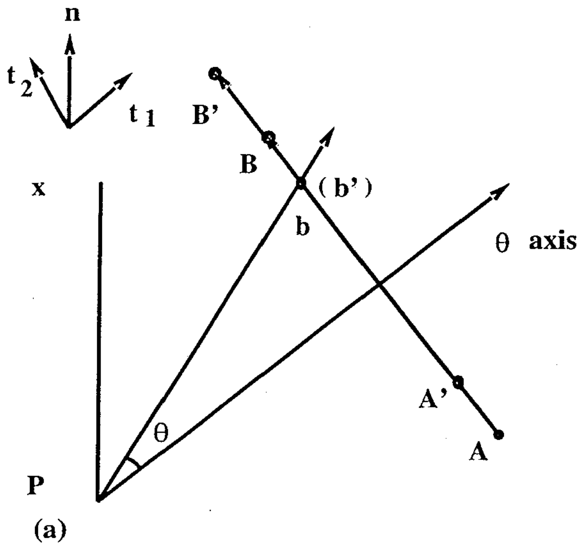

FIGURE 6-11: The perturbation of side AB along t_2

6.5 The outer integration about θ and an improvement

6.5.1 A plain outer integration scheme

With (6.1), the integration for computing ψ and $\frac{\partial\psi}{\partial D}$ are decomposed into the integration over one side at a time. The one-side integration can be written into the 2-D integration form of (6.2). For the inner integration, (6.5) and (6.6) can be used for computing ψ, while (6.8), (6.9), (6.11),(6.12), (6.13) can be used for computing $\frac{\partial\psi}{\partial D}$.

The outer integration of (6.2) about θ, however, needs to be done numerically. With a Gauss Quadrature scheme, the integration formula is:

$$\int_{\theta_A}^{\theta_B} f(\theta)d\theta \approx \sum_{i=1}^{N} w_i f(\theta_i) \tag{6.14}$$

where $f(\theta)$ is the result of the inner integration, N is the Gauss Quadrature order, w_i is the weight and θ_i is the quadrature point within $[\theta_A, \theta_B]$, $i = 1, \ldots, N$.

With (6.14) and the formulae for the inner integration, a numerical scheme to compute ψ and $\frac{\partial\psi}{\partial D}$ is established.

6.5.2 A flaw in the plain outer integration and the solution

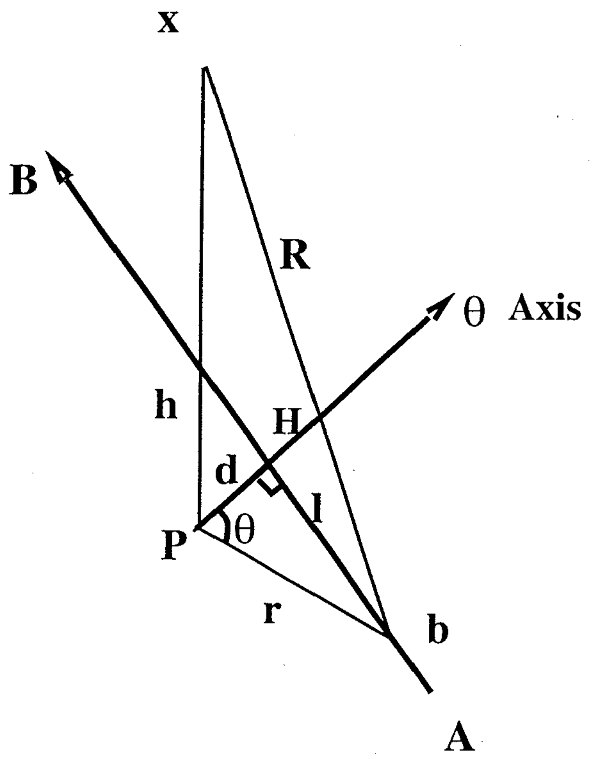

FIGURE 6-12: The flaw in the outer integration

There is a serious flaw in the outer integration scheme with the use of θ as the integration variable. The situation can be shown in Figure 6-12, where H is the intersection of AB and the θ axis, d is the length of PH, l is the length of bH. As shown in Figure 6-12, P is very close to the side AB, which means $r = d\sec\theta$ changes rapidly when θ is close to zero. As a result of $R = \sqrt{r^2 + h^2}$, R changes very rapidly with θ as well. Because the inner integration is done over R, more quadrature points are required around $\theta = 0$. When P is very close to AB, the outer integration will be performed close to a singularity point.

An integration close to a singularity point can cause large numerical errors. For example, the collocation implementation of the second kind of formulation for capacitance extraction has very large numerical error when the conductor has sharp edges because in that case the integration of the close to singular field around the edges is subject to large numerical error. To overcome this problem, qualocation method is introduced which changed the integration to the integration of a smooth function and the accuracy can is greatly improved [41]. The same idea can also be applied to the inductance extraction with permeable materials [43].

Fortunately, a simple transformation for the outer integration can be made by replacing $\int d\theta$ with $\int dl$, or even with $\int dr$ to get away from the singularity problem. In Figure 6-12, it is clear that:

$$\theta = arctg\,\frac{l}{d} = arctg\,\frac{\sqrt{r^2-d^2}}{d}$$

Then we have

$$\begin{aligned} d\theta &= \frac{1}{1+\frac{r^2-d^2}{d^2}}\frac{1}{d}\frac{r}{\sqrt{r^2-d^2}}dr \\ &= \frac{d}{r}\frac{1}{\sqrt{r^2-d^2}}dr \end{aligned}$$

With the relation above, $r = \sqrt{l^2+d^2}$ and $dr = \frac{l}{\sqrt{l^2+d^2}}dl$, the following transform can be made:

$$\begin{aligned} d\theta &= \frac{d}{r}\frac{1}{\sqrt{r^2-d^2}}dr \\ &= \frac{d}{r}\frac{1}{\sqrt{r^2-d^2}}\frac{l}{\sqrt{l^2+d^2}}dl \\ &= \frac{d}{r^2}dl \\ &= \frac{d}{l^2+d^2}dl \end{aligned}$$

The transform can be written as:

$$d\theta = \frac{d}{r}\frac{1}{\sqrt{r^2-d^2}}dr \tag{6.15}$$

and

$$d\theta = \frac{d}{l^2+d^2}dl \tag{6.16}$$

Meanwhile, the inner integration can be done in terms of l or r, with the substitution of:

$$\theta = arctg\,\frac{l}{d}$$

and

$$\theta = arctg\,\frac{\sqrt{r^2 - d^2}}{d}$$

When the outer integration is done with respect to l, the numerical accuracy is very satisfactory. With 23 quadrature points, 10 digits of accuracy is achieved for the Helmhotz kernel with $k = 0$ in the comparison with the analytic result of the potential and field at various different evaluation points due to a uniformly charged panel.

6.6 Linearized kernel

In the low frequency case, linearization is necessary in the computation of the P_1 and D_1 matrices in the linear system of (4.17) or (4.16). The linearization introduces two matrices P_{LM} and D_{LD} to be computed, with the entries defined as:

$$P_{LM}(j,k) = -\frac{k_1^2}{2}\int_{panel_k} |x_j - y| dy$$

$$D_{LD}(j,k) = -\frac{k_1^2}{2}\int_{panel_k} \frac{\partial |x_j - y|}{\partial n_y} dy$$

Then the numerical integration involved can be written down as

$$\begin{aligned}\psi_{LM} &= \int_S R ds \\ \psi_{LD} &= \int_S \frac{\partial R}{\partial n} ds\end{aligned} \tag{6.17}$$

where the derivative is taken at the evaluation point, and n is the normal direction of the panel, as shown in Figure 6-13. The same idea used in the computation of the Helmhotz kernel can be used here to take the derivative at the evaluation point instead of at the source point on the panel.

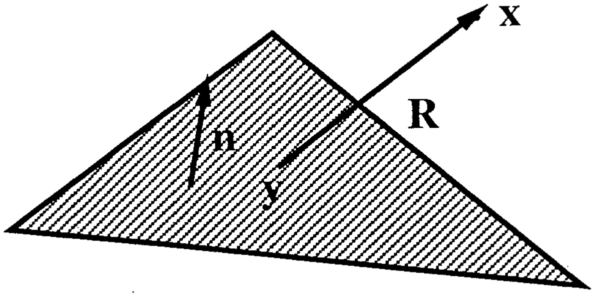

FIGURE 6-13: The basic integration of the linearized kernel

6.6.1 Computing $\int_S R ds$

For the integration to compute ψ_{LM}, (6.1) can be used to reduce the computation to one side at a time, and the integration for side AB can be done in polar coordinates:

$$\psi_{LM}(AB) = \int_{\theta_A}^{\theta_B} \int_{r_a(\theta)}^{r_b(\theta)} R r dr d\theta \tag{6.18}$$

Using the same transform as used for the Helmhotz kernel, the integration can be done in the coordinates of R and θ, and then reduced to a 1-D integration easily:

$$\begin{aligned} \psi_{LM}(AB) &= \int_{\theta_A}^{\theta_B} \int_{R_a(\theta)}^{R_b(\theta)} R^2 dR d\theta \\ &= \int_{\theta_A}^{\theta_B} \frac{((R(\theta))^3 - h^3)}{3} d\theta \end{aligned} \tag{6.19}$$

The relationship between R, r and h is shown in Figure 6-7, and $R = \sqrt{h^2 + r^2}$.

In addition, the transform of (6.16) and Gauss Quadrature scheme can be used to do the integration over l.

6.6.2 Computing $\int_S \frac{\partial R}{\partial n} ds$

The computation of $\int_S \frac{\partial R}{\partial n} ds$ can be done in a easier way, based on the relation between R , r and h.

Because of

$$R = \sqrt{r^2 + h^2}$$

it is clear that

$$\frac{\partial R}{\partial n} = \frac{\partial R}{\partial h}\frac{\partial h}{\partial n} = \frac{h}{R}p_p$$

where p_p indicates if the evaluation point is on the positive or negative side of the panel, namely: p_p is 1 if the evaluation point is on the positive side, and -1 if the opposite is true.

With this fact, the following is true:

$$\int_S \frac{\partial R}{\partial n} ds = p_p h \int_S \frac{1}{R} ds$$

where $\int_S \frac{1}{R}$ can be computed as the potential due to a uniformly distributed monopole of the Helmhotz kernel with $k = 0$.

7

Preconditioned iterative solver

7.1 GMRES, an iterative solution method

The linear systems of (4.17) and (4.16) are very large. For a discretization of M panels, the number of unknowns is approximately $7M$ and $8M$ for (4.17) and (4.16), respectively. If a direct solution method like Gaussian elimination is used, $O(N^2)$ memory and $O(N^3)$ CPU time are necessary.

If a iterative solution method like GMRES is used, the memory required will be still $O(N^2)$ but the cputime can be reduced to $O(N^2)$.

For a linear system of

$$Ax = b$$

The GMRES iterative method can be summarized as:

1. Guess x
2. Calculate residual $r = Ax - b$
3. Update x to reduce r
4. Repeat till $||r||$ small

The iterative method can be applied to (4.17) and (4.16). However, it would be deceiving to state that the CPU time can be reduced to $O(N^2)$ without knowing the number of iterations required for solution.

In GMRES solution, the computation complexity is approximately the number of iterations times the computation complexity of every iteration, which is $O(N^2)$. If the number of iterations in the solution is the same order as N, then the total computational complexity is still $O(N^3)$. For $O(N^2)$ performance in cputime, it is necessary to have the iteration number much smaller than the number of unknowns.

The GMRES iteration number, however, is related to the condition number and eigen value distribution of A. If A has a small condition number, the iteration number tends to be small. If the eigen values of A are clustered, the iteration number also tends to be small. On the other hand, if A has a large condition number and wide spread eigen values, the iteration number can be very large. In the extreme case, it can be as large as N.

7.2 Iteration number and preconditioning

7.2.1 GMRES iteration number of the surface formulation

Unfortunately, the iteration number of the matrix generated by the surface formulation is very large even for a small problem. Take the MQS analysis of the 216 panel discretization of a wire of aspect ratio of 6 for example(Figure 7-1). As shown in Table 7-1, even though the number of unknowns is $N = 1562$, the iteration number is more than 700 for both the low frequency of 1000 Hz and the high frequency of 10^{17} HZ. The iteration number is not neglegible compared with N, and this does not justify the $O(N^2)$ performance in CPU time.

Problem	panel	unknown	iter
LF(10^3 Hz)	216	1562	874
HF(10^{17} Hz)	216	1562	784

Table 7-1: Iteration number of the wire

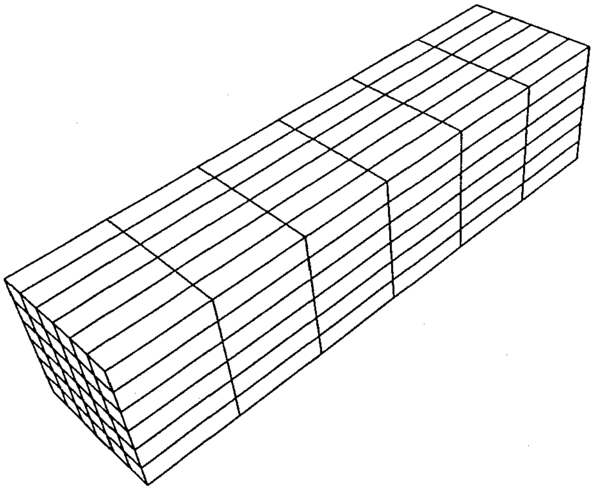

FIGURE 7-1: A wire of 216 panels

7.2.2 The condition number and the scaling problem

To investigate the reason of the large iteration number, the condition number of the matrix for the MQS analysis on the wire example in Figure 7-1 is computed with MATLAB (Table 7-2). From Table 7-2, it is clear that even though the number of unknowns is just $N = 1562$, the condition number of the matrix is about $1.582\,10^4$ at the low frequency of 1000 Hz and about $6.704\,10^{10}$ at the high frequency of 10^{17} Hz.

Problem	panel	unknown	cond	iter
LF(10^3 Hz)	216	1562	$1.582\,10^4$	874
HF(10^{17} Hz)	216	1562	$6.704\,10^{10}$	784

Table 7-2: Condition number and iteration number of the wire

One important fact about the conditioning is that the block matrices of P_0, $D_0 - I$,P_1 and D_1 are much better conditioned than the overall system. For the wire example, the condition number of P_0 and low frequency P_1 are about 69, while P_1 and D_1 at high frequencies have condition number close to one because they are almost diagonal matrices due to the damping kernel. However, the condition number of the linear system is about 16000 for low frequencies, and of order 10^{10} at the high frequency of 10^{17} Hz.

The contrast in the decrease of the condition number of P_1 and D_1 as frequency increases to the increase of the condition number of the overall linear system suggests that there is strong ill-conditioning caused by the difference of the scales between the blocks.

A significant source of the scaling problem is the first set of equations in the linear system, or (4.1)

$$P_1 \frac{\partial \bar{E}}{\partial n} - D_1 \bar{E} = 0$$

At low frequencies, the entries of P_1 are close to those of D_1 if the interaction between the nearby panels is considered; At high frequencies, however, the diagonal entries of P_1 are much smaller than those of D_1, while both of them are almost diagonal matrices. At high frequencies, the diagonal entry of P_1 is approximately $\frac{1}{2ik_1}$ with k_1 of order $\sqrt{f}$, while the diagonal entry of D_1 is always $\frac{1}{2}$ due to the singularity term. This observation agrees with the fact that, for low frequency, $\frac{\partial \bar{E}}{\partial n}$ should be smaller or comparable to $\bar{E}$, while at high frequency, $\frac{\partial \bar{E}}{\partial n}$ should be much larger than $\bar{E}$ due to the skin effect.

The scaling problem can not be solved by scaling the block of P_1 or D_1, because once one of them is scaled, P_0 or $D_0 - I$ has to be scaled as well. This will transfer the scaling problem to (4.5), the other set of equations in the linear system. The scaling problem could be solved by eliminating $\frac{\partial \bar{E}}{\partial n}$ from the overall system using:

$$\frac{\partial \bar{E}}{\partial n} = P_1^{-1} D_1 \bar{E},$$

but this involves a matrix inversion which is $O(N^3)$ effort, so it is not practical either.

Basically, the scaling problem occurs when a equation has a different kind of unknowns with different magnitude. The first set of equations falls into this category, with the problem showing up in the scaling between P_1 and D_1. A similar problem exists for most of the other equations in the linear system. A good preconditioner should capture the scaling information of all the blocks.

7.2.3 The eigen value distribution and the structure problem

Another important observation from Table 7-2 is that the iteration number at the low frequency is even larger than that at the high frequency even though the condition number at the low frequency is smaller. This suggests that there must be a source of the large iteration number other than the condition number. To investigate this problem, the eigen value distribution is plotted for both low frequency and high frequency cases(Figure 7-2 and Figure 7-3). From these figures, it is clear that the eigen values are wide spread at both the low frequency and the high frequency. This is the cause of the large low frquency GMRES iteration number.

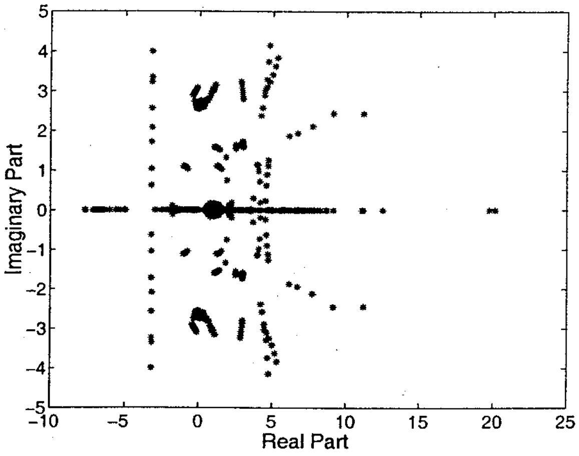

FIGURE 7-2: The eigen values at 1000 Hz

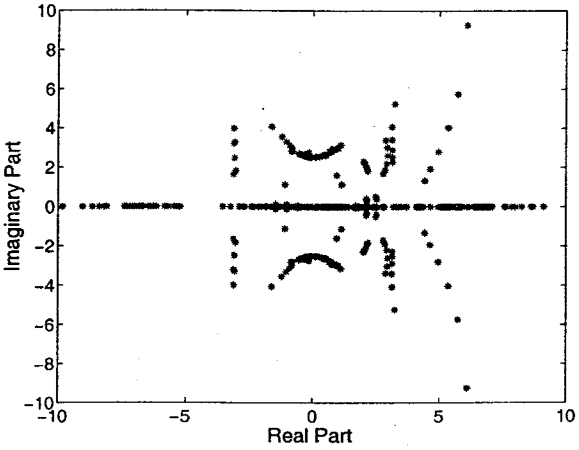

FIGURE 7-3: The eigen values at 10^{17} Hz

The reason of the wide spread eigen values must be related to the fact that the linear system of the surface formulation consists of different kinds of equations an unknowns. As a result, the matrix of the linear system consists of more than 20 block matrices distributed irregularly, and the matrix structure is far from symmetry. Since the eigen values are as spread out at the low frequency as at the high frequency while the scaling problem is much less serious at the low frequency, the ill-structuring of the matrix must be the major source of the wide spread eigen values. A good preconditioner should capture the sturctural information of the matrix.

7.2.4 An effective and efficient preconditioner

A preconditioner is a matrix $\hat{A}$ close to A to make the alternative system $\hat{A}^{-1}Ax = \hat{A}^{-1}b$ much better conditioned than $Ax = b$ because $\hat{A}^{-1}A$ is close to the identity matrix.

To get an effective preconditioner for the linear system of the surface formulation, the features of the matrix related to the iteration number have to be considered. An effective preconditioner should capture these features of the matrix, and the computational cost related to the preconditioner should be small, which includes the forming of the preconditioner and the incomplete factorization.

The basic features of the matrix are:

1. Many equations have different unknowns with different scales, so that the related blocks are not well scaled.

2. It consists of many blocks that form an irregular structure of the matrix. Most of the blocks are sparse except P_0, D_0, P_1 and D_1.

Obviously the sparse block matrices should be kept in the precondtioner so that the scaling information and the structural information of them are well represented. To keep the scaling information of the dense blocks, it would be efficient to replace P_0, D_0, P_1 and D_1 with $\hat{P}_0$, $\hat{D}_0$, $\hat{P}_1$ and $\hat{D}_1$, the diagonal matrices formed by the diagonals of the original ones. The structural information of the dense blocks is also kept because the diagonals reflect the position of the blocks in the whole matrix.

The scaling information of the dense blocks should be well reflected by this method of sparsification. For example, the scaling information of the first set of equations in the linear system

$$P_1 \frac{\partial \bar{E}}{\partial n} - D_1 \bar{E} = 0$$

should be represented by

$$\hat{P}_1 \frac{\partial \bar{E}}{\partial n} - \hat{D}_1 \bar{E} = 0$$

because the diagonal entries are a good representation of the magnitude of all significant entries.

For the same reason, the scaling information of P_0 and $D_0 - I$ in (4.5) can be well kept by replacing them with $\hat{P}_0$ and $\hat{D}_0 - I$.

Therefore, the scheme of forming such a preconditioner $\hat{A}$ can be summarized as:

1. Keep all the sparse blocks.

2. Replace the P_0, D_0, P_1 and D_1 with the matrices of their diagonals, $\hat{P}_0$, $\hat{D}_0$, $\hat{P}_1$ and $\hat{D}_1$.

Such a preconditioner is inexpensive to form because it is very sparse. To minimize the cost of the factorization of the preconditioner, incomplete LU factorization [14] is used and most of the fill-ins are dropped.

After such a preconditioner is used, the iteration number of solving the linear system of MQS analysis for the wire example in Figure 7-1 drops from more than 700 hundred to 21 at the low frequency, and 13 at the high frequency(Table 7-3). The iteration number is smaller at the high frequencies because P_1 and D_1 are almost diagonal, and the scaling difference between these two block matrices is well captured by the preconditioner. The iteration number is much smaller than the number of unknowns, which is 1562. This justifies an $O(N^2)$ performance in CPU time.

In Table 7-3, LF stands for low frequency, HF stands for high frequency, original stands for the original system and preconditioned stands for the preconditioned system.

Problem	LF iter	HF iter	LF cond	HF cond
Original	874	784	1.582e4	6.704e10
Preconditioned	21	13	3.493e4	5.814e5

Table 7-3: The improvement by the preconditioner

Figure 7-4 and Figure 7-5 show the eigen value distributions of the low frequency and the high frequency matrices after the preconditioner is used. The eigen values are almost on the real axis and quite clustered in both cases.

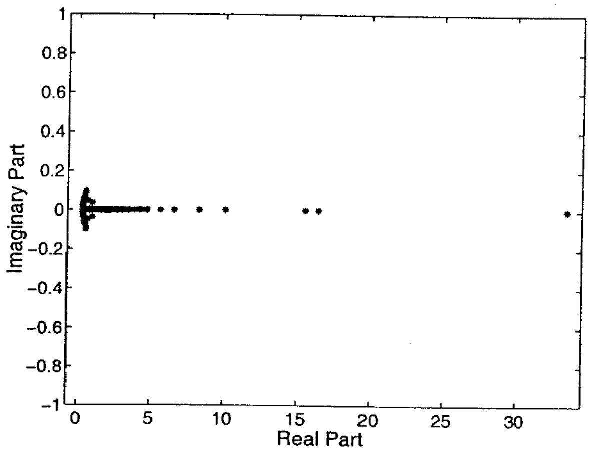

FIGURE 7-4: The eigen values of the preconditioned system at 1000 Hz

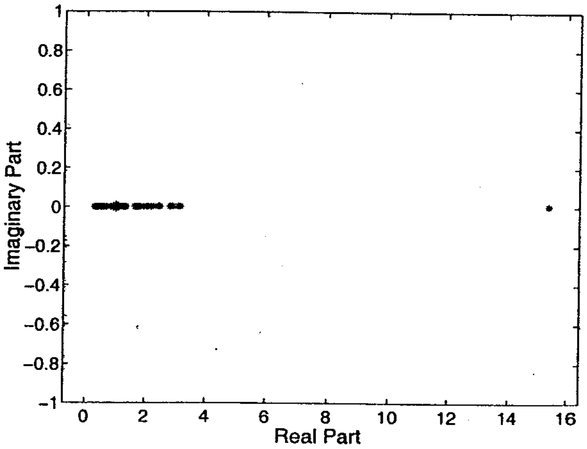

FIGURE 7-5: The eigen values of the preconditioned system at 10^{17} Hz

7.3 Numerical accuracy test of the preconditioned iterative solver

In this section results will be shown from using the above formulation to perform both magnetoquasistatic and electromagnetoquasistatic analysis of several structures. Magnetoquasistatic analysis is performed on a ring, a wire, a multipin connector and a spiral inductor over a semiconductor substrate ground plane, and the results are compared with those from using the public domain program FastHenry [18]. For the ring example, the low frequency inductance extracted with the surface formulation is compared the analytic formula as well. Electromagnetoquasistatic analysis is performed on a transmission line, with the results compared with an analytic formula.

7.3.1 A ring example

A ring example in Figure 7-6 is used for the accuracy test of MQS analysis because the analytic formula of low frequency inductance is available [33]. The ring is $10\mu m$ in diameter, having a square cross section of $0.5\mu m$ by $0.5\mu m$. The conductivity used is close to that of copper. The result of both resistance and inductance is compared with the results from the FastHenry simulation program. FastHenry combines multipole acceleration with a PEEC-like volume method [18].

For the kernel linearization and the current computation method switching of the surface formulation, F_L and F_H are set to be $1.5\,10^6$ Hz and $1.5\,10^{10}$ Hz, respectively.

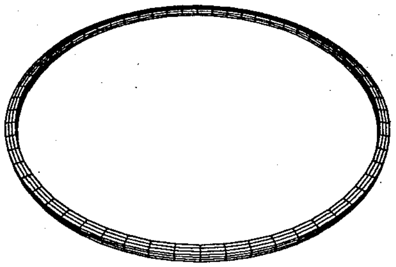

FIGURE 7-6: A discretized ring

As shown in Figure 7-7 , both simulation methods match the analytic inductance for the low frequency range(The low frequency analytic inductance is 0.04889 nH, computed with a formula from [33]), and both show the drop in inductance due to the skin effect at high frequency. However, the convergence of the inductance is more frequency dependent for the surface method than for FastHenry. As can be seen from the curves for 272 panels and 848 panels in Figure 7-7, the convergence is slowest around 10 GHz, when the skin depth is close to the diameter of the cross section.

When examining the resistance, shown in Figure 7-8, the two methods behave very differently. The surface formulation captures the frequency dependence of the resistance, due to the skin effect, without changing the discretization (848 surface panels were used). For FastHenry, however, the resistance stops increasing at a frequency that is discretization dependent. Figure 7-8 shows that the higher frequency resistance computed with FastHenry changes dramatically for 1440, 3840, and 15360 filaments.

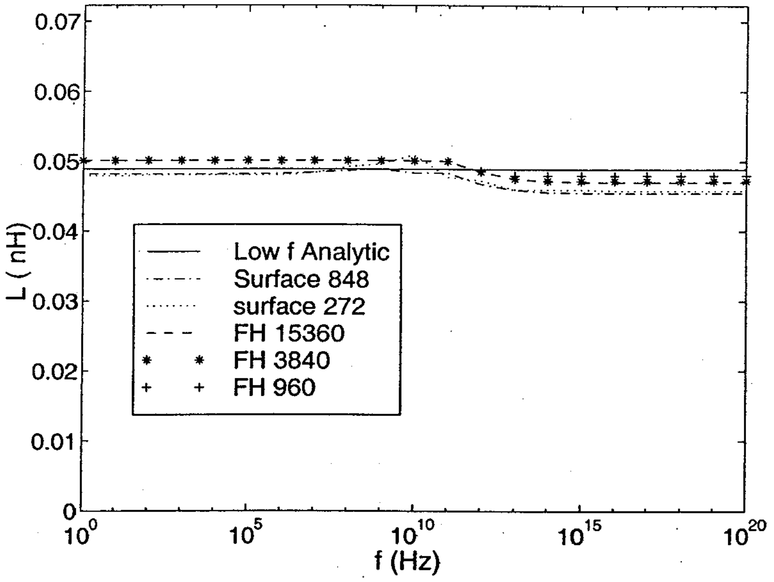

FIGURE 7-7: Inductance for the ring example

7.3.2 A wire example

The significance of a wire example is that such an open loop problem tests whether the surface formulation can capture the partial inductance correctly([23]), or whether the solution of Maxwell's Equation can be done with the surface formulation on part of a

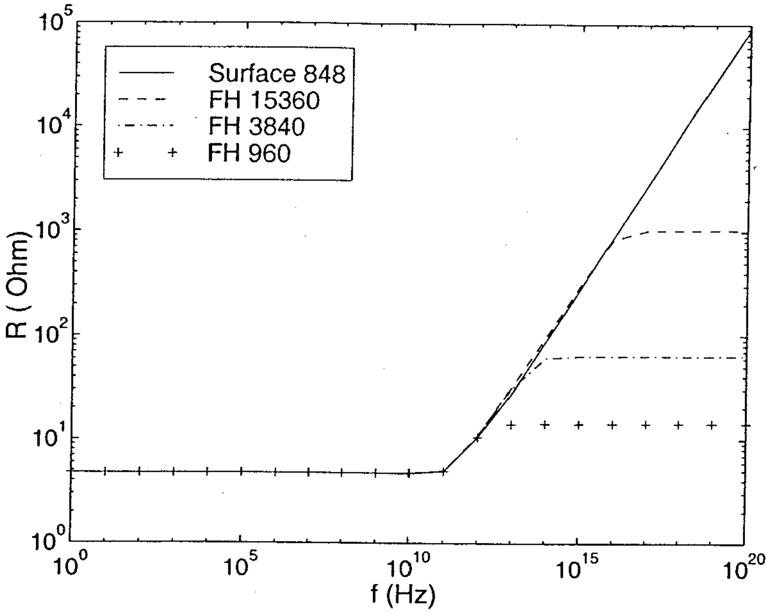

FIGURE 7-8: Resistance for the ring example

closed loop separately, with the influence from the other parts neglected.

F_L and F_H are set to be $1.5\,10^6$ Hz and $1.5\,10^{10}$ Hz respectively for the kernel linearization and the current computation method switching of the surface formulation.

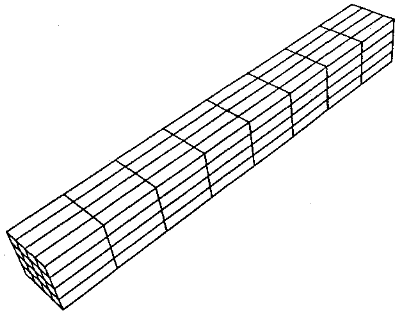

FIGURE 7-9: A wire example

The example used is a straight conductor wire that is 8 μm long, 1 μm wide and 1 μm thick. The same conductivity as for the ring example is used. The surface formulation uses 160 panels over the whole frequency range, while for FastHenry 128, 512 and 2048 filaments are used. The observation is similar to the ring example. As shown in Figure 7-10, two methods show similar inductance over the whole frequency range, and both capture the inductance drop due to the skin effect. For the resistance result as shown in Figure 7-11, the surface formulation still captures the frequency dependency without changing the discretization while the high frequency resistance computed with FastHenry changes dramatically for 128, 512 and 2048 filaments.

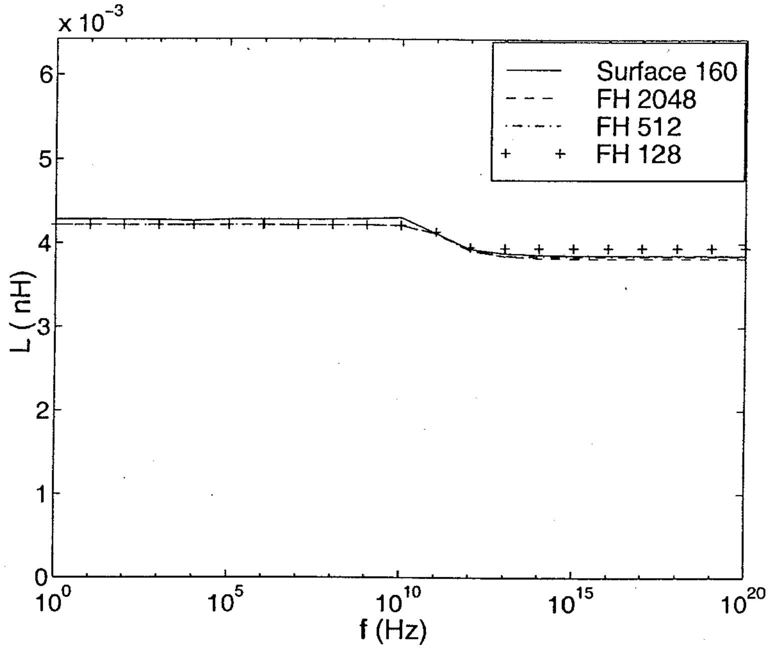

FIGURE 7-10: Inductance for the wire example

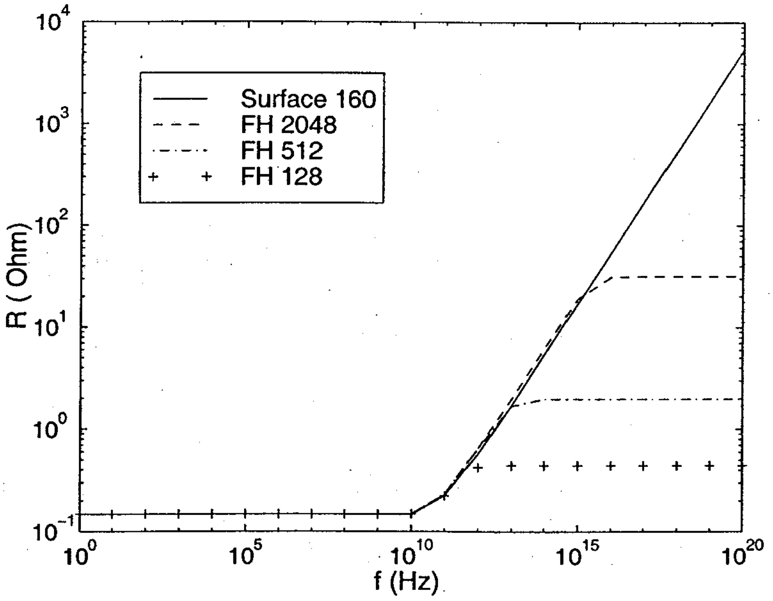

FIGURE 7-11: Resistance for the wire example

7.3.3 Multipin Connector

The significance of the multipin connector example is that it shows the performance of MQS analysis with the surface formulation in the multiple conductor case. This example also shows that the high frequency anomalies of FastHenry with curved structures are not present with the surface formulation.

For the kernel linearization and the current computation method switching of the surface formulation, F_L and F_H are set to be $1.5\,10^6$ Hz and $1.5\,10^{10}$ Hz, respectively.

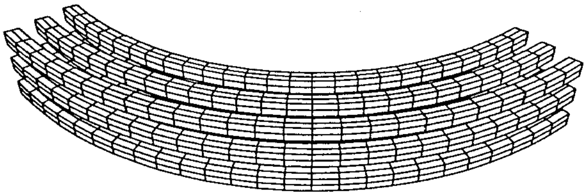

FIGURE 7-12: A 3 by 3 curved connector example

The frequency-dependent magnetoquasistatic inductance (Figure 7-13) and resistance (Figure 7-14) of the 3-by-3 curved multipin connector (Figure 7-12) are shown. The plots show three sets of computations, one with the surface formulation using 2088 panels, one using FastHenry (denoted FH) with 3600 filaments, and one using FastHenry with 14400 filaments. As the resistance plots show, the surface formulation captures the correct frequency dependence of the resistance, but the FastHenry results are only accurate to a discretization dependent frequency. From the inductance plot, the surface formulation also captures the decrease of inductance due to the skin effect. There are a few anomalies in the plots generated by FastHenry for the fine discretization due to a well-known problem with FastHenry's filament integrals [19].

7.3.4 Spiral Inductor over a substrate ground plane

Another example for MQS analysis is a spiral inductor with and without a semiconductor substrate ground plane (Figure 7-15). The diameter of the spiral is about $100\mu m$, with a $5\mu m$ by $5\mu m$ cross section. The ground plane is about $400\mu m$ by $400\mu m$, and is $100\mu m$ thick. The conductivity of the spiral is that of copper, and the conductivity of

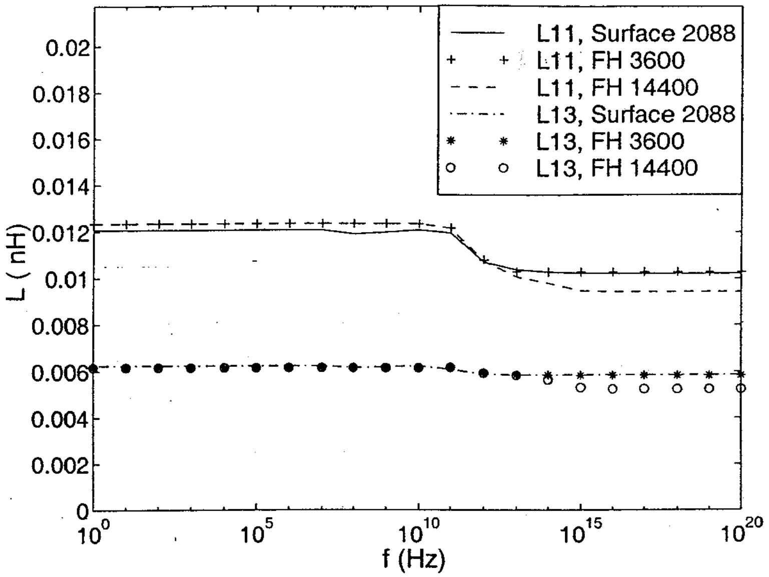

FIGURE 7-13: Inductance for a 3 by 3 curved connector

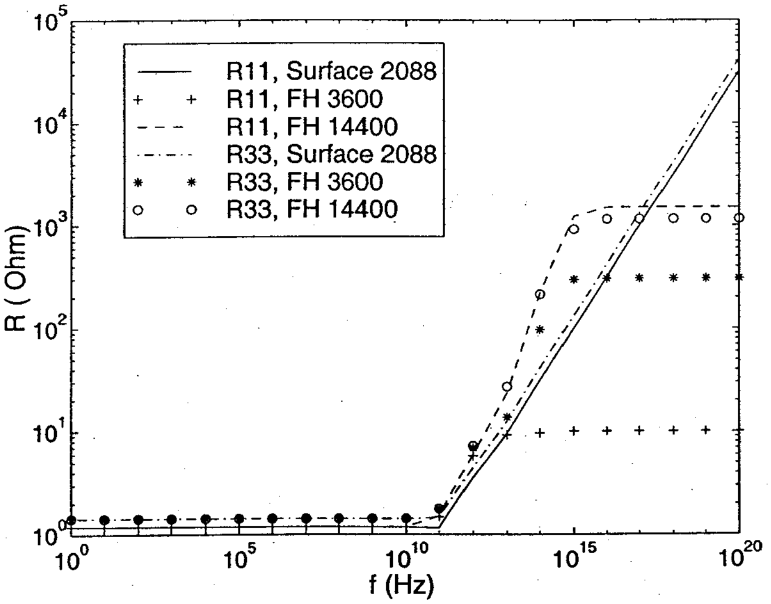

FIGURE 7-14: Resistance for a 3 by 3 curved connector

the ground is .005 that of copper.

The significance of this example is that it shows whether the surface formulation captures the proximity effect due to the existence of the ground plane. In the example, the substrate ground plane is separate from the spiral inductor.

F_L and F_H are set to be $1.5\,10^4$ Hz and $1.5\,10^8$ Hz respectively for the kernel linearization and the current computation method switching of the surface formulation. F_L for the ground plane is not important because the ground plane has negligible impact to the spiral inductor at low frequencies.

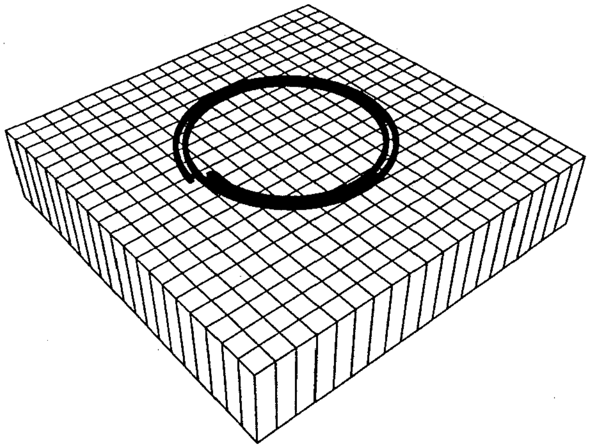

FIGURE 7-15: A spiral inductor over a substrate ground plane

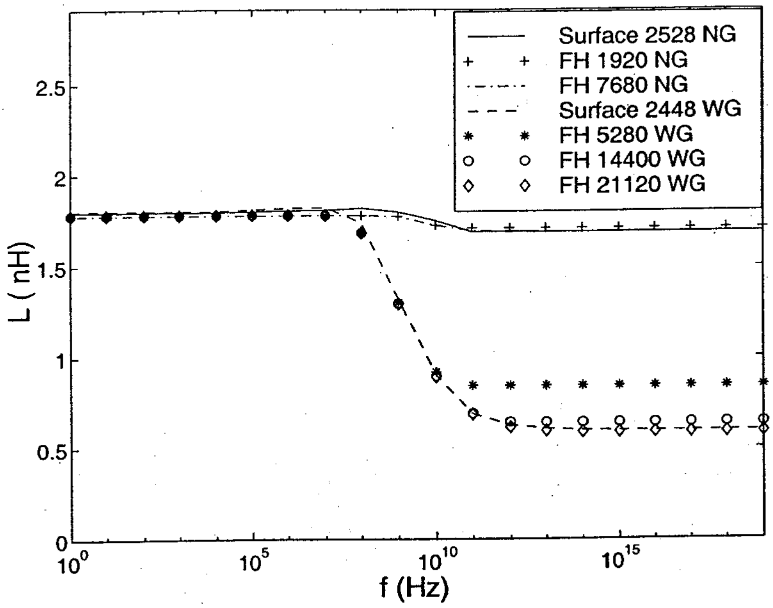

FIGURE 7-16: Inductance for the spiral inductor with and without a substrate ground plane

As shown in Figure 7-16, the surface formulation matches the inductance computed by FastHenry over the entire frequency range. Both methods capture the huge drop of inductance due to the proximity effect. Again, the surface formulation correctly captures

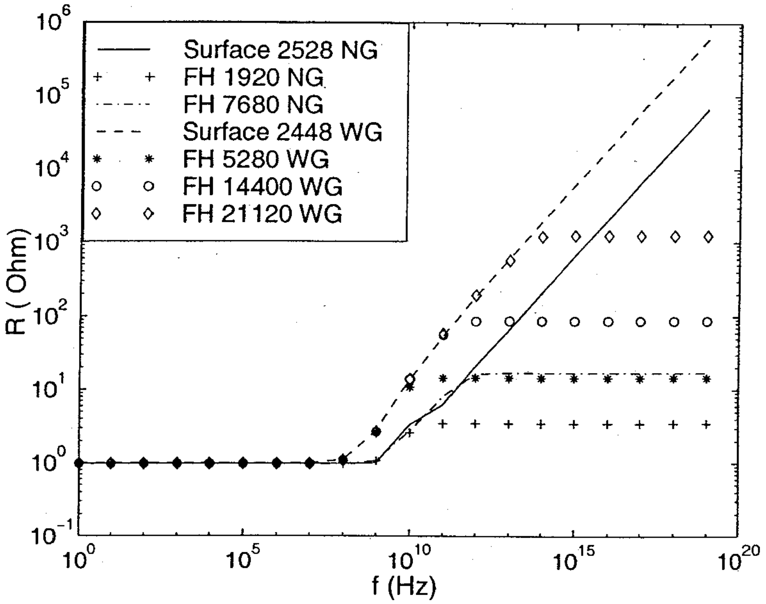

FIGURE 7-17: Resistance for the spiral inductor with and without a substrate ground plane

the frequency-dependent resistance over the entire frequency range, but FastHenry does not, as shown in Figure 7-17. It is worth noting that it is necessary to use more than 21,000 filaments in the substrate ground plane to converge the FastHenry results, where only 2500 panels are needed in the surface formulation.

7.3.5 Transmission Line

To verify that the surface formulation can perform EMQS analysis, the admittance of a long shorted transmission line was computed and then compared to the analytic formula for a nearly 2-D shorted transmission line(Figure 7-18). The transmission line wires are 37 μm wide, 15 μm thick and 10000 μm long. The two lines are separated by a gap of 27 μm. To compute the admittance using the surface formulation, the two wires of the transmission line are discretized into a total of 804 panels. Since the first resonance frequency is 15 GHz, the frequency of the simulations is set to be from 1 GHz to 100 GHz to observe resonance peaks.

For the kernel linearization and the current computation method switching of the surface formulation, F_L and F_H are set to be $1.5\,10^4$ Hz and $1.5\,10^8$ Hz, respectively.

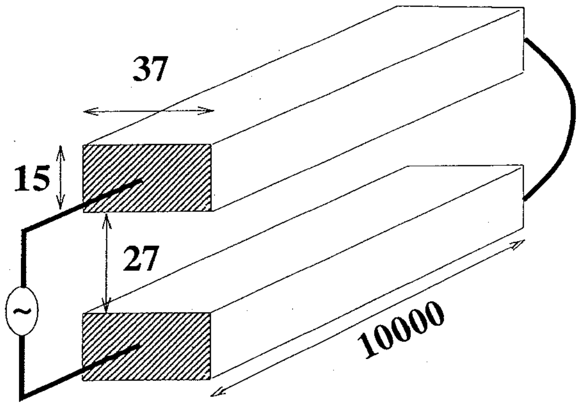

FIGURE 7-18: A long shorted transmission line

To compute the admittance using 2-D analysis, the effective inductance L_0, resistance R_0 and capacitance C_0 per unit length are computed numerically. To get the unit length inductance and resistance, MQS extraction is done at $f_{ref} = 10GHz$ to get the overall inductance L_{ref}, and overall resistance R_{ref}. $L = L_{ref}$ can be used for the frequency of interest because the lowest frequency of interest is high enough to assume current is mostly on the surface($F_H \approx 10^8 Hz$). For the same reason, the resistance in the frequency of our interest is assumed to agree with the asymptotic law of $\sqrt{\omega}$, so that resistance for any frequency f of interest can be computed with $R = R_{ref}\sqrt{f/f_{ref}}$. After L and R is computed, the unit length inductance and resistance are just $L_0 = L/l$ and $R_0 = R/l$, where l is the length of the transmission line. The unit length capacitance is computed with the speed of light c and the unit length inductance by using $C_0 = \epsilon\mu/L_0 = 1/(c^2 L_0)$.

The analytic formula for the impedance Z and the admittance Y is :

$$\beta = \sqrt{\omega^2 L_0 C_0 - i\omega R_0 C_0}$$

$$Z_0 = \frac{R_0 + i\omega L_0}{i\beta}$$

$$Z = Z_0 \frac{1 - e^{2i\beta l}}{1 + e^{2i\beta l}}$$

$$Y = \frac{1}{Z}$$

The results from the surface formulation and analytic formula are compared in Figure

7-19, and clearly show that the surface formulation correctly captures the resonances.

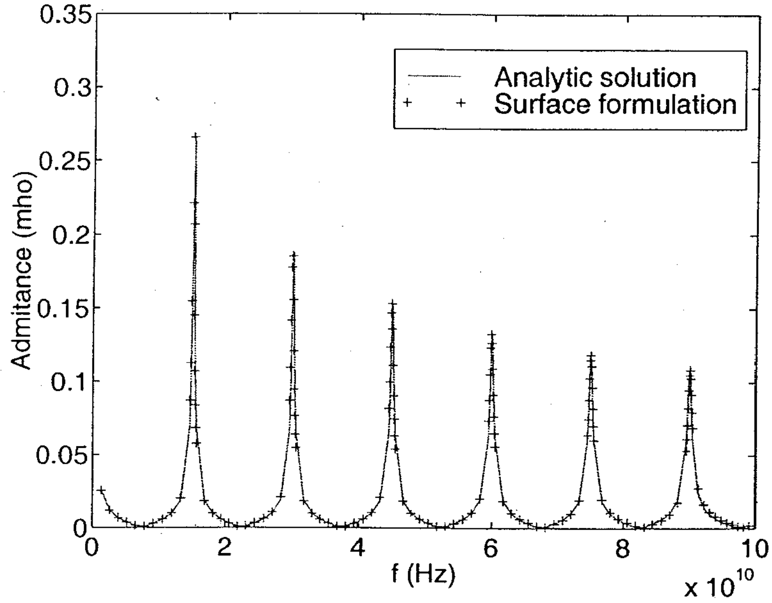

FIGURE 7-19: Admittance of the long transmission line

7.3.6 The iteration number of the large examples

The iteration number of the large examples is shown in Table 7-4. The large examples are the multipin connector, the spiral with or without a ground plane, and the shorted transmission line. In these examples, the number of unknowns are all larger than 5000, but the iterative method always converges in fewer than 100 iterations. The simulation of the transmission line example converges in 4 to 10 iterations because the frequency investigated is in the high frequency range.

Problem	panel	unknown	Min iter	Max iter
MQS connector9	2088	14850	18	42
MQS spiral2 NG	2528	17704	5	67
MQS spiral2 WG	2448	17184	27	81
EMQS transmission	804	6452	4	10

Table 7-4: Size of the problem and GMRES iteration number

8

The Precorrected-FFT acceleration

The preconditioned GMRES method has the performance of $O(N^2)$ both in memory and CPU time. The $O(N^2)$ memory comes from the storage of the matrix, and the $O(N^2)$ CPU time comes from the matrix vector multiplication in every GMRES iteration.

Assume the linear system of (4.17) and (4.16) can be written as

$$Ax = b$$

From the preceding chapter, it is clear that only P_0, D_0, P_1 and D_1 in A are dense blocks, which are basically the discretized form of the monopole and dipole potential operators. This means the only dense part of the matrix vector multiplication can be changed to the potential evaluation problem of Pq as shown in Figure 8-1, where P is the potential coefficient matrix while q is the charge vector.

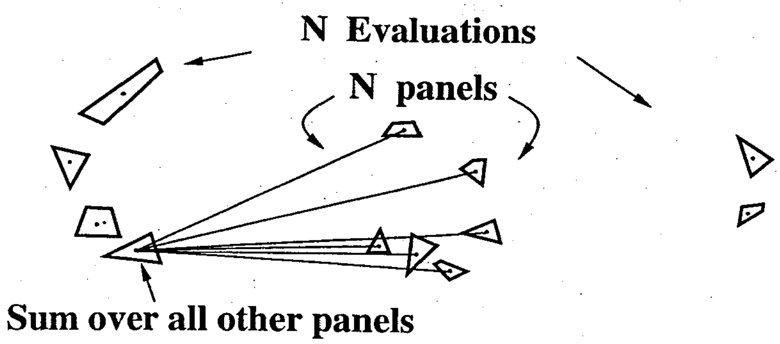

FIGURE 8-1: The potential evaluation problem

In Figure 8-1 (The figure comes from [38]), there are N charged panels and the potential needs to be evaluated at the centers of the N panels. This is an $O(N^2)$ problem. But if a matrix sparsification method like the Precorrected-FFT algorithm [38] is used to reduce the operation to $O(N \log N)$, then the whole formulation would be $O(N \log N)$ in CPU time, because the operations due to the sparse part of A is $O(N)$. At the same time, the memory usage will be reduced to $O(N)$ because the dense blocks are not formed explicitly, and the sparse part of A can be stored with $O(N)$ of memory.

The matrix sparsification techniques can be the Precorrected-FFT algorithm, SVD algorithm or the wavelet based methods. In the thesis, the Precorrected-FFT method is used.

8.1 the Precorrected-FFT method

The Precorrected-FFT method is a fast algorithm for potential evaluation. The basic idea is to separate the potential computation into a far field part and a near field part depending on the distance of an evaluation point from a panel and to represent the panel charge with charges on a 3-D uniform grid for the far field computation.

As shown in Figure 8-2 (borrowed from [38]), the far field contribution of a panel is approximated by projecting the panel charge onto the grid nearby. Then the potential contribution of the panel to the far field evaluation points is represented by the grid potential near the evaluation points due to the projected grid charge.

The far field potential contribution from all panels can be done in parallel by evaluating the potential on all gird points due to the charge projected onto all of them, and the grid potential evaluation process is a 3-D convolution that can be accelerated with the FFT because a 3-D uniform grid is used, and the potential kernel is not direction dependent.

For the near field contribution, direct computation is used.

The Precorrected-FFT method can be summarized into the following steps:

1. Represent panel charges on grid

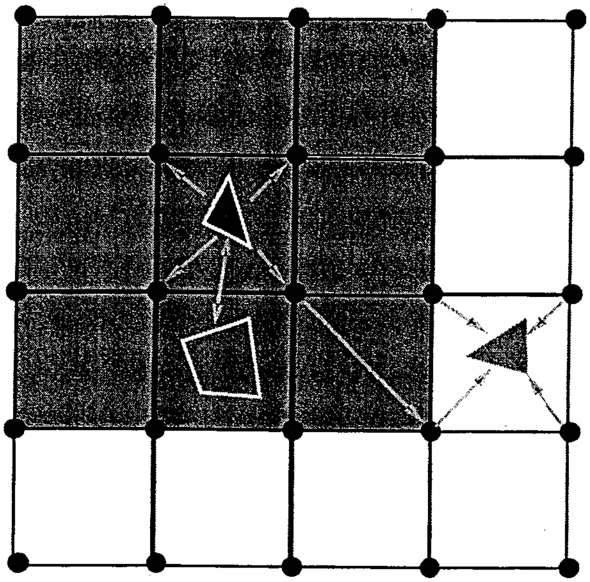

FIGURE 8-2: Precorrected-FFT method

[anterpolation or *projection* step]

2. Calculate grid-charge potentials on grid
3. Interpolate grid potentials onto panels
4. Local corrections

   [compute nearby interactions directly]

The summarization comes from [38].

8.2 Polynomial projection scheme

In combining the Precorrected-FFT algorithm with the iterative solver of the surface formulation, the projection step is crucial. If the collocation projection scheme [38] is used, then the projection coefficients will be dependent on different kernels, while the surface formulation has two different kernels at every frequency, and one of the kernel $G_1(r) = \frac{e^{iK_1 r}}{r}$ changes a lot from a close to $1/r$ kernel at low frequency to an exponentially damping kernel at high frequency. This means the projection needs to be done for every frequency, and this is not efficient.

The polynomial interpolation projection scheme [38], however, generates frequency and kernel independent projection coefficients. The basic idea is to approximate the potential field with polynomial expansion, and the potential at one point can be related to the potential at the nearby grids by some potential coefficients based on the polynomial expansion. The potential coefficients are used as the projection coefficients to project the charge at that point onto the nearby grids. The projection coefficients for a charged panel can be computed by averaging the projection coefficients of the points on the panel.

The only kernel in the surface formulation that has not been previously accelerated with the Precorrected-FFT algorithm is the $\frac{e^{iK_1 r}}{r}$ kernel, where K_1 is imaginary. To show the precorrected-FFT algorithm will have no difficulty with this kernel, a point source is projected onto vertex sources of a 2 by 2 by 2 cube. Then the worst case error at distance 3 from the cube center is plotted as a function of frequency. Even for a low order projection, the error is never worse than a few percent(Figure 8-3). The higher frequency projection is not pursued because in that case the kernel is damping very fast so that only near field evaluation is necessary, which is done with direct method.

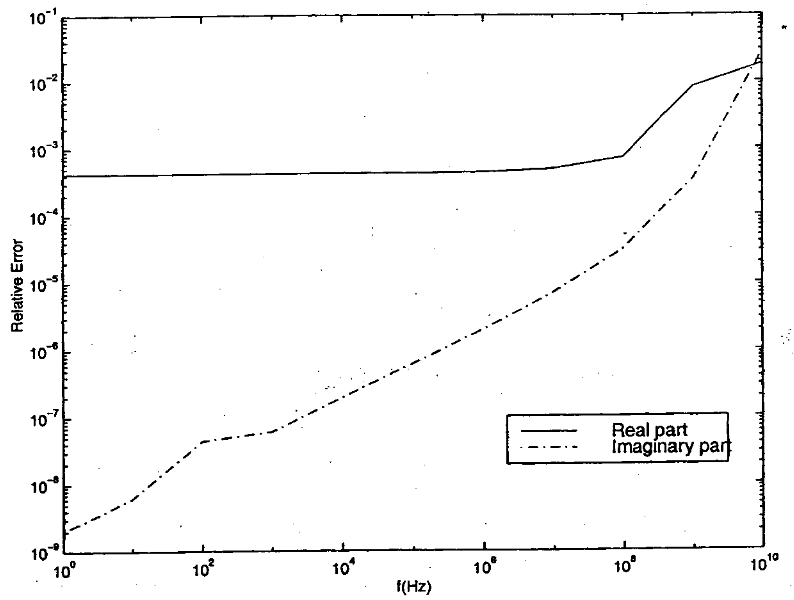

FIGURE 8-3: Worst case projection error for a typical example

8.3 Numerical result of the accelerated formulation

Various numerical examples are used to test the performance of the accelerated formulation. The memory usage and CPU time are measured on a 433 MHz DEC Alpha workstation.

8.3.1 Comparison with FastHenry

A comparison with FastHenry is done for the two turn spiral inductor over a ground plane (Figure 7-15) and the multipin connector (Figure 7-12) in the preceding chapter. The performance is shown in Table 8-1.

Problem	M(FH)	M(SF)	t_{LF} (FH)	t_{LF} (SF)	t_{HF} (FH)	t_{HF} (SF)
MQS connector9	421	129	2381	1364	13719	684
MQS 2-T spiral WG	458	147	2427	738	2822	559

Table 8-1: Comparison with FastHenry

In Table 8-1, M stands for memory in megabytes, t_{LF} and t_{HF} stand for low frequency and high frequency CPU time in seconds, FH stands for FastHenry and SF stands for the surface formulation.

As shown in Table 8-1, FastHenry is significantly slower than the surface formulation for both high frequency and low frequency computations. This shows the disadvantage of a volume method in capturing the frequency dependent resistance and inductance with the same discretization for the whole frequency range. However, FastHenry still could have an advantage in low frequency extraction because a much coarser discretization can be used for FastHenry to capture the inductance and resistance at low frequency.

On the otherhand, the advantage of the surface formulation over FastHenry can be even larger than that shown in Table 8-1 because the surface formulation can achieve acceptable accuracy at high frequency with less panels.

8.3.2 Three typical examples

Simulations are performed on three typical examples of different numbers of panels to show the performance of the accelerated algorithm.

8.3.2.1 A 4 by 4 multipin connector

The first example is a multipin curved connector with 4 by 4 wires (Figure 8-4) discretized into about 4000 panels. Figure 8-5 and Figure 8-6 show the inductance and resistance extracted with the accelerated formulation for MQS analysis. From the graphs, it is clear that the surface formulation captures the drop of inductance due to the skin effect, and the asymptotic increase of resistance at high frequency.

For the kernel linearization and the current computation method switching of the surface formulation, F_L and F_H are set to be $1.5\,10^6$ Hz and $1.5\,10^{10}$ Hz, respectively.

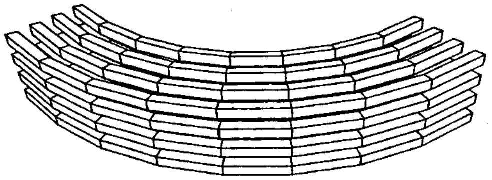

FIGURE 8-4: A 4 by 4 connector

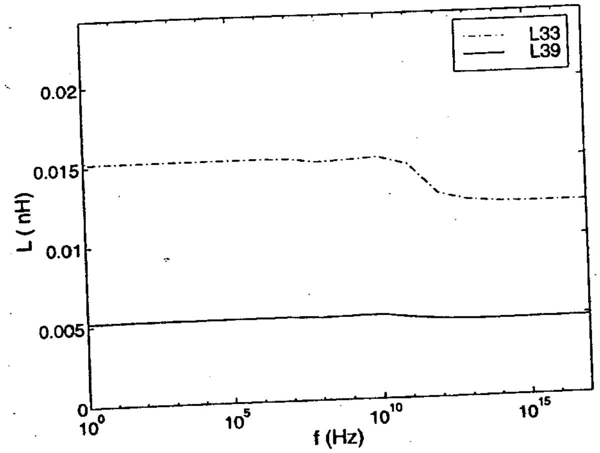

FIGURE 8-5: The inductance of the 4 by 4 connector

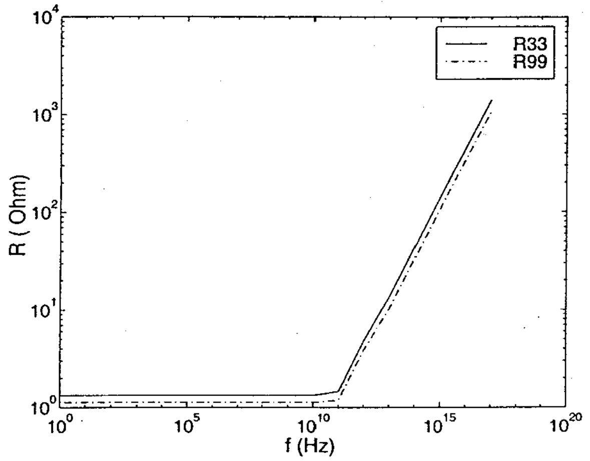

FIGURE 8-6: The resistance of the 4 by 4 connector

8.3.2.2 An 8 turn spiral over a ground plane

The second example is an 8 turn spiral over a thick substrate ground plane (Figure 8-7) discretized into 10118 panels. The diameter of the spiral is about $170\mu m$, with a $5\mu m$ by $5\mu m$ cross section. The ground plane is about $700\mu m$ by $700\mu m$, and is $100\mu m$ thick. The conductivity of the spiral is that of copper, and the conductivity of the ground is .005 that of copper.

For the kernel linearization and the current computation method switching of the surface formulation, F_L and F_H are set to be $1.5\,10^4$ Hz and $1.5\,10^8$ Hz, respectively.

The inductance and resistance computed with the accelerated surface formulation for MQS analysis is shown in Figure 8-8 and Figure 8-9. From these Figures, it is clear that the accelerated surface formulation captures the huge drop of inductance due to the proximity effect and the asymptotic increase of the resistance due to the skin effect at high frequency.

8.3.2.3 The shorted transimission line

EMQS analysis is performed with the accelerated surface formulation on the shorted transmission line used in the preceding chapter. The comparison between the admittance extracted with the surface formulation and that from the analytic formula shown in Figure 8-10 confirms that the accelerated formulation provides accurate answer in EMQS

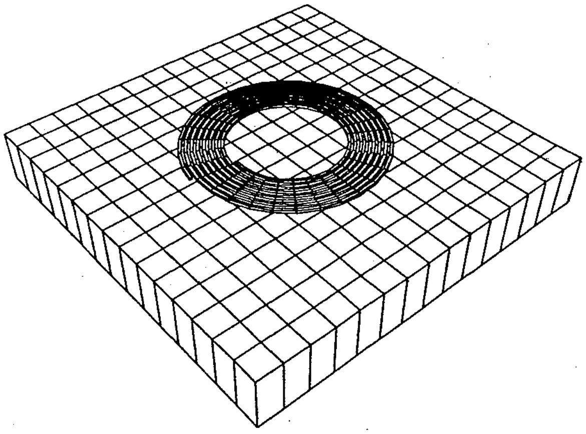

FIGURE 8-7: An 8 turn spiral over a ground plane

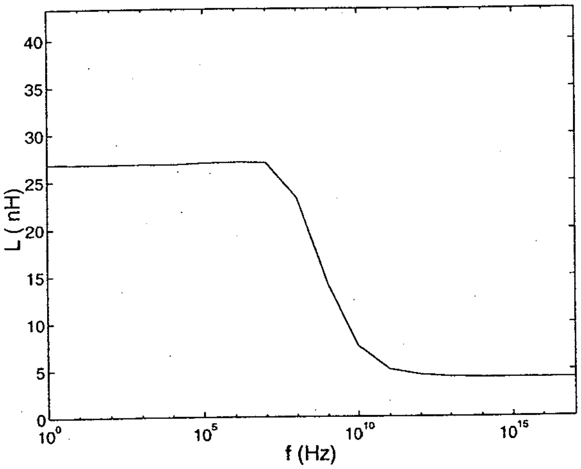

FIGURE 8-8: The inductance of the 8 turn spiral over a ground plane

analysis.

Still, F_L and F_H are set to be $1.5\,10^4$ Hz and $1.5\,10^8$ Hz respectively for the kernel linearization and the current computation method switching of the surface formulation.

8.3.2.4 The memory and CPU time performance

Table 8-2 shows the memory and cputime performance of the surface formulation applied to the three examples. In the table, CPU stands for CPU time and M stands for memory usage.

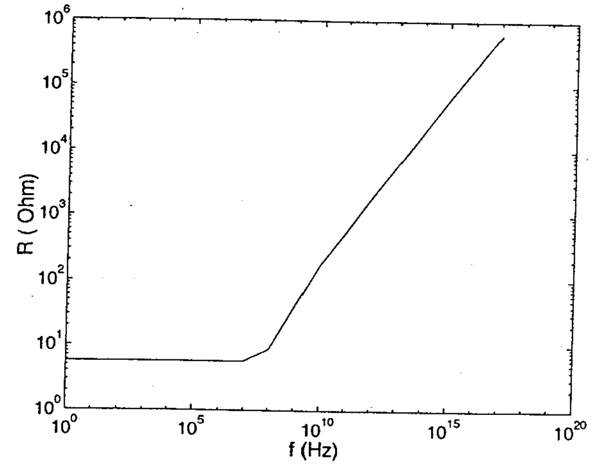

FIGURE 8-9: The resistance of the 8 turn spiral over a ground plane

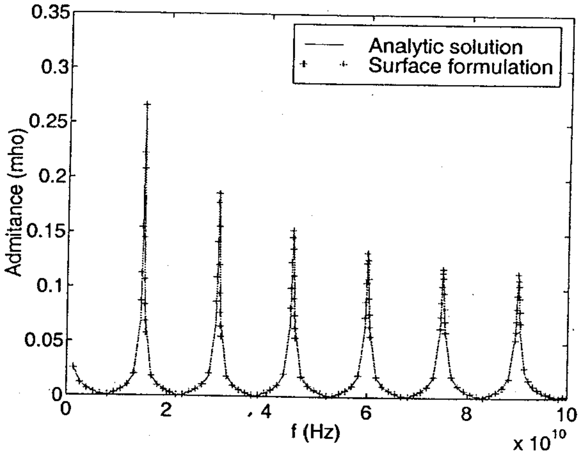

FIGURE 8-10: The admittance of the shorted transmission line

Problem	panel	unknown	M(Mb)	MIN CPU(s)	MAX CPU(s)
MQS connector16	3712	26400	245	2145	4878
MQS spiral8 WG	10118	70874	646	2508	3704
EMQS trans	804	6452	42	41	65

Table 8-2: Performance of the accelerated formulation

8.3.3 Asymptotic performance of the accelerated formulation

Since the Precorrected-FFT algorithm is $O(N \log N)$ in CPU time and $O(N)$ in memory, the Precorrected-FFT accelerated preconditioned GMRES solver for the surface formulation should have similar asymptotic performance.

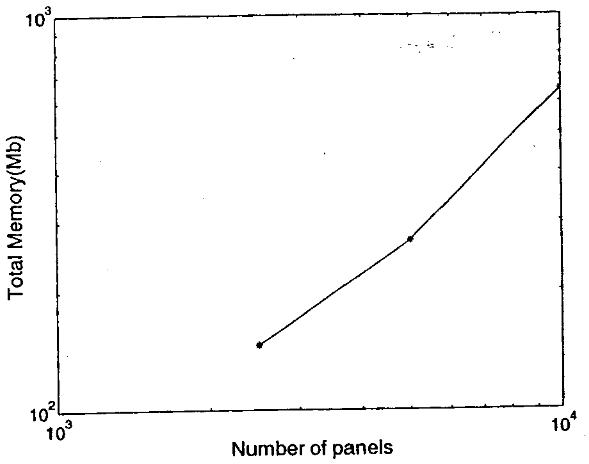

FIGURE 8-11: The memory usage versus the number of panels

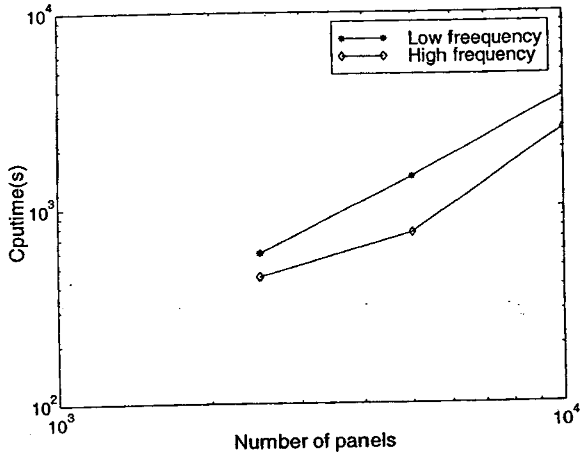

FIGURE 8-12: The cputime versus the number of panels

Figures 8-11 and 8-12 show the performance in CPU time and memory for 2 turn, 4 turn, and 8 turn spirals over a substrate ground plane. The number of panels is around 2500, 5000 and 10000, respectively. For all these three examples, F_L is set to be $1.5\,10^4$ Hz and F_H is set to be $1.5\,10^8$ Hz.

As can be seen from these figures the memory is increasing at close to the same rate as the number of panels, while the CPU time is increasing slightly faster than the number of panels. The reasons that the cputime is increasing slightly faster than $O(N)$ include:

1. The CPU time performance of the Precorrected-FFT algorithm is $O(N \log N)$ but not $O(N)$.

2. The direct computation in the potential evalutation has larger weight in the overall computation as the turns of the inductor increases, because the turns are close to each other.
3. The iteration number increase slightly as the number of panel increases.

The overall performance of the accelerated formulation is close to $O(N)$ in both CPU time and memory.

8.3.4 Comparison of different solution methods

A comparison between three different solution methods for the linear system of the surface formulation is made in Table 8-3 and Table 8-4. The examples for MQS analysis are a two turn spiral inductor without a ground plane(spiral2 NG), the three by three multipin connector(connector9) and the eight turn spiral inductor over the ground plane(spiral8 WG). The EMQS analysis example is the long shorted transmission line(trans). In these tables, Dir stands for the direct solution with Gaussian elimination, Dir GMRES stands for the preconditioned GMRES solution without the Precorrected-FFT acceleration, and FFT GMRES stands for the Precorrected-FFT accelerated preconditioned GMRES solution method.

Table 8-3 is the comparison of the CPU times of the three solution methods, where *h* stands for hours, *m* stands for minutes and *d* stands for days. The low frequency CPU time is used for the iterative methods, which represents the worst case performance. Table 8-4 is the comparison of the memory usage of the three solution methods. From these tables it is clear that the Precorrected-FFT accelerated GMRES solver outperforms the unaccelerated GMRES solver in both memory and CPU time, and both of them outperforms the direct solver of Gaussian elimination by orders of magnitude.

8.3.5 The EMQS analysis of the spiral inductor problem

EMQS analysis is performed on a two turn spiral inductor and an eight turn spiral inductors to observe the coupled inductance-capacitance effect. The two turn spiral has

Problem	panel	unknown	Dir	Dir GMRES	FFT GMRES
EMQS trans	804	6452	3.4h	3m	1m
MQS spiral2 NG	2528	17742	70h	37m	5m
MQS connector9	2322	14850	369h	1h	23m
MQS spiral8 WG	10118	74654	217d	8h	1h

Table 8-3: CPU time of different methods

Problem	panel	unknown	Dir	Dir GMRES	FFT GMRES
EMQS trans	804	6452	1.3Gb	61Mb	42Mb
MQS spiral2 NG	2528	17742	2e4Gb	666Mb	124Mb
MQS connector9	2322	14850	5000Gb	347Mb	129Mb
MQS spiral8 WG	10118	74654	8.9e4Gb	5Gb	646Mb

Table 8-4: Memory usage of different methods

the same dimension as the one in Figure 7-15 and it is discretized into 1568 panels. The eight turn spiral has the same dimension as the one in Figure 8-7 and it is meshed into 5888 panels.

By performing EMQS impedance extraction using the accelerated surface formulation, the first resonance peak of the admittance of the two turn spiral is found to be at around 210 GHz. The admittance curve of the spiral inductor from 1 GHz to 1000 GHz is plotted in Figure 8-13.

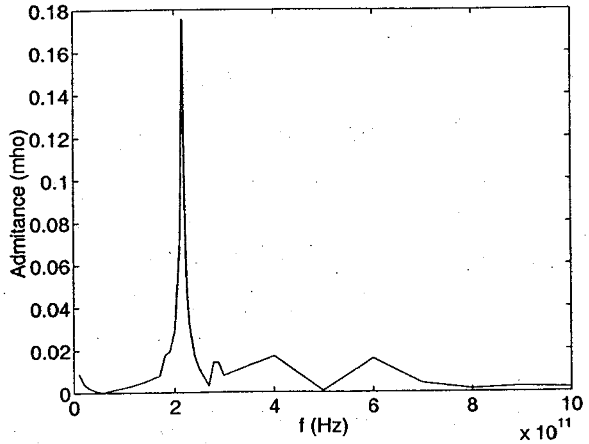

FIGURE 8-13: The admittance resonance peak of the two turn spiral

Even though the first admittance resonance peak is located at around 210 GHz far from the interested frequency range of RF circuits, the effective inductance of the spiral increases sharply in a lower frequency range due to the impedance resonance. As shown in Figure 8-14, the effective inductance of the spiral increases sharply in the 10 GHz range due to the coupled inductance-capacitance effect. The effective inductance is computed with $L_{eff} = \frac{imag(Z)}{i\omega}$, where Z is the EMQS impedance.

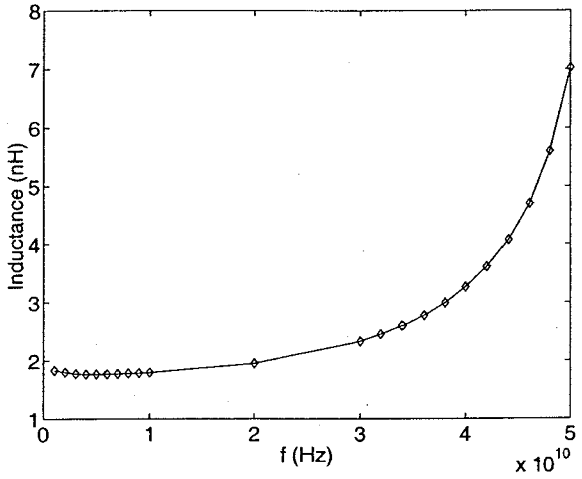

FIGURE 8-14: The effective inductance of the two turn spiral

Finally, EMQS analysis through the accelerated surface formulation shows that the effective inductance of the eight turn spiral inductor increases sharply in the GHz range, as shown in Figure 8-15. In Figure 8-15, the inductance drops a little around 1 GHz due to the skin effect, but it starts increasing around 5 GHz because of the resonance effect. For both examples, F_L is set to be $1.5\,10^4$ Hz and F_H is set to be $1.5\,10^8$ Hz.

8.3.6 The convergence rate of EMQS analysis

The convergence rate of EMQS analysis is estimated for a simple example. A wire of 40 μm long, 10 μm wide and 10 μm thick shown in Figure 8-16 is discretized into 24 panels as shown in Figure 8-17.

When every panel in the 24 panel discretization is broken into 4 identical rectangular panels, a 96 panel discretization is formed. The same procedure carried out twice results

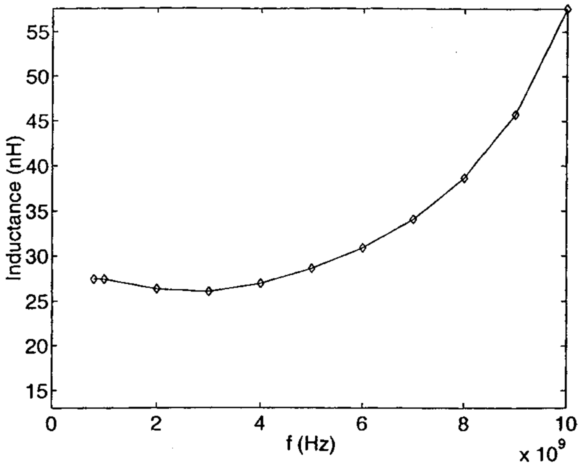

FIGURE 8-15: The effective inductance of the eight turn spiral

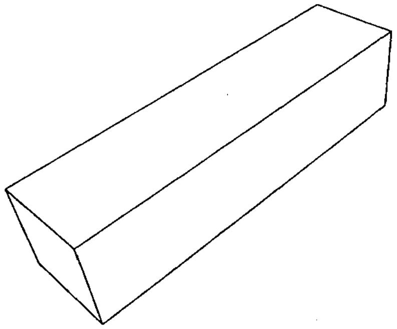

FIGURE 8-16: A wire example

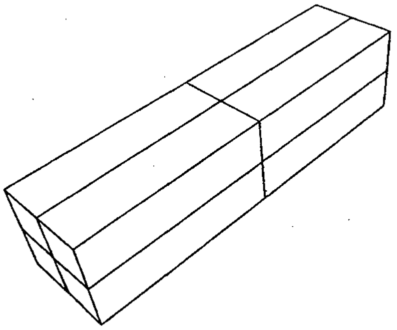

FIGURE 8-17: A wire discretized into 24 panels

in a 384 panel discretization and a 1536 panel discretization. EMQS impedance extraction is performed on the four discretizations at 80 GHz, 100 GHz, and 120 GHz. For every discretization, the average amplitude of the admittance at these three frequencies is computed (Table 8-5). F_H is set to be $1.5\,10^8$ Hz, and F_L is set to be $1.5\,10^4$ Hz.

Denote a_0, a_1, a_2 and a_3 as the average amplitude of the discretizations of 24, 96 ,384,

Number of panels	24	96	384	1536
Average amplitude	0.325608	0.335130	0.338590	0.337742

Table 8-5: The average amplitude of admittance

and 1536 panels, then the error between the discretizations can be computed by

$$e_0 = abs(a_1 - a_0)$$

$$e_1 = abs(a_2 - a_1)$$

$$e_2 = abs(a_3 - a_2)$$

Since the size of the panels decrease by a factor of 2 every time as the discretization is refined, the convergence rate can be evaluated as

$$r = (\frac{\log(e_1/e_0)}{\log(1/2)} + \frac{\log(e_2/e_1)}{\log(1/2)})/2$$

For this example, r is 1.7447, which means that the error decreases at the rate close to that of the panel size.

9

Extension to fullwave impedance extraction

The surface formulation can be extended to fullwave impedance extraction easily. Basically, the EMQS assumption in Ampere's Law is removed. The vector potential and scalar potential take the same integral form as in EMQS analysis, but with the Green's function kernel changed. The same is true for the two surface dyadic integral equations. The surface form of current conservation and the boundary conditions remain the same. At high frequency, the fullwave formula for current extraction should be used, which is very similar to the EMQS formula. At low frequency, the linearization of kernel G_1 is still necessary.

9.1 Fullwave analysis of time harmonic electromagnetics

9.1.1 Time harmonic Maxwell's equations

Time harmonic Maxwell's equations are:

$$\begin{aligned} \nabla \times \bar{E} &= -i\omega\mu\bar{H} \\ \nabla \times \bar{H} &= i\omega\epsilon\bar{E} + \bar{J} \end{aligned}$$

$$\begin{aligned}\nabla\cdot(\epsilon\bar{E}) &= \rho\\ \nabla\cdot(\mu\bar{H}) &= 0\end{aligned}$$

In addition, within the conductor with uniform conductivity, Ohm's Law can be applied:

$$\bar{J}=\sigma\bar{E} \tag{9.1}$$

where σ is the conductivity.

With the same reasoning used in the EMQS analysis of a time harmonic electromagnetic field, it can be proved that:

$$\nabla\cdot\bar{E}=0$$

is true inside and outside the conductor.

With Gauss's Law (3.3) and the uniform ϵ assumption, the charge density ρ is nonzero only on the surface.

9.1.2 Fullwave analysis for time harmonic electromagnetic field

The equivalent representation of Maxwell's equations with vector potential and scalar potential for fullwave analysis is well known [1, 2, 37]. With $\nabla\cdot\bar{A}=-i\omega\epsilon\mu\psi$ (Lorentz gauge), $\mu\bar{H}=\nabla\times\bar{A}$ and $-\nabla\psi=\bar{E}+i\omega\bar{A}$, the differential equations for $\bar{A}$ and ψ turn out to be:

$$\nabla^2\bar{A}-(iK_0)^2\bar{A}=-\mu\bar{J} \tag{9.2}$$

and

$$\nabla^2\psi-(iK_0)^2\psi=-\rho/\epsilon \tag{9.3}$$

where ρ is nonzero only on the surface of the conductors S, and $K_0=\sqrt{\mu\epsilon}\omega$. Therefore, the integral equations for $\bar{A}$ and ψ are:

$$\bar{A}(x) = \int_V G_0(x,y)\mu\bar{J}(y)dy \tag{9.4}$$

and

$$\psi(x) = \int_S G_0(x,y)\frac{\rho(y)}{\epsilon}dy \tag{9.5}$$

where $G_0(x,y) = \frac{e^{iK_0|x-y|}}{4\pi|x-y|}$ and V is the volume of the conductors.

9.2 Two dyadic surface integral equations

9.2.1 The first dyadic surface integral equation

The first dyadic surface integral equation is derived for every conductor separately.

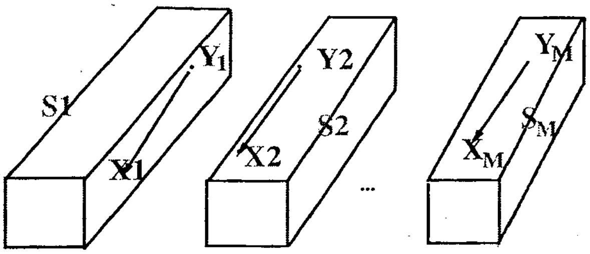

FIGURE 9-1: The illustration of the first dyadic surface integral equation

For the inside of the k-th conductor in Figure 9-1, the electromagnetic field satisfies Faraday's Law (3.1) and Ampere's Law (3.2), which can be written as

$$\nabla \times \bar{E} = -i\omega\mu\bar{H} \tag{9.6}$$

$$\nabla \times \bar{H} = (\sigma_k + i\omega\epsilon)\bar{E} \tag{9.7}$$

with $\bar{J} = \sigma_k\bar{E}$ applied.

Taking the curl on both sides of Faraday's Law (9.6), using the vector identity $\nabla \times (\nabla \times \bar{E}) = \nabla(\nabla \cdot \bar{E}) - \nabla^2\bar{E}$ with $\nabla \cdot \bar{E} = 0$, and also applying (9.7), we have a vector Helmhotz equation about $\bar{E}$ inside the k-th conductor

$$\nabla^2 \bar{E} - (iK_1)^2 \bar{E} = 0 \tag{9.8}$$

which is homogeneous for the conductor and $K_1 = \sqrt{-i\omega\mu\sigma_k + \mu\epsilon\omega^2}$.

Applying Green's Second Identity to (3.14) with $x \in V_k$ as the evaluation point of the Green's function yields a dyadic surface integral equation

$$\int_{S_k} G_1(x,y) \frac{\partial \bar{E}(y)}{\partial n_y} dy - \int_{S_k} \frac{\partial G_1(x,y)}{\partial n_y} \bar{E}(y) dy = \bar{E}(x) \tag{9.9}$$

where S_k and V_k are the surface and the volume of the k-th conductor,

$$G_1(x,y) = \frac{e^{iK_1|x-y|}}{4\pi|x-y|} \tag{9.10}$$

To make all the quantities on the surface, move x to the interior of S_k, then:

$$\int_{S_k} G_1(x,y) \frac{\partial \bar{E}(y)}{\partial n_y} dy - \int_{S_k} \frac{\partial G_1(x,y)}{\partial n_y} \bar{E}(y) dy = \bar{E}(x) \tag{9.11}$$

where $x, y \in S_k$.

Still a simpler notation is used in which $\int_S \frac{\partial G_1(x,y)}{\partial n_y} \bar{E}(y) dy$ is the entire integral rather than a principle-value integral plus an extra term.

9.2.2 The second dyadic surface integral equation

The second dyadic surface integral equation is derived by considering all conductors at the same time, so that the coupling between the different conductors as shown in Figure 9-2 can be accounted for.

Equation (3.14) can be rewritten as another vector Helmhotz equation:

$$\nabla^2 \bar{E} - (iK_0)^2 = i\omega\mu\bar{J} \tag{9.12}$$

which is homogeneous throughout the space.

Applying Green's Second Identity to (9.12) with $x \in V$ as the evaluation point of the

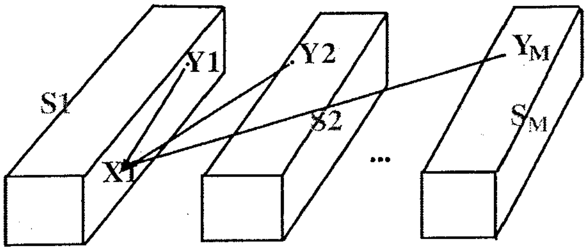

FIGURE 9-2: The illustration of the second dyadic surface integral equation

Green's function yields the following integral equation

$$\int_S G_0(x,y)\frac{\partial \bar{E}(y)}{\partial n_y}dy - \int_S \frac{\partial G_0(x,y)}{\partial n_y}\bar{E}(y)dy = \bar{E}(x) + i\omega \int_V \mu G_0(x,y)\bar{J}(y)dy$$

where $G_0(x,y)$ is the same Green's function in the integral expression of $\bar{A}$ and ψ.

With $-\nabla\psi = \bar{E} + i\omega\bar{A}$ and $\bar{A}(x) = \int_V \mu G_0(x,y)\bar{J}(y)dy$, the integral equation above can be written as:

$$\int_S G_0(x,y)\frac{\partial \bar{E}(y)}{\partial n_y}dy - \int_S \frac{\partial G_0(x,y)}{\partial n_y}\bar{E}(y)dy + \nabla\psi(x) = 0 \tag{9.13}$$

Move x to the interior of S, then we have a dyadic surface integral equation that is based on the electrical field, its normal derivative and the gradient of scalar potential:

$$\int_S G_0(x,y)\frac{\partial \bar{E}(y)}{\partial n_y}dy - \int_S \frac{\partial G_0(x,y)}{\partial n_y}\bar{E}(y)dy + \nabla\psi(x) = 0 \tag{9.14}$$

Again, the singularity in the integration is not removed.

9.3 The current conservation, the capacitive integral equation and boundary conditions

The surface integral form of the current conservation remains the same as that in EMQS impedance extraction, because it is just based on $\nabla \cdot \bar{E} = 0$:

$$\int_C E_t(x) \cdot (n(x) \times l(x))dx - \int_a \frac{\partial E_n(y)}{\partial n(y)} dy = 0 \tag{9.15}$$

The capacitive integral equation takes the same form as that in EMQS impedance extraction

$$\psi(x) = \int_S G_0(x, y) \frac{\rho(y)}{\epsilon} dy \tag{9.16}$$

but G_0 is the fullwave kernel.

The boundary conditions are the same as in EMQS impedance extraction.

9.4 Numerical simulations

9.4.1 Fullwave analysis of the long shorted transmission line

The same discretization for EMQS analysis can be used for fullwave impedance extraction, and the panel integration problem has been solved in Chapter 6. Still, a low frequency linearization is necessary to capture the inductive effect correctly. At high frequency, the fullwave current extraction formula should be used.

The linear system can be solved with the preconditioned GMRES method, and accelerated with the Precorrected-FFT algorithm. The Precorrected-FFT algorithm has no difficulty in the acceleration of Helmhotz kernel with real wavenumber [38].

Fullwave impedance extraction is performed on the long shorted transmission line example (Figure 7-18) in the preceeding chapters, and the result is compared with that from the analytic formula. Figure 9-3 shows that fullwave impedance extraction with the surface formulation yields accurate results. Since EMQS impedance extraction also matches the analytic solution accurately (Figure 7-19), this means EMQS analysis approximates fullwave analysis accurately for this example.

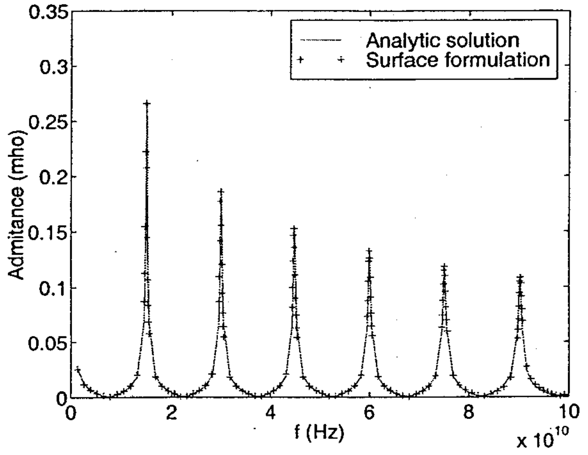

FIGURE 9-3: The fullwave admittance of the shorted transmission line

9.4.2 Limit of EMQS analysis

EMQS analysis can be taken as a good approximation of fullwave analysis when the size of the structure is small compared with the wavelength. In the long shorted transmission line, however , EMQS impedance extraction seems to be accurate even for the case when the size of the structure is three times the wavelength if the sixth admittance resonance peak is considered (Figure 7-19).

To explore if it is a special case or a general result, the gap (d) between the two wires of the transmission line is increased to 500 μm and 5000 μm to see if EMQS analysis still provides similar result as fullwave analysis. The length of the transmission line is 10000 μm, and in the original transmission line example, d is 15 μm.

Figure 9-4 and Figure 9-5 show the difference between EMQS analysis and fullwave analysis when the gap is significant compared with the length of the transmission line. It is clear from these figures that the fullwave analysis still gives almost the same position of the resonance peaks as predicted for the long shorted transmission line with the small gap of 15 μm. The amplitude estimated from fullwave analysis is also decaying as the frequency increases and this agrees with the intuition which is based on the fact that the resistance should increase with frequency.

Several observations from the comparison of EMQS results with fullwave results are worth to note. First of all, the position of the resonance peaks estimated through fullwave

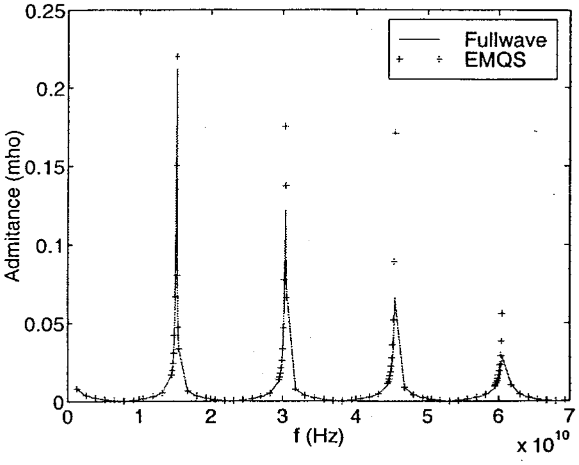

FIGURE 9-4: EMQS and fullwave results for $d = 500$

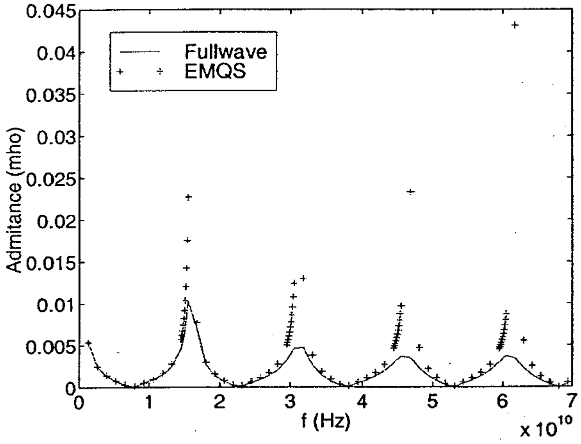

FIGURE 9-5: EMQS and fullwave results for $d = 5000$

analysis is well captured by EMQS analysis. Secondly, the amplitude of the resonance peak computed through EMQS analysis differs a lot from that computed through fullwave analysis. Basically, EMQS analysis often overestimates the amplitude, and the error tends to be larger at higher frequency. The amplitude of resonance peaks can even be increasing significantly with the increase of frequency, and this is against physics intuition. Finally, as the gap between the wires increases, the error of the amplitude estimation through EMQS analysis also gets larger. These observations suggest that fullwave analysis is much more reliable than EMQS analysis when the size of the structure is close to or larger than the wavelength. In other words, it is a special case that EMQS analysis gives very good approximation of fullwave analysis when the structure is comparable to or larger than the wavelength, as has been observed for the long shorted transmission line with very small gap.

10

Conclusions and future work

10.1 Conclusions

In the thesis, a new surface integral formulation and discretization approach for computing electromagnetoquasistatic impedance of general 3-D conductors is developed. To develop the new surface formulation, two dyadic surface integral equations that relate the electrical field to the scalar potential are derived from Maxwell's equations. In addition, the surface integral form of $\nabla \cdot E = 0$ is also derived. All these equations are applicable to general 3-D structures because no assumption of geometry is made.

The key advantages of the formulation is that it avoids volume discretization of the conductors and the substrate, and a single discretization is accurate over the entire frequency range. In addition, the approach does not require a-priori information about proximity effects or the low frequency distribution of the currents.

Computational results from a ring, a wire, an on-chip spiral inductor, a multipin connector and a transmission line verify that the formulation is accurate when the preconditioned GMRES iterative method is used to solve the discretized equations for MQS and EMQS analysis. Furthermore, a fast algorithm with close to $O(N)$ performance in both CPU time and memory is developed by accelerating the $O(N^2)$ part of the matrix-vector multiplication of the iterative solver with the Precorrected-FFT algorithm.

10.2 Future work

1. 1-D simplification of MQS analysis for thin conductors

   A 1-D simplification of the formulation can be used for time and memory efficiency when a conductor is thin. The basic idea is to assume that the current is nonzero only along the length of the conductor. For the currents related with a surface, the current in the normal direction is zero because of MQS assumption, while the current in the tangential direction orthogonal to the length of the conductor should be negligible compared to the current in the tangential direction along the length. In [39], the 1-D simplification is already developed and tested. The number of unknowns of the simplified linear system is less than half of that of the original system. If GMRES and the Precorrected-FFT algorithm are used to accelerate the solution, a faster algorithm can be developed.

2. High frequency simplification

   At frequencies high enough, a substantial simplification can be made because the P_1 and D_1 matrices can be taken as diagonal. Then $\frac{\partial \bar{E}}{\partial n}$ can be eliminated from the linear system. At the same time, the current in the normal direction can be represented with charge density on the surface. This gives a linear system with the number of unknowns about half of that of the original linear system. Again, If GMRES and Precorrected-FFT algorithm are used to accelerate the solution, a faster high frequency algorithm can be developed to compute the high frequency resistance, effective inductance and resonance peaks.

   For thin conductors, the tangential current orthogonal to the length of the conductor can be neglected as in the 1-D simplification, and this gives a system with the tangential current along the conductor, the charge and the scalar potential as the only unknowns. If the preconditioned GMRES method and the Precorrected-FFT algorithm is applied to solve the linear system, better performance can be achieved.

Bibliography

[1] R. F. Harrington. *Field Computation by Moment Methods.*. MacMillan, New York, 1968.

[2] J. D. Jackson. *Classical Electrodynamics.* John Wiley & Sons, New York, second edition, 1975.

[3] H. A. Haus and J. R. Melcher. *Electromagnetic Fields and Energy.* Prentice-Hall, Englewood Cliffs, NJ, 1989.

[4] Chen-to Tai. *Dyadic Green functions in electromagnetic theory.* IEEE Press, Piscataway, NJ, 1994.

[5] J.N. Newman. Distributions of sources and normal dipoles over a quadrilateral panel. *Journals of Engineering Mathematics*, pages 113–126, 1986.

[6] J.L. Hess and A.M.O. Smith. Calculation of potential flow about arbitrary bodies. *Progress in Aerospace Sciences*, Vol.8, pp. 1-138, 1966.

[7] L. Greengard. *The Rapid Evaluation of Potential Fields in Particle Systems.* Cambridge, Massachusetts: M.I.T. Press, 1988.

[8] J. R. Phillips and J. K. White. A Precorrected-FFT method for Electrostatic Analysis of Complicated 3-D Structures. *IEEE Trans. on Computer-Aided Design*, Vol. 16, No. 10, pp.1059-1072, October 1997.

[9] Wenjing Ye. A fast 3D solver for unsteady Stokes flow with applications to microelectromechanical systems. In *Proceedings of the Second International Conference on Modeling and Simulation of Microsystems*, San Juan, 1999.

[10] S. Kapur and J. Zhao. A fast method of moments solver for efficient parameter extraction of MCMs. *Design Automation Conference*, 1997, pp. 141–146.

[11] Johannes Tausch and Jacob White. Wavelet-like Bases for Integral Equations on Surfaces with Complex Geometry. *IMACS Series in Computational and Applied Mathematics*, IMACS, 1998.

[12] Johannes Tausch and Jacob White. A Multiscale Method for Fast Capacitance Extraction. *36th Design Automation Conference*, pp.537–542, New Orleans, 1999.

[13] Y. Saad and M. H. Schultz. GMRES: A generalized minimal residual algorithm for solving nonsymmetric linear systems. *SIAM Journal on Scientific and Statistical Computing*, 7:856–869, July 1986.

[14] W. Hackbusch. *Iterative Solution of Large Sparse Systems of Equations* Springer-Verlag, New York, 1994.

[15] J. Tausch and J. White. Second-Kind Integral Formulations of the Capacitance Problem. *Advances in Computational Mathematics*, pp. 141–146, 1997.

[16] Keith Nabors and Jacob White. Fastcap: A multipole accelerated 3-d capacitance extraction program. *IEEE Transactions on Computer-Aided Design*, 10(11):1447–1459, November 1991. This is a full ARTICLE entry.

[17] J. Phillips and J. White. A precorrected-FFT method for capacitance extraction of complicated 3-D structures. In *Proceedings of the Int. Conf. on Computer-Aided Design*, November 1994.

[18] M. Kamon, M.J. Tsuk and J.K. White. FASTHENRY: A multipole accelerated 3-D Inductance Extraction Program. *IEEE Trans. MTT*, vol.42, No.9, pp. 1750–pp1758, Sep. 1994.

[19] M. Kamon, F. Wang and J. White. Recent Improvements to Fast Inductance Extraction and Simulation. In *Proceedings of the* 7^{th} *Topical Meeting on Electrical Performance of Electronic Packaging*, West Point, New York, October, 1998, pp. 281-284.

[20] A. Farrar and A. T. Adams. Matrix methods for microstrip three-dimensional problems. *IEEE Transactions on Microwave Theory and Techniques*, MTT-20(8):497–504, August 1972.

[21] A. E. Ruehli and P. A. Brennan. Efficient capacitance calculations for three-dimensional multiconductor systems. *IEEE Transactions on Microwave Theory and Techniques*, 21(2):76–82, February 1973.

[22] A. E. Ruehli. Inductance calculations in a complex integrated circuit environment. *IBM J. Res. Develop.*, 16:470–481, September 1972.

[23] P. A. Brennan, N. Raver, and A. Ruehli. Three dimensional inductance computations with partial element equivalent circuits. *IBM Journal of Res. and Develop.*, 23(6):661–668, November 1979.

[24] D. Ling and A. E. Ruehli. Interconnect modeling. In A. E. Ruehli, editor, *Circuit Analysis, Simulation and Design, 2*, chapter 11, pages 211–332. Elsevier Science Publishers B. V., North-Holland, 1987.

[25] W. T. Weeks, L. L. Wu, M. F. McAllister, and A. Singh. Resistive and inductive skin effect in rectangular conductors. *IBM Journal of Res. and Develop.*, 23(6):652–660, November 1979.

[26] A. C. Cangellaris, J. L. Prince, and L. P. Vakanas. Frequency-dependent inductance and resistance calculation for three-dimensional structures in high-speed interconnect systems. *IEEE Transactions on Components, Hybrids, and Manufacturing Technology*, 13(1):154–159, March 1990.

[27] Yehia Massoud and Jacob White. Simulation and Modeling of the Effect of Substrate Conductivity on Coupling Inductance. In *Proceedings of the International Electron Devices Meeting*, Washington D.C., pp. 491-494, December 1995.

[28] A.R. Djordjevic, T.K. Sarkar, and S.M. Rao. Analysis of finite conductivity cylindrical conductors excited by axially-independent TM electromagnetic field. *IEEE Trans. Microwave Theory Tech.*, vol.MTT-33, pp.960-966, Oct.1985.

[29] E. Tuncer, Beom-Taek Lee, and D. P. Neikirk. Interconnect Series Impedance Determination Using a Surface Ribbon Method. In *IEEE 3rd Topical Meeting on Electrical Performance of Electronic Packaging*, Monterey, CA, Nov. 2-4, 1994, pp. 250-252.

[30] R.B. Wu and J.C. Yang. Boundary integral equation formulation of skin effect problem in multiconductor transmission lines. *IEEE Trans. Magnetics*, vol. Mag-25, pp.3013-3015, July 1989.

[31] M.J. Tsuk and J.A.Kong. A Hybrid Method for the calculation of the resistance and inductance of transmission lines with arbitrary cross sections. *Microelectronic System Interconnections*, pp65-pp74, IEEE Press, Piscataway, NJ, 1993.

[32] M. Kamon, N. Marques, and J. White. FastPep: A Fast Parasitic Extraction Program for Complex Three-Dimensional Geometries. In *IEEE/ACM International Conference on Computer Aided-Design*, San Jose, California, November 1997.

[33] Grover and Frederick Warren. *Inductance calculations, working formulas and tables*, New York, 1946.

[34] Ali M. Niknejad. *Analysis Design and Optimization of Spiral Inductors and Transformers for Si RF ICs*, Ph.D Thesis, UC Berkeley.

[35] W. E. Arnoldi. The principle of minimized iteration in the solution of the matrix eigenvalue problem. *Quart. Appl. Math.*, 9:17–29, 1951.

[36] George A. Baker Jr. *Essentials of Padé Approximants.* Academic Press, New York, NY, First edition, 1975.

[37] Matton Kamon. *Fast Parasitic Extraction and Simulation of Three Dimensional Intercnnect via Quasistatic Analysis*, Ph.D Thesis, MIT, February 1998.

[38] Joel Phillips. *Rapid solution of potential integral equations in complicated 3-dimensional geometries*, Ph.D Thesis, MIT, June 1997.

[39] Junfeng Wang, Johannes Tausch and Jacob White. A wide frequency range surface formulation for 3-D inductance and resistance extraction. In *Proceedings of the Second International Conference on Modeling and Simulation of Microsystems*, San Juan, March 1999.

[40] Junfeng Wang, Johannes Tausch and Jacob White. A wide frequency range surface formulation for distributed RLC extraction. *International Conference on Computer Aided Design*, San Hose, November 1999.

[41] Junfeng Wang , Johannes Tausch and Jacob White. Improved Integral Formulations for Fast 3-D Method-of Moments Solvers. In *Proceedings of EPEP 98*, p.273-276, West Point, NY, Oct. 1998.

[42] Junfeng Wang and Jacob White. Fast Algorithms for Computing Electrostatic Geometric Sensitivities. In *Proceedings of SISPAD 97*, Boston, MA, Sep., 1997.

[43] Yehia Massoud, Junfeng Wang and Jacob White. Accurate Inductance Extraction with Permeable Materials Using Qualocation. In *Proceedings of the 2-nd International Conference of Modeling and Simulation of Microstructures*, Peurto Rico, Apr., 1999.